.

Detection and Analysis of Low Energy Electrons in a Scanning Electron Microscope using a novel detector design based on the Bessel Box Energy Analyser

Ashish Suri

PhD

University of York

Electronic Engineering

2019

.

f

.

Abstract

Advancements in the field of scanning electron microscopy have been one of the major nano technology enablers. A scanning electron microscope (SEM) generates a magnified image of the sample by bombarding it with an electron beam and detecting the electrons that scatter off the surface along with the electrons that are generated in the sample. In conventional SEMs, the generated or secondary electrons are detected by the famous Everhart Thornley detector via positively biased input-grid. However, in doing so, it loses energy and angular information of the electrons. This information is crucial to interpret the SEM image of the sample under study.

What is needed is a small and compact detector that can detect electrons and furnish energy information inside an SEM chamber. The detector designed to achieve these aims is able to detect low energy electrons at the same time able to take the geometrical constraints of the SEM into account. This study presents a design and implementation of a novel secondary electron detector based on the Bessel Box (BB) energy analyser for SEM

Simulations were carried out for the design in SIMION 8.1 ray tracing software. An energy resolution of 0.4% has been numerically calculated and experimentally tested in an ultra-high-vacuum chamber. This was followed by the integration of the BB detector to a conventional scanning electron microscope.

The device described would be appealing to the electron microscopy and spectroscopy at large. The detector has been successfully demonstrated for electron spectroscopy applications: Auger and secondary electron. It has also been demonstrated for secondary electron microscopy, all obtained by as-designed BB detector.

.

Table of Contents

.

.

.

List of figures

.

.

.

.

.

List of Abbreviations

SEM	scanning electron microscope
SAM	scanning Auger microscope
SE	secondary electron
UHV	ultra-high vacuum
AES	Auger electron spectroscopy
EDX	energy dispersive X-ray spectroscopy
EFSEM	energy filtered secondary electron microscopy
ET	Everhart Thornley (detector)
TTL	through the lens (detector)
FEG-SEM	field emission gun scanning electron microscope
IMFP	inelastic mean free path
BSE	back scattered electron
WDS	wavelength dispersive X-ray spectroscopy
LEE	low energy electrons

.

SEY	secondary electron yield
BSC	back scattered coefficient
TEY	total electron yield
REELS	reflected electron energy loss spectroscopy
TEM	transmission electron microscope
FEG	field emission gun
LED	lower electron detector
UED	upper electron detector
LEED	low energy electron diffraction
CEM	channeltron electron multiplier
PEEK	polyether ether ketone
TFE	thermally assisted field emission
EBT	electron beam testers
SIMS	secondary ion mass spectroscopy
QMS	quadrupole mass spectrometer

.

EHV	extreme high vacuum
ESD	electron stimulated absorption
RBB	retarding Bessel box
ID	internal dimension
OD	outer dimension
SFEM	scanning field emission microscope

.

Acknowledgments

'For my part I know nothing with any certainty, but the sight of the stars makes me dream' (Vincent Van Gogh).

The last years spent at the University of York have enriched my experience as a researcher in the field of Electron Microscopy. I take this opportunity to thank my supervisors Prof. Mohamed El-Gomati and Dr. Steve Tear. Under their kind supervision and continued support, I was able to successfully pursue my scientific goals. Their expertise and valuable feedback along this journey, helped me to think critically and contribute positively to the experiments and thesis writing. I am thankful for their belief in me and for providing me with this opportunity in the SIMDALEE2 consortium.

Furthermore, I would like to extend my gratitude to Dr. Christopher Walker and Dr. Andrew Pratt for their assistance and support in terms of valuable feedback and scientific discussions during our periodic brainstorming sessions. I am thankful to the support extended by Prof. Danilo Pescia, with a successful collaboration with his group at ETH Zurich. I am grateful to be part of the SIMDALEE 2 consortium, all the mentors and students for fruitful discussions during our meetings.

The design and testing of the detector has been possible only with active support of the Mechanical workshop at the Department of Physics, University of York particularly Mr. Jason Flatt. I am thankful to him for the assistance.

In the end, I would like to extend my gratitude to my mother, brother and my partner for their understanding and support during this time. Finally, I would like to dedicate this thesis to my late father. His belief in me has made this journey possible.

.

Author's Declaration

I declare that this thesis is a presentation of original work and I am the sole author. This work has not previously been presented for an award at this, or any other, University. All sources are acknowledged as References.

List of publications (peer reviewed):

1. ***Analysis and detection of low energy electrons in electron microscopes using a Bessel box energy analyser, Ashish Suri, Andrew Pratt, Steve Tear, Christopher Walker, Cem Kincal, Umut Kamber, Oguzhan Gurlu, Mohamed El-Gomati, Journal of electron spectroscopy and related phenomena (2019).***
2. ***"Next generation secondary electron detector with energy analysis capability for SEM", Ashish Suri, Andrew Pratt, Steve Tear, Chris Walker, Mohamed El-Gomati, Journal of Microscopy (in press).***

List of publications (Conference Paper):

1. ***"Characterization of a Miniature Electron Energy Analyzer for Scanning Electron Microscopes", Ashish Suri, Andrew Pratt, Chris Walker, Steve Tear, Mohamed El-Gomati, Journal of Physics: Conf. Series, 902, 012017 (2017).***

.

Chapter 1: Introduction

Recent developments in nano, material and biological sciences are driven by advancements in probing and characterising technologies. These characterisation tools provide a peek into the micro and nano realms decoding physical mechanisms at play to control and manipulate matter. Understanding the physics for fundamental elements or next generation functional materials has placed the onus on parallel improvements in characterisation techniques. One of the most popular instruments that uses an electron source to image and characterise the sample is the scanning electron microscope (SEM) (1). SEM has been a popular choice for many decades now because it generates 3D (three dimensional) like images for micro to nano sized objects. Furthermore, the SEM offers a non-destructive method for the identification of the elements from the sample under study.

It generates a magnified image of the sample by employing a beam of electrons. The interaction of an electron beam with a solid surface leads to the generation of electrons and photons in the sample, some of them form important signals for microscopy and spectroscopy. Electrons generated in the sample are termed as secondary electrons (SE). The energy information of the detected SEs provides crucial information pertaining to the sample's chemical and electronic structure. While most of the SEs are low energy electrons (< 50 eV) some of them may also be detected at high energy as a signature signal for the element under study. These SEs are called Auger electrons. Elemental identification is also carried by detecting characteristic X-rays.

Auger electron spectroscopy (AES) is a widely established technique for elemental identification on solid surfaces (2) carried out in scanning Auger microscopes (SAM). However, it is normally carried out in an ultra-high vacuum (UHV) environment to maintain a clean sample surface for the duration of the experiment (3). Conventionally, X-ray spectroscopy (EDX) is performed for elemental identification in an SEM but not AES. However, EDX has inferior spatial resolution and depth of information (~ 1 μm) when compared to AES where it is better than 10 nm (1). Auger electron and characteristic X-ray emissions are competing physical phenomena occurring as a

.

result of electron-solid interaction. While AES is more sensitive towards samples containing low atomic number elements such as biological and polymer materials, EDX on the other hand is more sensitive towards heavy elements such as gold and silver. Therefore, introducing AES as a complementary technique to EDX can enhance the performance of SEM for element identification at nano-scale. This is the first of the two cases advocated by this work. The second application stems from the recent developments in energy-filtered SE microscopy (EFSEM) which has laid emphasis on the low energy SE spectra. Studies have shown that by tuning the detector at the desired pass-energy, relative contrast in the SEM image can be enhanced between the elements in the sample (4). Conventional SE detectors such as the Everhart-Thornley detector (ETD) or through-the-lens (TTL) detectors, both offer little to no energy analysis (e.g. ETD (5)) or limited energy filtering capability (e.g. the low-pass energy filter in TTL (6)).

This thesis attempts to enhance the capability of an SEM by detecting and energy analysing electrons. A novel low energy detector design is proposed which is based on the Bessel Box energy analyser. The emphasis is laid on electron energy analysis in an SEM environment for spectroscopy (SE and AES) and microscopy (SE) applications. The prerequisites for such a detector design pertain to: (a) Numerical calculations for the detection of low energy electrons for microscopy and SE spectroscopy. (b) Energy resolution comparable to the state-of-the-art energy analysers such as cylindrical mirror analyser (CMA) for Auger spectroscopy. (c) Finally a compact design to take the geometrical restrictions imposed by the SEM components near the sample, into account. This also helps in the portability of the device over SEM variants.

The thesis begins by underlining the fundamentals of electron-solid interaction in Chapter 2. This is followed by chapter 3 which discusses the SEM instrument with a review of the state-of-the-art SE detectors and Auger energy analysers. Subsequently, the chapter 4 introduces the BB energy analyser and discusses the numerical simulations for the BB design. The numerical work was instrumental in streamlining the design considerations for the BB analyser. The experimental characterisation of the as-designed BB in a ultra-high vacuum system is discussed in chapter 4. This is

.

followed by the discussion of spectroscopic and microscopic BB-results acquired in the JEOL field emission SEM (FEG-SEM) in chapter 5. The thesis is concluded with a summary and discussion on future development of this novel detector in chapter 6.

.

Chapter 2: Electron-Solid Interaction

It was five years after the discovery of the electron by J. J. Thompson in 1897 (7) that the phenomena of SE emission was discovered by Austin and Starke in 1902 (8). This was achieved while studying electron reflection from a variety of metal targets (such as copper aluminium, iron, platinum etc.). Based on the intensity of the reflected beam, their work concluded that besides the ordinary reflection process, another set of electrons are also released from the metal target. These additional set of electrons were termed the secondary electrons (SEs).

SEs are electrons generated in a solid upon bombardment of a photon or a charged particle, of sufficient energy. The term ‘secondary’ is used to indicate the generation of electrons in an element as a consequence of the interaction with a ‘primary’ source. When an electron source is involved, as in microscopy in an SEM or spectroscopy in an SAM, the electron-source is referred to as ‘primary-electron beam’ and the electrons as ‘primary electrons’. The study of SEs is important because they provide topographical and chemical information of the element under study.

This chapter is divided into 6 sections. The first section provides a qualitative picture of electron-solid interaction and detectable entities emanating from it. This is followed by section 2 which underlines the fundamentals of SE emission: generation, transport and escape. This is followed by a discussion on yield, energy and angular distribution of the emanated electrons in sections 3, 4 and 5 respectively. These properties are useful for detection and analysis in electron microscopes. Finally, the chapter concludes with a brief discussion on Auger emission.

2.1. Electron Beam-Solid Interaction

The bombardment of an electron beam on a solid causes the primary-beam electron to undergo a cascade of scattering processes. The scattering events can be classified as

.

elastic or inelastic. In an elastic collision, the energy of the primary-beam electron remains unchanged while its direction of propagation can change. In an inelastic collision, the primary-beam electron can lose a fraction or all its energy to the sample, generating various entities within the sample. A scattering event is characterized by the scattering cross-section (elastic or inelastic) and by mean free path or MFP (elastic or inelastic). A scattering cross-section is a concept of the probability of the occurrence of an event and the MFP gives an average distance travelled by the electron between successive scattering events A general expression for scattering cross section is defined as:

$$\sigma = \frac{N_e}{n_i n_t}$$

2. 1

where N_e is the number of scattering events per unit volume, n_i is the number of incident particles per unit area and n_t is the number of target sites per unit volume. In general, smaller the cross section, longer the MFP and lesser probability of the occurrence of the scattering event.

2.1.1. Elastic Interaction

The penetrating primary-beam electron can interact elastically under the influence of attractive columbic forces with the positively charged sample atom or experience repulsive coulombic forces from the sample electrons. This interaction alters the electron trajectories within the sample. The net deflection can be anywhere between 0^o to 180^o with no change in its energy. After numerous such elastic scattering events, a fraction of the primary-beam electrons can escape into the vacuum (1). The Rutherford-type model has been often used for calculating elastic cross-section, which assumes electrons as classical particles scattered by the sample nuclei. The elastic cross section is given by (9):

$$\sigma_{el} = 5.21\text{x}10^{-21}\left(\frac{Z}{E}\right)^2 \frac{4\pi}{\alpha(1+\alpha)}\left(\frac{E+511}{E+1024}\right)^2$$

2. 2

.

where Z and E are the atomic number and kinetic energy of an incident electron respectively. The parameter α takes into account the screening effect of the outer shell electrons. This is needed because the primary-beam electron does not see all the charge on the nucleus which is screened by the electron cloud around it.

The elastic cross-section increases with the atomic number (Z) of the element under study which means the probability of elastic scattering from a heavy element like gold is higher than from a carbon atom with lower atomic number. While this formula has been widely used for its simplicity, it has been demonstrated to be a poor approximation for heavy elements and low electron energies, where wave-nature of the electrons becomes important to characterise the interaction. The Mott cross-section is used instead. It takes the wave properties into account and is elaborated elsewhere (10).

2.1.2. Inelastic Interaction

A single inelastic interaction results in loss of a fraction of primary-electron energy and results in a small change in its trajectory angle. A cascade of such inelastic scattering events causes either the primary-beam electron to lose a part of its energy and escape the sample or loose all its energy to the sample. The inelastic interaction, much similar to the elastic interaction, is characterized by an inelastic cross section (σ_{in}) and an inelastic mean free path (IMFP). The net IMFP is the contribution from all the possible inelastic interactions in the sample, and is given by:

$$\frac{1}{\lambda_{IMFP}} = \frac{1}{\lambda_{plasmon}} + \frac{1}{\lambda_{core}} + \frac{1}{\lambda_{outer\ shell}} + \frac{1}{\lambda_{phonon}} + \frac{1}{\lambda_{valence}} \qquad 2.3$$

where $\lambda_{plasmon}$, λ_{core}, $\lambda_{outer\ shell}$, λ_{phonon}, $\lambda_{valence}$ are individual IMFPs due to plasmon excitation, core transition, outer-shell transition, phonon excitation and valence band transition respectively. These inelastic interactions include:

a) Phonon excitation: quantum of lattice vibration corresponding to losses of 0.02 - 1 eV.

.

b) Plasmon excitation: quantum of collective electron vibration corresponding to losses of 5- 60 eV.

c) Excitation of a core electron (K, L, M, N..) to an unoccupied state above the Fermi level.

d) Ejection of outer shell electron.

e) Interaction with single valence band electron.

The transfer of energy due to inelastic interaction results in the generation of different types of entities within the sample, some of which form important detectable signals for extracting the topographical and chemical information in an instrument like SEM, is summarised in Figure 1.

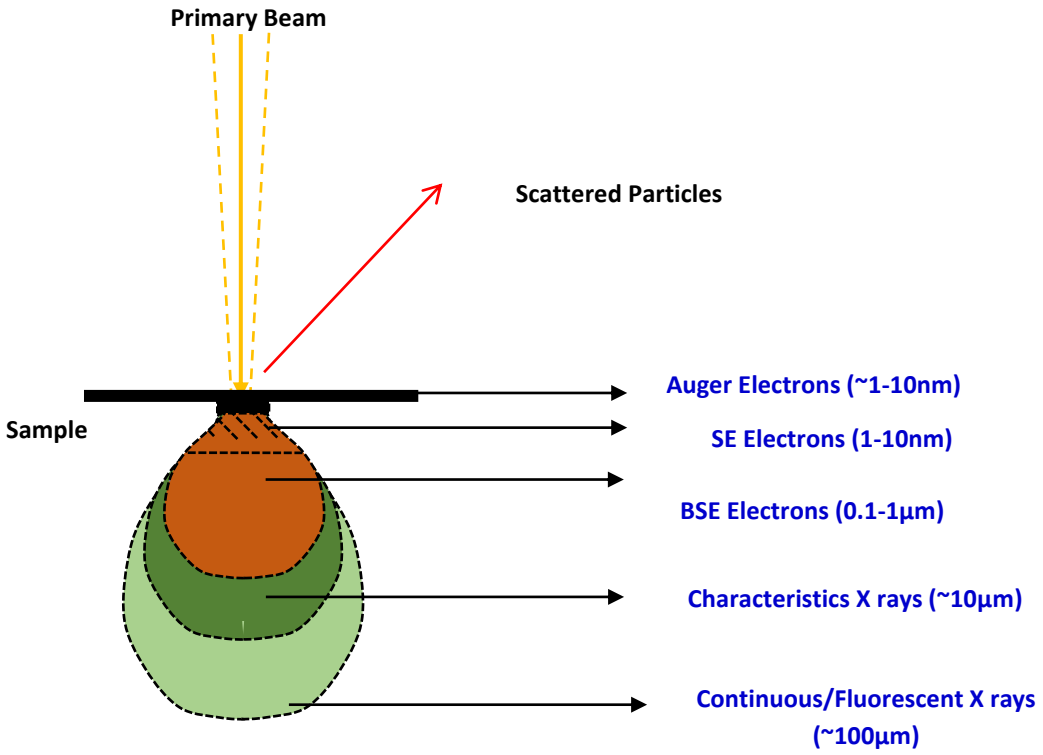

Figure 1 Summary of the signals generated due to electron-solid interaction and respective information depth.

- Secondary Electrons: These are mainly low energy electrons (LEE) generated in the sample. The SEs originate as loosely bound electrons in the valence or conduction band of the sample atoms. During inelastic beam interaction, a part of the energy may be gained by these electrons and be able to escape into the

.

vacuum. A cascade of such events leads to the SE signal that is used for imaging.

- Back Scattered Electrons (BSE): Primary beam electrons that are back scattered from the sample elastically or have undergone losses are collectively termed as BSE. The SE and BSE form the most important imaging signal in an SEM.
- Auger Electrons and X-ray emission: The inelastic interaction can eject some of the tightly bound inner shell electrons. The primary beam electron loses energy equal to the binding energy of the electron corresponding to the ejected electron's occupied shell. Simultaneously, the atom is excited to a higher energy with a missing electron in its inner shell (atomic orbital). Subsequently, the atom releases its excess energy by the transfer of an electron from a higher energy shell to its inner shell releasing X-rays or another electron called Auger electron from another outer shell. Since the energy difference between the shells is the characteristic of the element under study, energy analysis of these X-rays or Auger electrons have proven to be a very powerful tool in furnishing the chemical information of the sample. X-ray and Auger electron emissions are competitive processes. The X-ray emission is dominant for heavier atoms while the Auger process is dominant for lighter atoms. The corresponding spectroscopies are termed as AES and EDX respectively.
- Braking Radiation: An electron passing by an atom might be deaccelerated. This deceleration leads to the generation of the braking X-rays and are termed by the German word 'Bremsstrahlung X-rays'. These X-rays form the background continuous signal in the X-ray spectrum.
- Cathodoluminescence: In addition to the X-ray emission, recombination of excess electron hole pairs in semiconductors can result in the emission of visible photons which can be used for imaging.
- Sample current: Some of the electrons are absorbed by the sample and can be measured as sample to ground current.

A typical curve for the energy dependence of IMFP is shown in Figure 2 (11). An empirical relation is described by Seah and Dench by fitting a curve on the

.

experimental dataset on the IMFP values. As can be seen in the figure, a minimum IMFP lies at the electron energy corresponding to highest inelastic scattering for example a minimum of about 100 eV in the IMFP corresponds to strong plasmon excitation in Silver. At higher energies, ionization of the core electrons is most favoured which is the least probable of excitation leading to an increase in the IMFP. Below the minimum, the low energy electrons (hot electrons) can interact only with conduction electrons, the probability of which depend on the number of electrons it can excite (accessible filled states) and the number empty states available for it go to. Sze described such energy dependence as E^{-2}, this was also used by Seah and Dench for the IMFP description for low energies (11). Elastic scattering is more likely to be favoured in this regime.

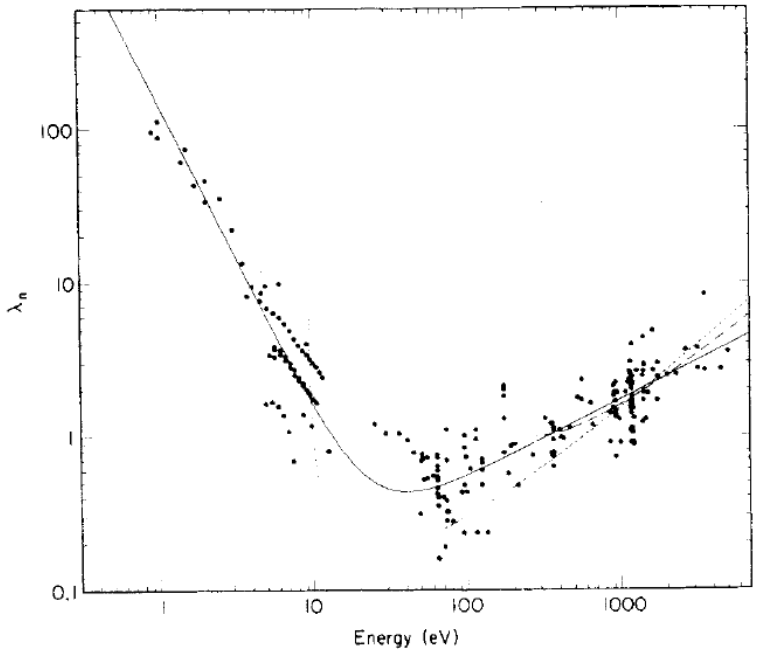

Figure 2 Typical profile of inelastic mean free path. This data is taken from the work of Seah and Dench **(11)**. A curve is fitted on the experimental dataset for IMFP values.

2.1.3. Stopping Power and Energy Dissipation Rate

As previously mentioned, the primary-electron looses energy while interacting with the solid. An expression was given for the same by Hans Bethe in 1930s (12). In this model, the contribution of all the possible events that can cause energy loss is represented by a factor called the mean ionization energy. According to Bethe's

.

theory, (also called the continuous slowing down approximation) the average rate of energy transfer (*dE/ds)* to the sample is given as:

$$\frac{dE}{ds} = -2\pi e^4 N_a \left(\frac{Z\rho}{A_w E}\right) ln\left(\frac{1.166E}{J}\right)$$

2. 4

where e is the electron charge, N_a is Avogadro's number, Z is the atomic number, ρ is the atomic density, A_w is the atomic weight and E is the electron energy in the sample and J is the mean ionisation energy and s is the distance travelled in the solid. The negative sign indicates the loss of primary beam energy. Berger and Seltzer calculated its value empirically and demonstrated that J (keV) nearly-linearly depend on the atomic number, given by (1):

$$J = (9.76Z + 58.5Z^{-0.19}) \text{ x } 10^{-3}$$

2. 5

Stopping power results from the combined average contribution from all the discrete inelastic processes. Although, it is a good approximation for electron energies greater than the mean ionisation energy J, it is not valid for energies lower than the J as dE/ds would be positive. Instead individual inelastic cross sections are studied, or the inelastic interaction is modelled using optical dielectric functions. This is beyond the scope of this thesis and for the review of quantitative/qualitative description of various interaction models, the reader may refer to the reference (10).

2.1.4. Information Depth

The electron-solid interaction occurs within a finite volume in the solid and is termed as 'interaction volume'. This has been simulated using various models (10) and is also visualised experimentally by bombarding an electron beam on some insulators such as polymethyl methacrylate (PMMA). The PMMA undergoes chemical changes and is rendered prone to etching when treated with suitable solvents. This is the principle of e-beam lithography. The volumetric extent of etching would then be equal to the interaction volume. The entities generated due to inelastic scattering originate throughout the interaction volume. However, the detectable signals in the vacuum

.

previously described (Figure 1), depend on the individual escape depths. Longer escape depth as in X-rays, in comparison with SE, also result in the lateral expansion of the escape width. Therefore, the SE images have the highest spatial resolution of all the signals generated in SEM and is discussed in subsequent sections.

The interaction volume strongly depends on the energy of the primary beam. The average range travelled by the primary-beam energy E_P is correlated with the stopping power of equation 2. 4 and is given by simply integrating it over energies from 0 to E_P:

$$R = \frac{1}{\rho}\int_0^{E_P} \frac{-1}{\left(\frac{dE}{ds}\right)} dE \qquad 2.\ 6$$

The higher the beam energy, the larger the expected interaction volume. Qualitatively it can be understood as follows: upon increasing the beam energy the inelastic cross-sections decrease, leading to a decrease in the stopping power (rate of energy loss per distance travelled) of the primary electron. Thus, the primary electron can penetrate much deeper into the sample (the penetration depth given by equation 2.6), because of both its higher initial energy and the reduced stopping power at high energies, before losing all of its energy to the sample. Furthermore, the loss factor from the Bethe expression increases with increasing atomic number. The combination of these two factors results in heavier elements (such as gold) with shallower interactional depth as compared to lighter elements (such as carbon). Figure 3 shows a schematic of the interaction volume within the sample for higher and lower primary-beam energies. Primary beams with energies less than 1 keV down to a few hundreds of eV are generally considered to be LEE beams. Probing samples with LEE confine the interaction of the primary-beam very near to the sample surface, close to the point of impact, yielding surface-sensitive information.

.

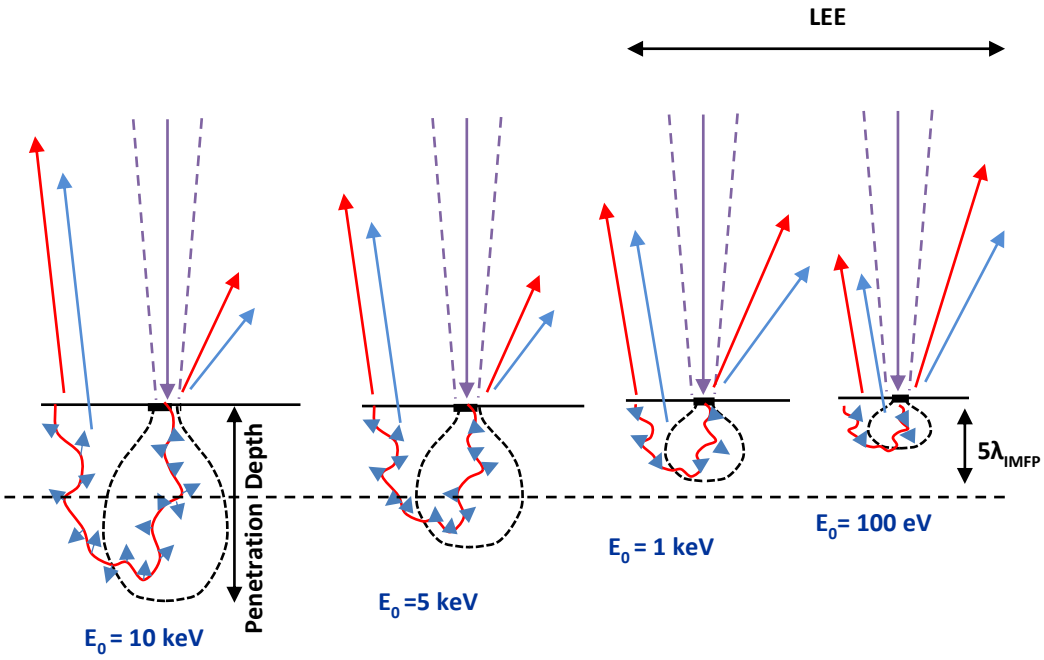

Figure 3 Pictorial representation of the effect on the interaction volume with decreasing primary-beam energy, E_0.

2.2. SE Emission

The phenomenon of SE emission is usually described as a 3-step procedure: SE generation on beam impact (SEI), slowing down and transport of primary beam through the sample generating more SEs in a cascade process (SEII) and finally the escape of SEs into the vacuum.

In an SEM, the SEs are detected for generating a magnified image of the sample under study. The detection of SEs in an SEM is important because they not only contain sample information but demonstrate the highest spatial resolution for imaging. There are primarily two kinds of SEs emanating from the sample labelled as SE-I and SE-II in Figure 4. The SE-Is are generated by the direct impact of the primary-electron beam on the sample, very close to the electron-beam point of impact, whilst SE-IIs are generated by the BSEs. Both SE-I and SE-II are conveniently termed as 'true SEs' because their origins lie in the sample. In practice, further to the SE-I and SE-II types, another type of SEs are identified as SE-IIIs, which are generated when high-energy

.

BSEs that emerge from the sample strike the objective pole piece or the chamber walls and generate SEs from these surfaces, as shown in Figure 4. These electrons introduce a background signal, which adds an unrelated signal to that originating from the sample and are therefore difficult to interpret and need to be avoided.

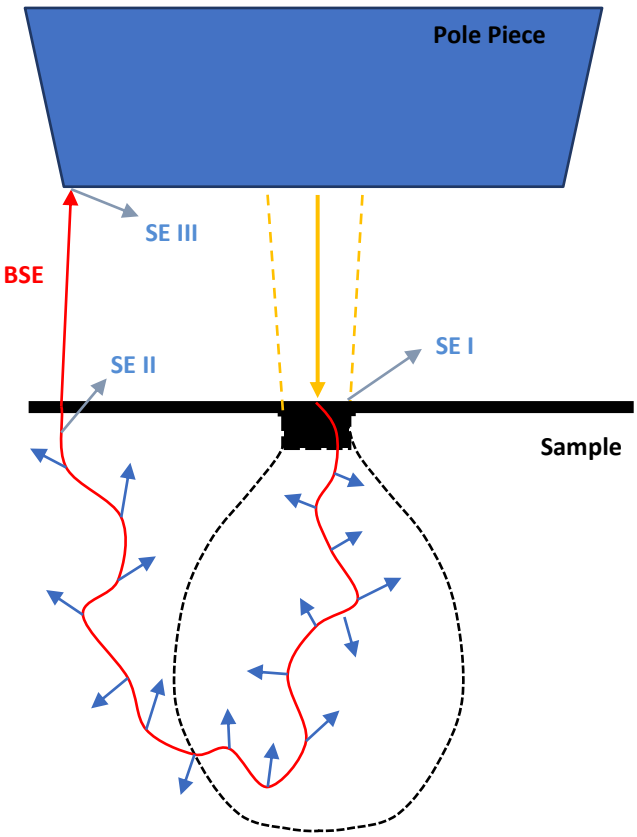

Figure 4 Types of secondary electrons, for example, in SEM: SE I, SE II and SE III.

2.2.1. SE Generation

A widely accepted picture for the SE generation in a solid is of a single electron excitation of inner (K and L) and outer (valence and d-shell) shell electrons (1). In metals, one electron transitions due to plasmon-decay also contribute to the total number of SEs. Plasmons are quanta of the collective oscillations of free electrons in a metal. The simulations carried out by Chung and Everhart show that in Aluminium (13), most of the contribution to the SEs come from the plasmon decay, while in Cu, Au and Ag, the contribution from the excitation of d-shell electron is also significant.

.

2.2.2. SE Transport

A single SE generated due to inelastic interaction of a single primary electron can potentially generate more SEs as they encounter another scattering site by the same mechanisms as discussed in the previous section. Some of the primary-beam electrons travel deeper into the sample and loose their energy due to a cascade of inelastic collisions before coming to a halt or escaping into the vacuum. These inelastic processes also generate SEs and Auger electrons which can have energies of up to 2 keV or more depending on the sample atomic number and the incident electron energy. This multiplication of electrons due to cascade process was first proposed by Wolff in 1954 (14). This is the reason as to why one may obtain a greater number of electrons than the incident electrons.

When the energy of a BSE or an SE is reduced to a minimum level due to losses, they experience primarily elastic scattering (Figure 2) and tend to diffuse through the sample. Now, only those SEs and Auger electrons which are within a few mean free paths (5-15 nm) of the surface can escape and be detected. Since the BSEs which have generated the SE-IIs have also travelled some distance in the sample, these SEs emerge from the surface of the sample at distances much further laterally from the primary-beam impact point.

2.2.3. SE Escape

After generation and transportation SEs still have to overcome the in-built potential or the work function to be able to escape the sample. The difference in the potentials in the sample and the vacuum leads to the electronic refraction of the SEs (15). Thus, the angles at which the electrons are emitted can now be interpreted from Snell's law for electrons (15) as follows:

$$\sqrt{E_s}\sin(\beta) = \sqrt{E_k}\sin(\alpha) \qquad 2.7$$

An electron generated with energy E_s in the sample (referring to the bottom of the conduction band), approaches the sample-vacuum interface at an angle β (Figure 5a). The electron emits with energy E_k, (referred to the local vacuum) at an angle α,where

.

the relationship between E_k and E_s depends on the work function of the metals (ϕ) and Fermi level energy E_f (Figure 5b) and electron affinity (χ) for semiconductors (Figure 5c):

$$E_s = E_k + E_f + \phi$$

2. 8

$$E_s = E_k + \chi$$

2. 9

Furthermore, α = 90° which is the case for total internal reflection corresponding to ß > ß$_1$ where electrons are reflected into the sample, is given by:

$$\sin(\beta_1) = \sqrt{\frac{E_k}{E_s}}$$

2. 10

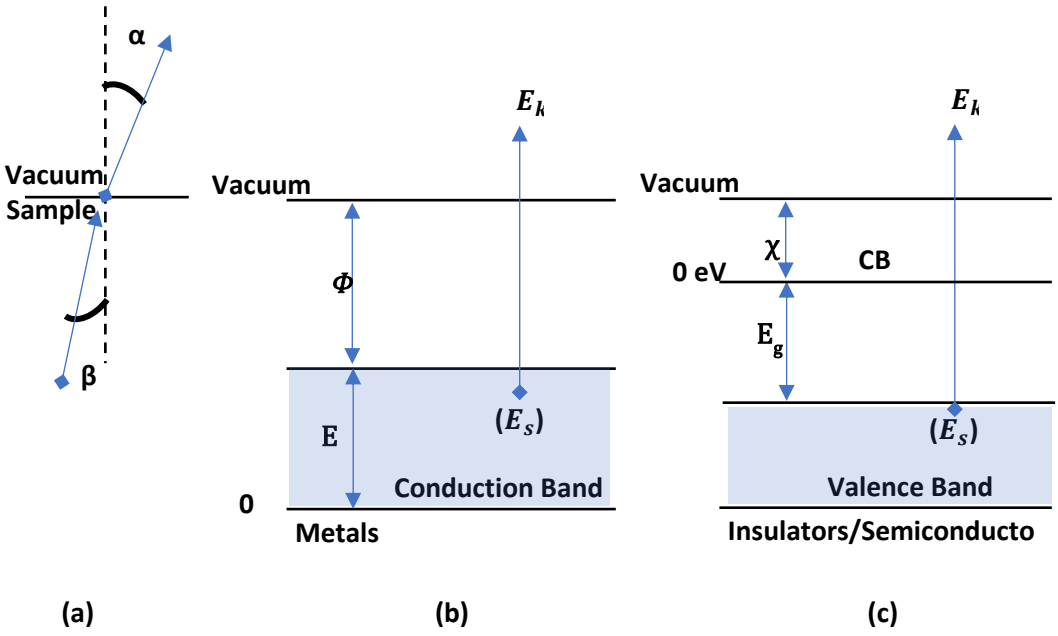

Figure 5 (a) Refraction of the generated electrons because of the difference in the potentials between sample and vacuum. Band diagram of a metal (b) and an insulator/semiconductor (c) vacuum energy levels.

.

2.3. SE Yield and Back Scattering Coefficient

Once the SEs and BSEs escape the sample, they can be detected as free electrons in the vacuum. The electron-solid interaction characterisation is carried out by estimating the SE yield (SEY) and back scattering coefficient (BSC). These macroscopic properties primarily depend on the element under study and the primary beam energy. SEY is the ratio of the total SEs emanated from the sample to the total incident electrons, denoted by δ. Similarly, BSC is the ratio of the total BSEs detected to the total incident electrons, denoted by η. Experimentally, SEY and BSC are quantified in a dedicated setup as shown in Figure 6a (17). A special hemispherical collector is used for detection. The sample is biased +50 V to restrict the escape of the SEs from the sample. The ratio of the collector current (I_{c+}) to the probe current (I_o) would simply be equal to the BSC. On the other hand, when the sample is grounded, the ratio of the collector current (I_{c-}) to the probe current would result in total electron yield (TEY) from the sample. The difference of the TEY and BSC gives SEY.

A general trend for TEY (η+ δ) in relation to primary-beam energy is shown in Figure 6b (17). Points E_1 and E_2 are the special cross-over points as at these points the number of the electrons incident on the sample equals the number of electrons leaving the surface resulting in no excess charge on the sample. These points are of special interest when studying insulating samples, such as polymers. The insulators tend to charge up when they are impinged with excess electrons or are devoid of it. This would render an SEM image uninterpretable.

The total yield increases upon decreasing primary beam energy until the cross over point at E_2, attains the peak at E_{max} and then decreases with decreasing primary beam energy. Usually E_{max} is found to be less than 1 keV in materials (18) (19). The BSC generally changes little with changing primary beam energies (1). Therefore, the contribution to the increase in the total yield at lower primary beam energies mainly comes from the SEY. This is because upon decreasing the beam energy, the interaction volume becomes shallower, higher fraction of the SEs are generated within escape depth (5-15 nm) leading to higher SEY yield till it reaches the peak value of δ_{max}.

.

The decrease in the SEY at lower energies (<E_{max}) is simply because low number of SEs are generated with decreasing primary beam energies.

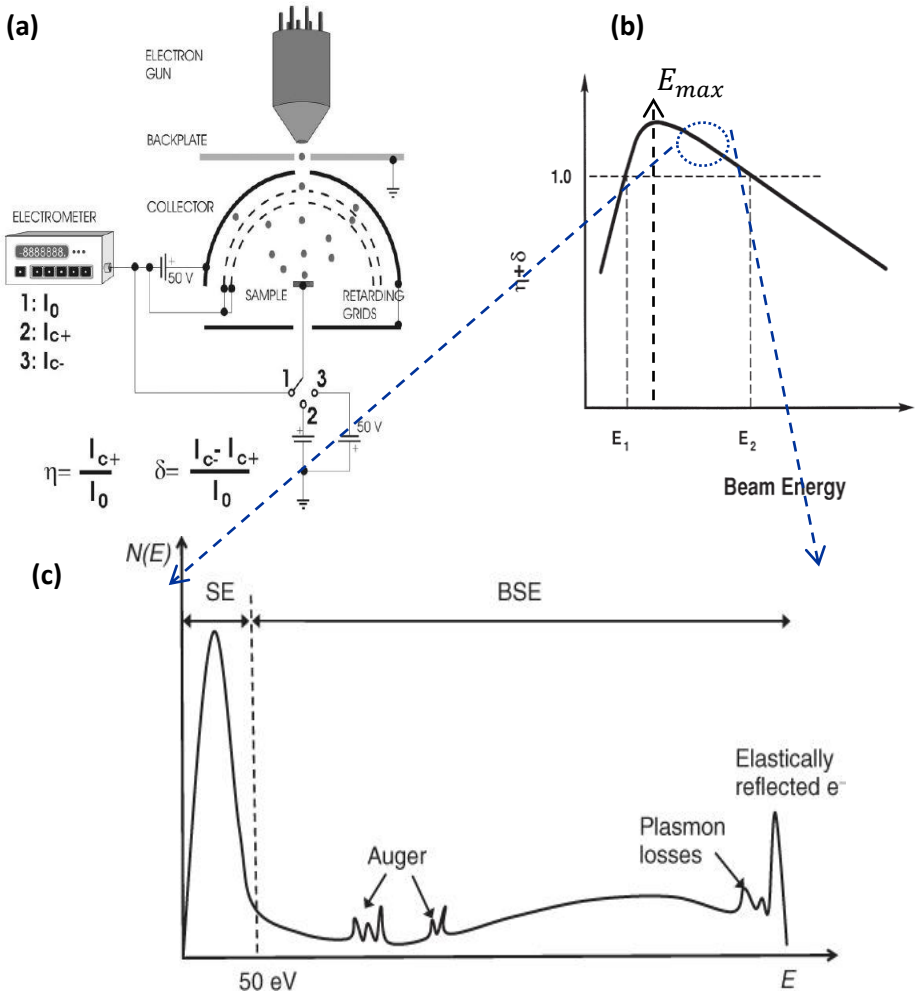

Figure 6 (a) is the detector assembly for collecting all the possible generated/scattered electrons. I_{c+} is the collector when the sample is at 50 V and I_{c-} when grounded. I_o is the probe current. **(17)** (b) Plot showing total collected electrons with respect to the primary beam energies. When the collected electrons are arranged according to their energies for particular primary-beam energy (c) **(1)**.

2.4. Energy Distribution

The detected electron energies in vacuum can lie anywhere between 0 and the maximum primary-beam energy as shown in Figure 6c and can be divided into three regions:

.

1. The peak at the lower end of the spectrum corresponds to ‘low energy SEs’. which usually have energies less than 50 eV (20). This forms the principle of estimating SEY and BSC discussed in previous section.
2. The peak at the higher end of the spectrum corresponds to the elastically scattered electrons.
3. The general background in between these peaks represent inelastically scattered electrons. The characteristic Auger features are superimposed on the background. When the spectrum is interpreted from the higher end, with elastic peak (EP) as 0 loss peak, the technique is referred to as the reflected electron energy loss spectroscopy or REELS. Losses incurred due to plasmon excitation are also superimposed on the background. The spectrum (Figure 6c) when interpreted from the lower end is often referred as the AES technique with SE peak at the lower end and auger peaks superimposed on the BSE background.

2.5. Angular Distribution

The BSEs and SEs escape the sample in a cosine distribution (20) as shown in Figure 7a and Figure 7c respectively. The BSC at an angle α with respect to the surface normal is given by:

$$\eta = \eta_o \cos(\alpha)$$

2. 11

where η_o is the BSC at $\alpha = 0^o$. This implies that most of the BSEs escaping the sample are concentrated very near to the surface normal. Similarly, the SEY at an angle α with respect to the surface normal is given by:

$$\delta = \delta_o \cos(\alpha)$$

2. 12

where δ_o is the SEY at $\alpha = 0^o$.

.

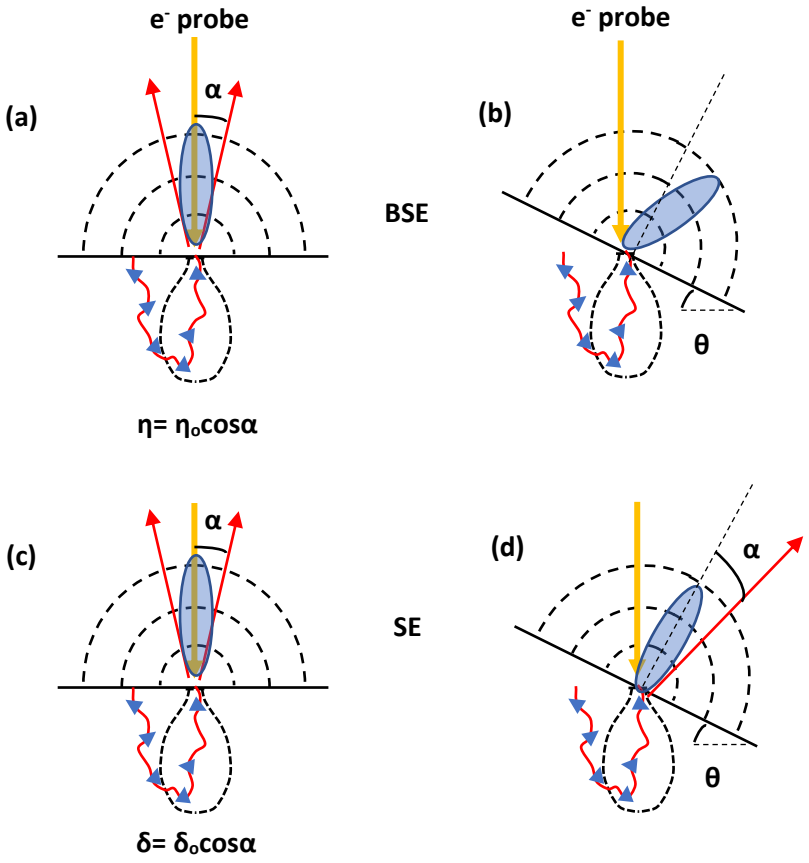

Figure 7 (a) Cosine distribution of emitted BSEs for sample at 0^o tilt, for the sample tilted at an angle θ (b). Isotropic emission of SEs for sample at 0^o tilt (c) and for the sample tilted at an angle θ (d).

The BSE angular distribution becomes asymmetric about surface normal when the sample is tilted at an angle θ with respect to the beam axis as shown in Figure 7b. Tilting the sample further results in the increase in forward scattering. In the case of SEs, a cosine distribution exists with respect to the sample normal, which is not the same as the beam axis anymore (Figure 7d). This is owed to the near-isotropic nature of the SE generation in the sample at higher beam energies. The SE emission increases with the tilt angle as cosec(θ). This is the reason why local variations in the topography of the sample results in the brighter edges in the SEM images. This is termed as an 'edge effect'.

.

2.6. Auger Electron Emission

Auger electrons are special type of SEs that contain chemical signature of the element under study, discovered by French physicist Piere Auger in 1925. A fast-moving electron ionises an inner shell electron which results in another electron from the higher shell to occupy the vacant site and the excess energy is dissipated through, either the emission of an X-ray photon or an Auger electron. This is summarised pictorially in Figure 8 .

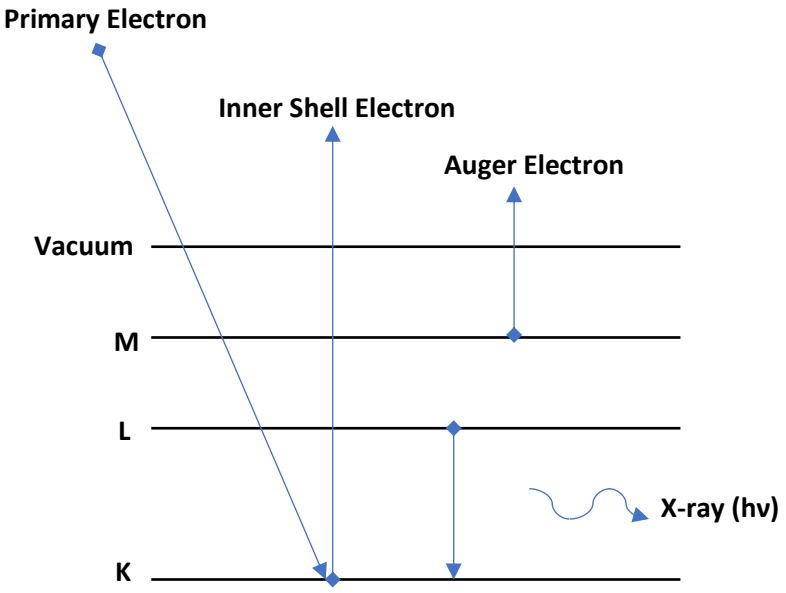

Figure 8 Pictorial representation of the excitation of inner shell electron and subsequent relaxation by an Auger electron or an X-ray photon.

Assuming an electron is ionised from K shell, and an electron from L shell occupies this hole. This, followed by the release of an electron from, say M shell, then this Auger emission would be described as KLM Auger transition. Similar process involving other shells may include KLM, LMM transitions and so on. If the electron from higher subshell occupies the vacant site corresponding to L_1L_2M transition, is the special case of Auger process called Coster-Kronig transition (21), named after their discoverers in 1935. If the emission of the Auger electron is also from the same shell then it is called super Coster-Kronig Auger transition (e.g. M_1M_2 M_3). The energy of electron (E_A) for KLM transition would be given by:

.

$$E_A = E_K - E_L - E_M$$

2. 13

where E_K, E_L, E_M are electron binding energies for K, L and M shells respectively. If the atom relaxes by releasing a photon instead, the energy $h\nu$ is given by:

$$h\nu = E_K - E_L$$

2. 14

The Auger emission and X-ray emission are competitive processes, while former is radiative, latter is a non-radiative means. The Auger yield w_A is related to the X-ray yield w_x by:

$$w_A = 1 - w_x$$

2. 15

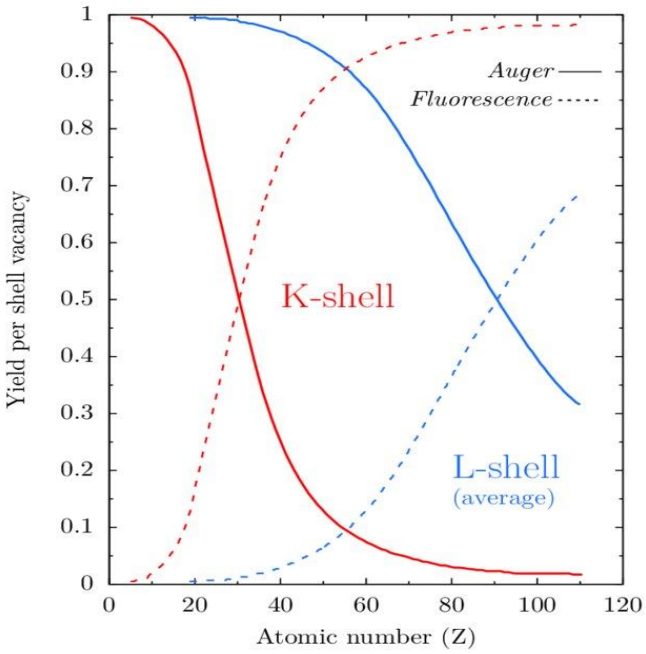

Figure 9 Relative Auger and X-ray emission yields shown for K and L shells. The image is reproduced from **(22)**.

The relative yields as a function of atomic number are shown in Figure 9. As can be seen, the auger emission dominates for K-shell excitations for Z< 31 whereas X-ray emission is stronger for heavier elements. Similarly, L-shell Auger transitions are

.

dominant for lighter elements for almost all elements. As previously discussed, because of shorter Auger escape depths, AES detection requires clean surface for the duration of the experiment. Therefore, it is always carried out in a UHV system. No such restriction is imposed for the X-ray photon detection and is used as the technique for the elemental identification in high vacuum systems such as SEM. This work advocates AES detection in an SEM environment as a complementary technique for chemical information by detecting Auger peak positions and exhibiting comparatively superior spatial resolution.

While the energy of the Auger electron is independent of the primary beam energy, which was fundamental in their discovery, the Auger electron yield in turn depends on it. This is because the ionization cross-section depends on the exciting beam energy and can be expressed as a ratio of the beam-energy to the critical ionization energy.

2.7. Summary

This chapter presented a qualitative understanding of the electron-solid interaction and the emanated entities as a result of it. It is shown that the secondary and auger electrons escape from few mean paths from under the surface and therefore are sensitive to the surface composition. The X-ray and the Auger electron provide chemical signature of the sample under study. The information depth also tells us that the Auger electrons offer a superior spatial resolution as opposed to the X-ray detection for the elemental identification. Since, they are a competitive process, the application of both the techniques would be helpful in improving the spatial resolution of the SEM instrument. The BB detector described in this thesis aims to detect SEs for microscopy and Auger electrons for elemental identification in an SEM.

.

Chapter 3: Instrumentation-SE Detection and Energy Analysis

The concepts of electron-solid interaction discussed in chapter 2 explain the ubiquitous nature of SEs. A photon or a fast-charged particle leads to emission of electrons from an element. The phenomenon of SE emission in applications such as satellites and particle accelerators etc. are undesirable and potentially can cause problems in the functioning of these instruments. A significant effort goes into minimising SE emission, for e.g., from the metal-parts in these instruments. On the other hand, instruments such as SEM and SAM use the very same principle of SE emission for microscopy and spectroscopy applications.

The main focus of the thesis is to design a detector for the SE electrons in an SEM environment. The current chapter delves into the basic building blocks of a scanning electron microscope. Subsections focus on the description of state-of-the-art SE detectors and SE imaging. An overview of the historical perspective of AES and SE spectroscopy is followed with a brief review of the most commonly used energy analysers. Overall, it highlights the limited energy analysis capability of the state-of-the-art SE detectors, particularly no energy analysis capability (as in an ET detector) to a limited energy analysis capability (as in a TTL detector).

3.1. SEM Construction

The history of SEM development is closely linked with the development of another electron microscope: transmission electron microscope (TEM). A TEM generates an image by detecting electrons diffracted from atoms in the transmission mode. The conceptualisation of the first electron microscope in 1932 by Max Knoll and Ernst Ruska was in fact a TEM (23). It was 3 years later in 1935 an SEM prototype was demonstrated by Max Knoll. Thereafter, developments in 1940s and 50s were carried by Vladimir Zworykin for RCA instruments in the US, Richard Oatley in Cambridge (24) and JEOL in Japan, helped towards the SEM commercialisation. Meanwhile,

.

Ernst Ruska and others continued with the development and commercialisation of TEM for Siemens in Germany. A review of the history of electron microscope development can be found in Ernst Ruska's Nobel lecture of 1987 (25) and the SEM development in reference (26).

3.1.1. Electron Optical Column

A typical SEM construction as shown in Figure 10a, consists of an electron gun, electron-optical column and a dedicated set of electron and photon detectors (1). All the SEM components are housed in a vacuum chamber consisting of: electron optical column, specimen chamber and all other SEM components.

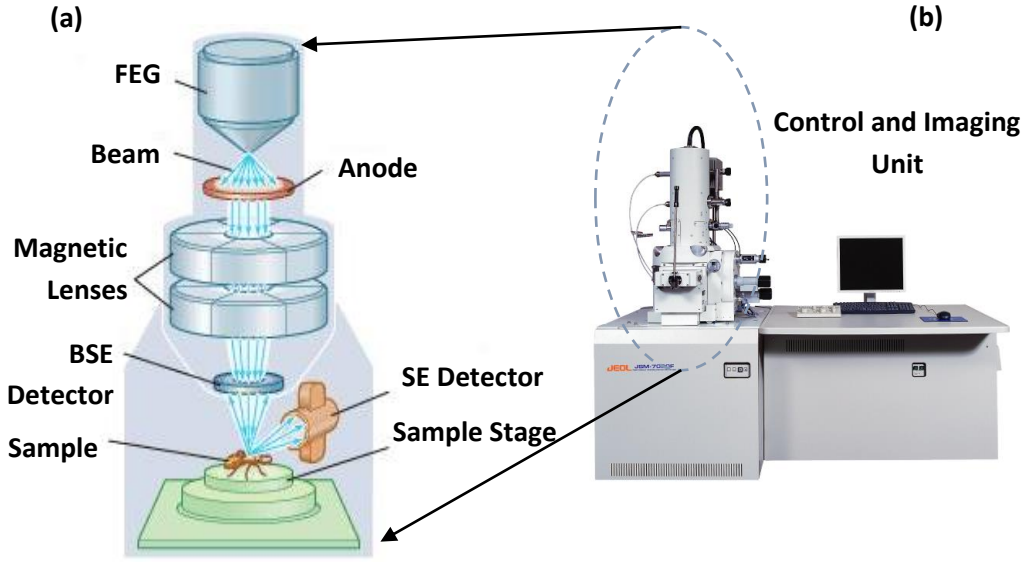

Figure 10 (a) A typical SEM Construction **(27)**. (b) JEOL 7000F FEG-SEM used in this work.

Electron Gun: The general construction of an electron gun comprises of a metal filament (e.g. tungsten) and a positively biased anode with a central aperture. Typical beam energies in commercial SEM systems fall in the range between 500 eV and 30 keV. Electron guns are classified by the type of emission mechanism they employ as: thermionic, field and thermally assisted field emission. These mechanisms are summarised in Figure 11.

To achieve electron emission, electrons must overcome the potential barrier or the work function (Φ) of the filament material. In thermionic emission, electrons may

.

overcome this potential barrier in a metal such as tungsten when provided with thermal energy (Figure 11a). Alternatively, the potential barrier can be lowered and thinned by applying high electric fields between filament and anode. This is achieved by employing a very sharp tip geometry (diameter ~1 μm). Electrons at the fermi level can now tunnel through the triangular potential barrier as shown in Figure 11c. This is called cold field emission. The third mechanism employs the principles of the thermionic and field emission. Thermally assisted field emission (TFE) as the name suggests is thermally assisted field emission. Electrons tunnel through the barrier, which is now lowered but also thinned with the application of the electric field (Figure 11b). Electron guns based on thermionic emission have the least brightness, maximum energy spread and maximum spot size among the three types. However, it is easier to fabricate and does not require UHV conditions. The FEG generates electron beam with the brightest intensity, the smallest energy spread and the smallest probe diameter. However, it requires UHV conditions which increases the cost of installation and operation.

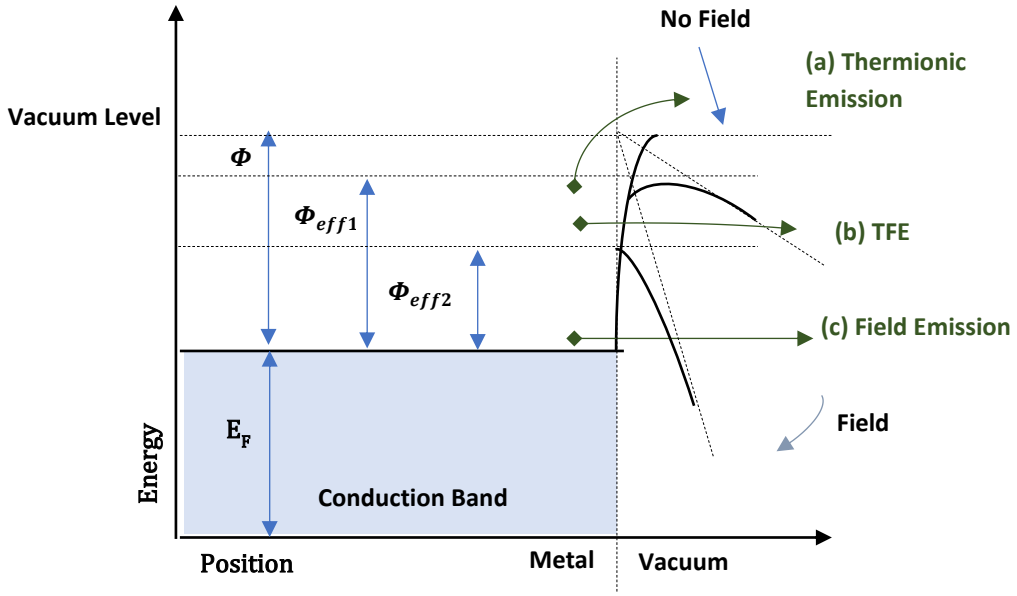

Figure 11 Band bending and the corresponding mechanisms of electron emission from a metal-vacuum interface in (a) Thermionic emission (b) Thermally assisted field emission (c) Cold Field emission.

.

Lens System: The electron beam leaving the gun has a certain size in the transverse direction of its propagation. This is demagnified and focussed on to the sample by condenser lens and an objective lens.

Stigmators: Due to factors like beam misalignment and mechanical asymmetry of the lens pole-pieces, the primary beam has an elliptical shape which is corrected by yet another electron-optical element called stigmators.

Scanning System: A deflection system just before the objective lens, scans the electron beam on the sample in a raster fashion. The scanning rate along with the scanning area can be set in the computer-controlled system. This helps in controlling the magnification in the SEM image. These usually consists of a pair of magnetic coils corresponding X and Y scans.

3.2. SE Detectors

In Max Knoll's SEM prototype the image was generated without the use of focussing lenses and by detection of change in intensities of the sample to ground current, but the prototype demonstrated the scanning (200 lines) and imaging capability of the instrument. However, it was Manfred Von Ardenne, in late 1930s and early 1940s, who demonstrated a focussed electron probe (~ 50 nm). Around that time, Zworkyn (28) developed copper-beryllium dynodes (electron multiplier) for SE detection. The electron (Figure 12) tubes were used to amplify low-level electron-signals resulting from photoelectric effect (29). The work by Richard Oatley's group in Cambridge, led to the development of a robust SE detector design (ET) by Everhart and Thornley in 1960 (5), which is still very popular today.

3.2.1. ET Detector

A sketch of the ET detector is reproduced from Everhart and Thornley's work (Figure 12). The ET detector attracts SEs from the sample by positively biasing (50-300 V) the front cage which encloses a scintillator biased at a high voltage (~10 keV). The electrons accelerate and are converted into photons upon impact with the scintillator which is coupled with a light pipe. Eventually the optical signal is again amplified using a photomultiplier and converted to an electronic signal for imaging.

.

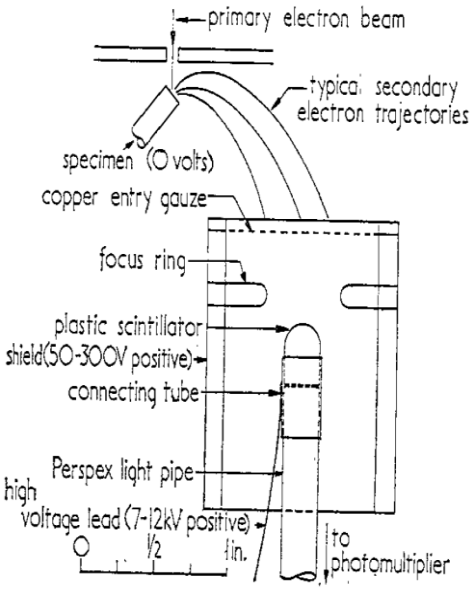

Figure 12 A sketch for an ET detector. The image is reproduced from **(5)**.

Although, it has been a popular choice for several decades, the application of the positive voltage results in the detection of SEs over a broad energy range along with some of the BSEs. In doing so one loses crucial energy information. Furthermore, some of the BSEs striking the chamber walls produce SE IIIs which is also detected by the ET detector. This degrades the signal (i.e. the 'true SEs' emanating from the sample) to noise ratio.

3.2.2. Through-the-lens Detector

More recent developments in SE detection include the in-lens or through-the-lens (TTL) detection mechanisms, in which the SEs are extracted through the electron-optical column for detection as shown in Figure 13 (1). The sample is immersed in a high magnetic field of the objective lens. The emerging SEs spiral upward inside the electron column due to the high magnetic field and are then deflected onto by a detector using deflection fields. The major advantage of TTL detector is that it avoids SE III detection (Figure 13). However, TTL detectors require dedicated SEM column design, often a proprietary of the manufacturer, who does not provide much flexibility to the end user. Most modern SEMs are equipped with both SE detectors: ET and TTL, sometimes are referred to as lower electron detector (LED) and upper electron detector (UED) respectively.

.

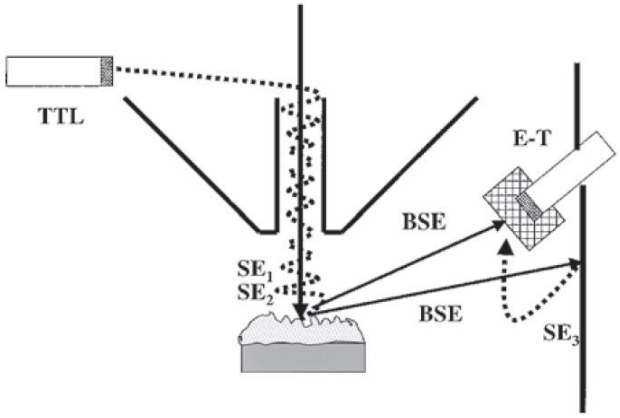

Figure 13 Shows the schematic of the position of ET and TTL detectors with respect to the objective lens. TTL avoids SEIIIs and detects SEI and SEII as opposed to ET detector which detects all three SE types along with some of the BSEs. Image a is reproduced from **(1)**.

3.3. SE Imaging

The electron beam is raster scanned across the sample and the image is generated by detecting signal intensities resulting from electron-solid interaction, discussed in chapter 2. A single pixel in the image corresponds to a single point on the sample. Thus, the SEM magnification is simply the ratio of the physically scanned length to the pixel length. SEM systems employ electron detectors for BSEs and SEs and some level of SE energy analysis may be present. However, AES detection is never employed by commercial manufacturers. State-of-the-art SE detection and energy analysis is discussed in the subsequent sections. X-ray detectors are used to perform spectroscopy (EDS) for elemental identification and microscopy (elemental maps). The SE imaging using the BB detector is discussed in chapter 6.

3.3.1. Contrast Function

SEM images are interpreted by relating the grey levels to the characteristics of the sample. An image contrast occurs when there is a difference in the grey level intensities between the region of interest from other parts of the sample. Mathematically a contrast function (C) is defined as:

.

$$C = \frac{G_2 - G_1}{G_2}$$

3. 1

given,

$$G_2 > G_1$$

where G_1 and G_2 are the grey-level intensities. By definition the contrast function is always positive and lies between $0 < C < 1$. When, C= 0, there is no contrast between the chosen pixels or points and when C = 1 corresponds to the maximum contrast with $G_1 = 0$. The interpretation of SEM images is related with understanding of the contrast mechanisms and spatial resolution of the detected entity resulting from electron-solid interaction.

3.3.2. SE Image Contrast

Conventionally, the SE generated images were interpreted to provide topographic information. Coupled with the SEM's high depth of field, almost '3D-like' images are generated. Topography contrast is the combined effect of the non-uniform SEY at various location on the sample and the collection efficiency (which is affected by the line of sight) of the SE detector. From the discussion on SE angular distribution in chapter 2, it is known that the SEY increases with the localised tilt in the sample of a rough surface with edges appearing brighter and difficult to resolve. Lowering the primary energies eliminates this effect and the edges become easier to resolve. Tilting the sample can enhance the topographic contrast owing to the angular variations. The ET detector is located on one side of the sample and collects electrons via positively biased grid. In doing so, planes facing the ET detector appear brighter as compared to planes facing away. This difference in collection efficiency causes a 'shadowing effect'. The consequence of this is that valleys appear darker as shown in the diamond sample seen in Figure 14a. On the other hand, TTL detector exhibits uniform collection efficiency with respect to the SE angular distribution as shown in Figure 14b.

.

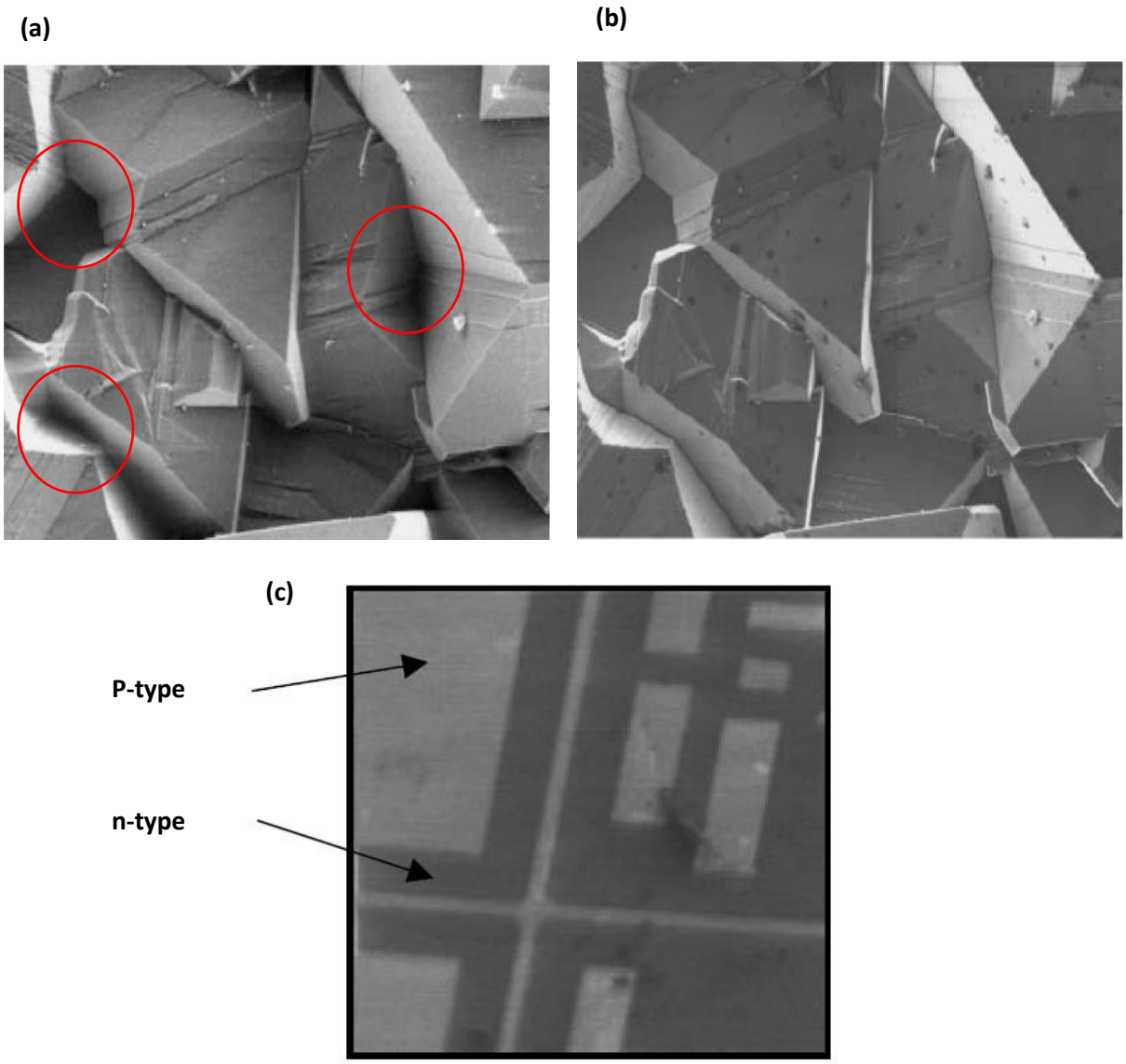

Figure 14 Topographic Contrast observed in diamond sample imaged by (a) ET detector and (b) In-lens detector imaged at 5 keV. The red circles in ET image correspond to the shadowing effect. The image is reproduced from **(16)**. (c) shows dopant contrast with p-type brighter than the n-type substrate imaged at 0.7 keV. The image is reproduced from **(30)**.

For samples devoid of topography, some level of compositional contrast is also reported with low primary beam-energies. The fact that the beam interacts very near to the sample surface and the dependence of the probability of SE escape from the surface depends on electronic properties such as the local work-function, work-function mapping in graphene (31), layer counting in 2D materials (32) etc., have demonstrated promising results. One of the extensively researched area is of the

.

dopant contrast (30), where a contrast between p-doped features is seen with relation to n-doped well in semiconductor substrate (such as silicon), can be seen in SE images (p-doped is brighter in Figure 14c).

3.4. SE Energy Analysis

The energy distribution of the emanated SEs resulting from electron-solid interaction discussed in chapter 2 (Figure 6c) comprises of low energy SE peak and characteristic Auger features in the form of peaks and 'shoulders' on the background. As discussed in chapter 2, Auger electrons escape from few mean free paths from the solid. Therefore, Auger detection provides surface information and is used extensively as a characterising tool in surface science experiments. Being a surface technique AES demands the sample surface is free of impurities. Experimentally, this is achieved by in-situ cleaning and UHV conditions.

3.4.1. Vacuum Conditions

Vacuum is created in a volume by pumping out the gas molecules. It is generally classified with respect to the gas pressures as low vacuum ($P_{Vacuum}<10^{-2}$ Pa), high vacuum ($10^{-2}<P_{Vacuum}<10^{-5}$ Pa) and ultra-high vacuum (10^{-6} Pa$<P_{Vacuum}$). According to the kinetic theory of gases. the pressure is defined as the force exerted by the gas molecules hitting the chamber walls which depends on the molecular density of the gases, temperature and volume of the chamber. Decreasing the chamber pressure increases the mean free path between collisions of the gas molecules and therefore has direct impact on the time duration to form a monolayer of impurity on the surface of the sample. Number of atoms (N_a) hitting a unit area of surface per unit time is given by (33):

$$N_a = RP\sqrt{(M_t T)} \qquad 3.\ 2$$

where P and T are the chamber pressure and temperature respectively. R is universal gas constant = $8.314\ Jmol^{-1}K^{-1}$, M_t is the molecular mass. For a gas say, Nitrogen

.

at room temperature, the time taken for a monolayer to form on, say, 10^{15} cm^2 target site is estimated to be:

$$t = \frac{4x10^{-2}}{P} \qquad 3.3$$

where P is expressed in Pa. For quantitative AES measurements, it is desirable for the experiment duration to be less than the time taken for the monolayer formation. Table 1 summarises approximate time scales for the monolayer formation on sample with a unit sticking coefficient (i.e. all the gas molecules hitting the sample stick to the sample). AES systems are often coupled with in-situ sample preparation and cleaning through heating or ion bombardment is often carried out before an AES measurement.

Vacuum	**Pressure**	**Time for Monolayer**
Low	$>10^{-2}$ Pa	<4 s
High	10^{-4} Pa	40 s
Ultra High	$<1x10^{-6}$ Pa	>100 min

Table 1 Typical nitrogen monolayer formation times corresponding to the pressure ranges of LV, HV and UHV conditions.

3.4.2. Auger Electron Spectroscopy

Some of the earliest spectroscopic experimental work was undertaken by Eric Rydberg with Au, Ag and Cu metal targets, demonstrating low-loss and elastic peaks in 1930 (34) and a complete spectrum in 1936 (35). The use of low primary beam energies (150 eV) and poor vacuum conditions ($>5x10^{-4}$ Pa) did not allow for the detection of Auger features in the spectrum. JJ Lander and few others before him observed features in the spectrum from variety of targets (C, Al, Ni, Cu etc.). He attributed these features to the Auger effect in 1953, 30 years after the discovery of Auger effect. The experiment was carried out at ~800 eV primary-beam energy and in better vacuum conditions ($5x10^{-5}$ Pa) than the previous reports. This was the beginning of AES. However, its potential as a surface analysis technique was explored at General

.

Electrics in 1967 with the efforts by Harris (36) who prepared (sputtering) and cleaned (heating) the samples in-situ before examining them with an electron probe. Weber (37) integrated AES with the existing surface science technique: low energy electron diffraction instrument (LEED). In the LEED technique, a low energy probe is used to project a diffraction pattern from the elastically scattered electrons onto a scintillator screen. This helped in establishing it as an important technique for surface analysis. Weber made use of the UHV conditions for his experiments (~$1x10^{-7}$ Pa).

This was immediately followed by the integration of AES with SEM and led to the development of a dedicated system by Macdonald and Waldrop in 1971 using a cylindrical mirror analyser (CMA) designed by Palmberg, Bohn and Tracy (38) . These key developments were carried out at PHI-systems (a spin-off company from University of Minnesota) which eventually led to the development of scanning Auger microscope (SAM). Macdonald and Waldrop's setup for the first time related a surface sensitive spectroscopic technique with an SE microscopic image. These initial experimental works were technology demonstrators and were carried out in HV environment similar to specimen chamber pressures in SEM. In fact the Auger spectra acquisition in these works are the first and more recently by El-Gomati, Walker and Zha in 2011 at University of York (39) very few reports on the AES detection in an SEM.

Subsequent Auger analysis by researchers were carried out exclusively in UHV environment with a focus on quantification of Auger intensities. The focus was also laid on the design and implementation of high performance Auger analysers in SAM such as CMA by Palmberg at PHI-Systems and concentric hemispherical analyser (CHA) by Bassett, Gallon and Prutton (40) at University of York. This coupled with the scanning capability of a focussed probe and software algorithms helped in generating elemental Auger maps with nanometre resolution (41). The detectors used for Auger analysis are termed simply as Auger spectrometers and for low energy SE energy detection are termed as SE or SEM spectrometers.

.

This work makes use of the BB analyser for the AES technique. The Auger spectrum acquired in UHV environment is discussed in chapter 5 and the one acquired in SEM environment (HV) is discussed in chapter 6.

3.4.3. Secondary Electron Spectroscopy

Meanwhile, SEM became an important tool for imaging at nano meter scale. One of the applications that spearheaded SE energy analysis' popularity was non-destructive characterisation of semiconductor devices. Electron beam testers (EBT) became dedicated instruments which employed SE spectrometers in SEM for the quantification of voltage contrast (42). First pointed out by Oatley and Everhart in 1957 (43), who observed variations in the brightness of an SE image with the changes in the bias of a reverse-biased p-n junction. In general. the SE trajectories emanated from the region of interest on the sample are affected by the presence of electric fields above the sample. Biasing, say a specific region positively with respect to the surroundings results in the region appearing darker in the SE image and vice versa. This is termed as 'voltage contrast' and is a consequence of the change in the number of electrons arriving at the detector due to potentials above the sample surface. SE energy analysis was proposed by Wells and Bremer in 1968 to quantify this effect (44). This was needed because of the difficulty in determining the nature of surface and ambient fields. SE analysers are employed to observe the shift in the SE peak in-correspondence with the bias given to the sample. Localized defects and grain boundaries in crystalline samples or discontinuities in a conductive layer in semiconducting devices have been detected in SE images. This is achieved by applying transverse electric fields in-situ to the sample inducing a voltage contrast in SE images at the defects (45).

More recent interest in SEM energy analysis is rooted in energy-filtered scanning electron microscopy (EFSEM). Recent experiments with the generation of energy-filtered images, allowing electron detection for a fixed, narrow band of SE energies, has furnished the relative-compositional information due to a difference in the SEY at the filtered energy (16).

.

3.5. Electron Energy Analysers

An electron energy analyser or an electron spectrometer is a detector-device used for experimental energy analysis of the emanated electron. It detects number of electrons (intensity) as a function of energy. The design of a charged particle energy analyser is governed by the principles of electron-optics: a charged particle such as an electron changes its trajectory under the influence of electrostatic or magnetic field. The force exerted by the electrostatic fields is in direction of the net electric field and the force exerted by the magnetic fields is perpendicular to the direction of motion and the net magnetic field.

One class of analyser design employs retarding fields and offer a potential barrier preventing electrons with energies lower than the barrier from detection, effectively acting as a high pass filter. Another major class of energy analyser employ deflecting fields. The fields cause dispersion of incident electrons into their respective energy components (Figure 15).

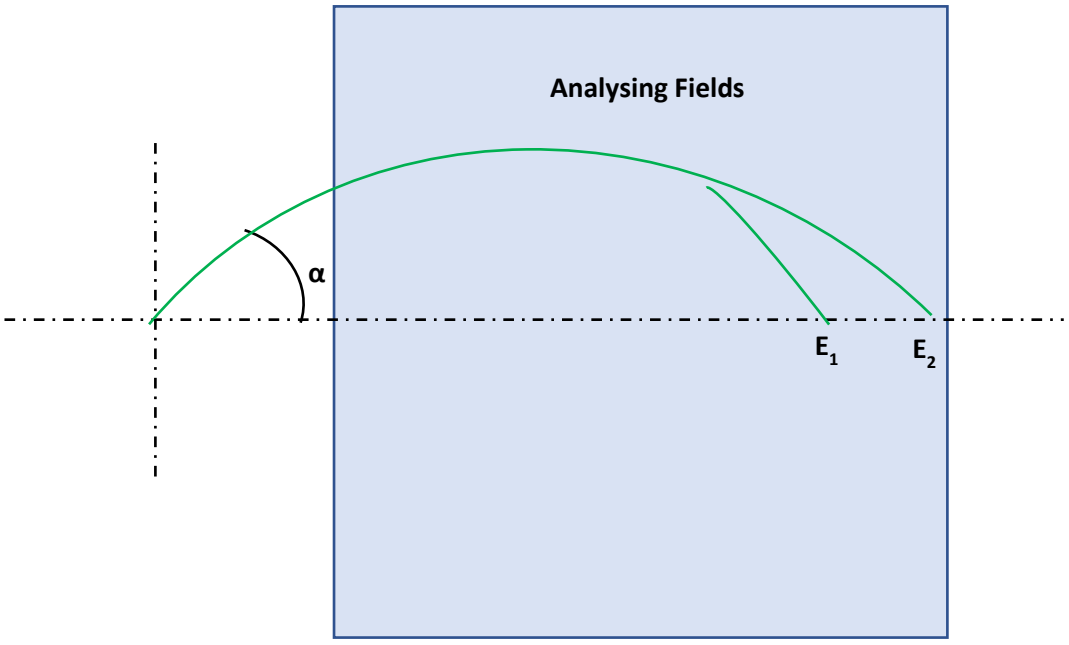

Figure 15 A narrow band of energies can be collected with the application of an output aperture. This is further elaborated in chapter 4 with reference to the BB analyser design.

.

An important classification stems from total analysing times as serial and parallel acquisition analyser. Serial analysers disperse incident electron trajectories into respective energy components and detect narrow band of energies in a serial manner. In parallel acquisition, discrete electron trajectories can be detected at the same time. The computing times can be reduced as a factor of number of collection channels using position sensitive detector such as multi-channel plates.

3.5.1. Retarding Field Analyser

Weber used a 3 grid retarding field analyser (RFA) to integrate AES with LEED technique, as shown in Figure 16. Usual construction of RFA comprises of four concentric hemispherical grids coupled with a scintillator screen at high bias. The 2 outermost grids are grounded to prevent field penetration to the sample. The two inner grids are shorted together and biased negatively closer to the Auger energy of interest. The use of two grids helps in avoiding focussing effects on electrons due to field non-uniformities in region between grid-mesh. Electron energies greater than the potential barrier are transmitted through the analyser for detection, essentially making RFA as a high-pass filter. A small amplitude AC bias is superimposed on top of the retarding voltage to reduce the influence of the background electrons by doubly differentiating the output signal.

Although RFA has a resolution for 0.5-1%, adequate for AES, the major drawback with RFA is the low signal to noise ratio. This is because of the high-pass nature of the analyser and the increase in shot noise resulting from scattering of high energy BSEs from the RFA grids.

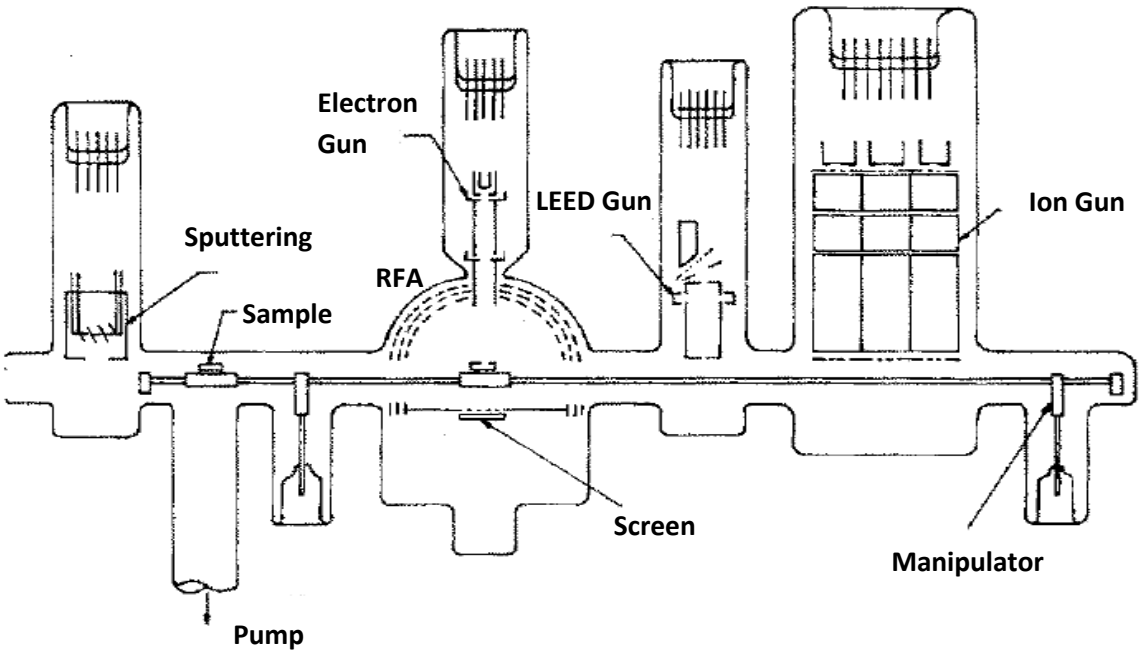

Figure 16 Weber's experimental setup. RFA was used for Auger analysis. The image is reproduced from **(37)**.

3.5.2. Cylindrical Mirror Analyser

The commercially available PHI SAMs, discussed earlier, made use of cylindrical mirror analyser (CMA) developed by Palmberg in 1969 and described by Sar-el (46) in 1967. A general construction of CMA as deployed in SAM is shown in Figure 17. CMA essentially is a cylindrical capacitor consisting of 2 concentric cylinders of radius R_1 and R_2 with the symmetric axis same as the SAM's optic axis. The sample and the detector are placed on the optic axis at a distance L from each other. The input and output apertures are defined on the grounded inner cylinder which is large enough to house the electron optics. The outer cylinder is biased negatively to focus the electrons emanated from the sample. The relationship between the pass energy (E)and the voltage applied (V_{cyl}) to the outer cylinder is given by:

$$E = \frac{k}{R_1}\frac{V_{cyl}}{ln\left(\frac{R_2}{R_1}\right)} \qquad 3.\ 4$$

.

where k is a constant that depends on the distance L between the sample and the detector. CMA can be designed for different entrance angles but for the special case where central angle equals α = 42.18°, the CMA is operated in the second order focussing regime. For this condition the value of k equals 1.3099. For the best performance with regards to energy resolution and the signal sensitivity, second order focussing allows input apertures to be are designed to allow entrance angles within the scale of $\Delta\alpha$ = ±6° about the central angle of 42.18°. This allows minimum degradation to the relative energy resolution. CMAs are designed to achieve second order focussing. The relationship between the relative energy-resolution with respect to small angle spread ($\Delta\alpha$) depend on the 3rd order, given by (46):

$$\frac{\Delta E}{E_o} = 2.75(\Delta\alpha)^3 \qquad 3.5$$

CMAs have been extremely popular in AES owing to their high collection efficiency, banking on 360° polar collection and ±6° azimuthal collection giving a total collection efficiency of 14% with relative energy resolution of 0.3%. The main disadvantage of the CMA is high sensitivity of the axial position of the sample.

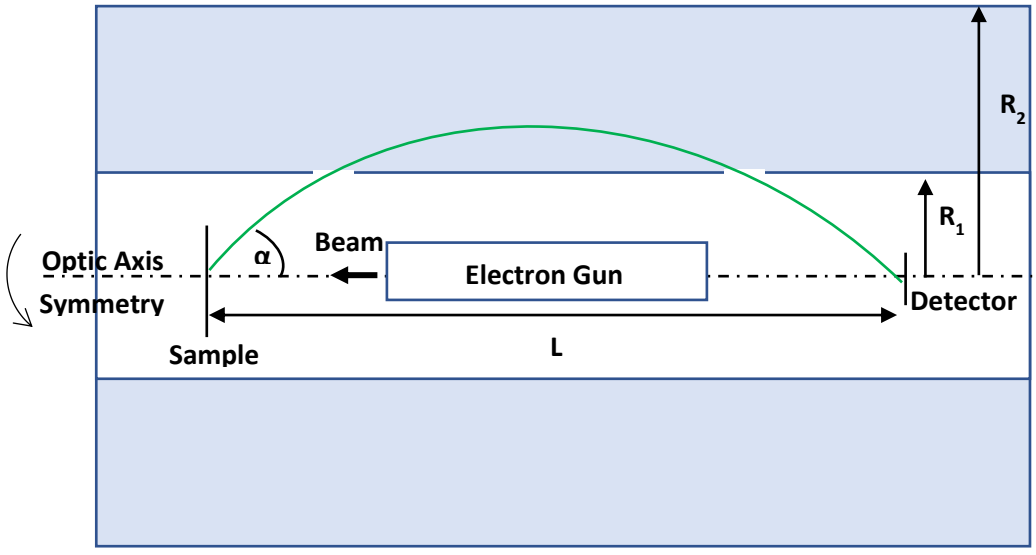

Figure 17 Schematic of CMA where L is the distance between the sample and detector, R_1 and R_2 are diameters of the inner and outer cylinders. The inner cylinder is grounded.

.

3.5.3. Concentric Hemispherical Analyser

CHA comprises of concentric hemispheres of radii R_1 and R_2 as shown in Figure 18. A deflection voltage (-V) is applied between the two spheres such that the outer sphere V_2 is negative and the inner sphere is positive V_1 with respect to the V applied. Input and output slits are defined on the median equipotential surface with radius R_o from the centre of curvature. Ideally, R_o equals $(R_1 + R_2)/2$. f and r are the angular and radial coordinates, respectively, of an electron of energy E_0 entering the analyser at an angle α to the slit normal (Figure 18). The relationship between pass energy E_o and the applied voltage difference is given by: (46):

$$e.V = E_o\left(\frac{R_2}{R_1} - \frac{R_1}{R_2}\right) \qquad 3.6$$

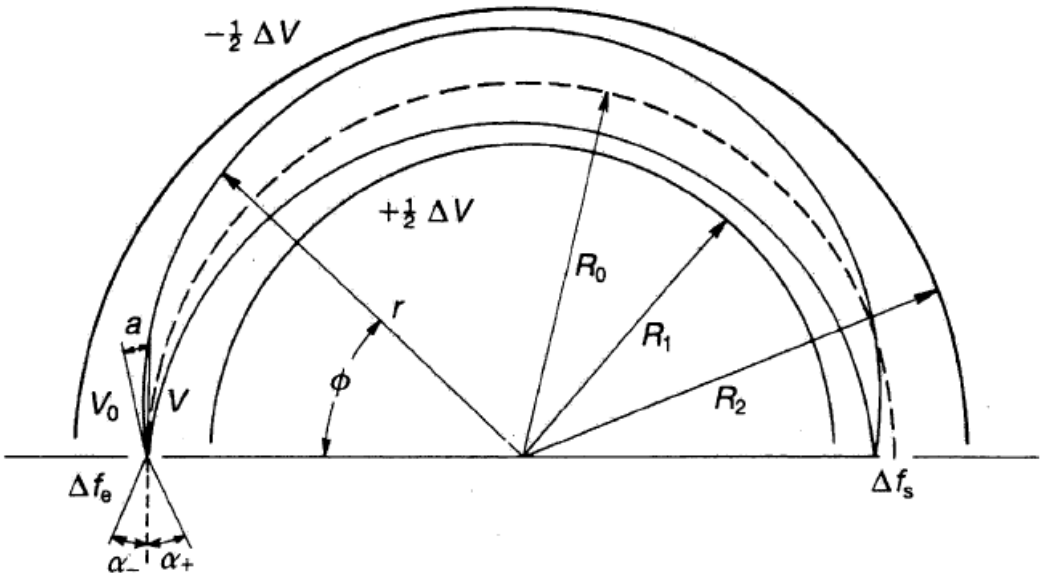

Figure 18 Schematic of CHA where R1 and R2 are the radii for inner and outer sphere respectively. Input and output slits are defined on the median equipotential surface with radius Ro from the centre of curvature.

The relative energy resolution for a first order focussing depends on the input and output slit widths (w) and the entrance angle (α) is given by (46):

.

$$\frac{\Delta E}{E_o} = \frac{w}{2R_o} + \frac{\alpha^2}{4}$$

3. 7

A higher resolution can be obtained with large radius and small slit widths. All modern spectrometers operate with a lens system to transfer electrons from the sample plane to the entrance of the CHA. A comparison of different type of analysers with respect to relative energy resolution is given in Table 2. CHA offers better energy resolution, is less sensitive to the sample position compared to the CMA.

Analyser Type	**Energy Resolution**
RFA	0.4%
CMA	0.3%
CHA	0.05%

Table 2 Comparison of energy resolution of the most popular analysers **(47)**.

3.5.4. SEM energy analysers

An electrostatic energy analyser was deployed in SEM by El-Gomati, Walker and Zha in 2011 (39). A hyperbolic energy analyser (HFA) described by Jacka (48) applied hyperbolic electrostatic fields for deflecting electrons (Figure 19a). The advantage of this analyser was that it can perform parallel acquisition reducing the analysing times. Electrons enter the HFA from a source outside the analyser given by the coordinates (-xs,-ys) as shown in Figure 19b, x_o is the distance between the slit and the origin and x_f is the landing position.

.

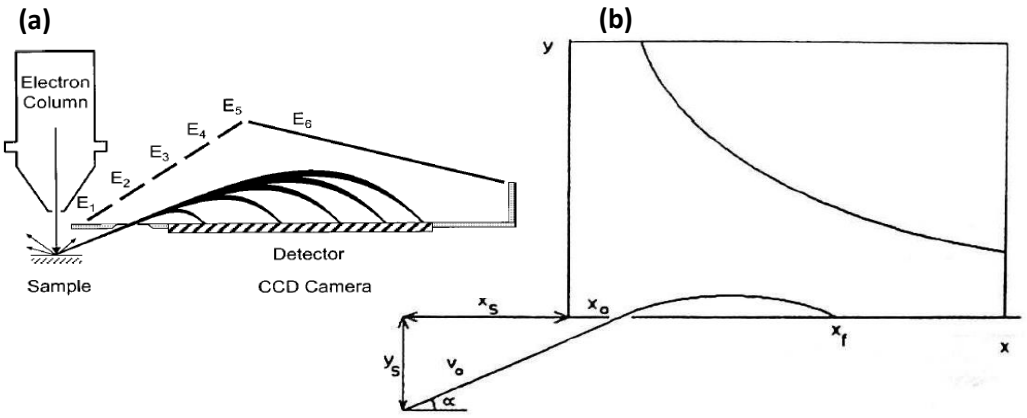

Figure 19 (a) Schematic of a hyperbolic field analyser. Fields are created by the application of potentials between $E_{1\text{-}5}$ and E_6. The image is reproduced from **(48)**. (b) Definition of the electrons entering the HFA. The image is reproduced from **(49)**.

The usual operation of the SEM analysers developed for TTL detectors involve application of extraction field for attracting SEs from the sample, magnetic field of the objective lens cause the SEs to spiral u-the column and finally the deflecting fields are employed for the collection. Figure 12 shows SE energy analysis using a TTL detector as described in (6) in FEI XL30s FEG-SEM.

The SE energy analysis in a TTL detector is carried out by creating deflection fields by a set of three layers with each layer consisting of two electrodes of opposite polarity, all located on the inside of the objective lens of FEI XL30s FEG-SEM (6), as shown in Figure 12b. The lowermost layer deflects the SE trajectories towards the scintillator while the other two layers are used to compensate for the effect on the primary beam. The voltage on the lowermost deflection electrode sets up the upper cut-off electron energy being detected. All the electron energies from 0 eV to the upper cut-off energy are detected. Thus, this arrangement acts as a low-pass filter. The extraction voltages are also employed for the higher collection of the SEs from the sample. Scanning the deflection voltage results in the SE spectrum shown in Figure 12c. The raw spectrum depicts the integral of the SE energy distribution as the total counts at a given energy are weighted as $EN(E)$ also known as the 'S-curves'. Differentiating the spectrum with respect to energy yields the expected SE curve shown in Figure 12d.

.

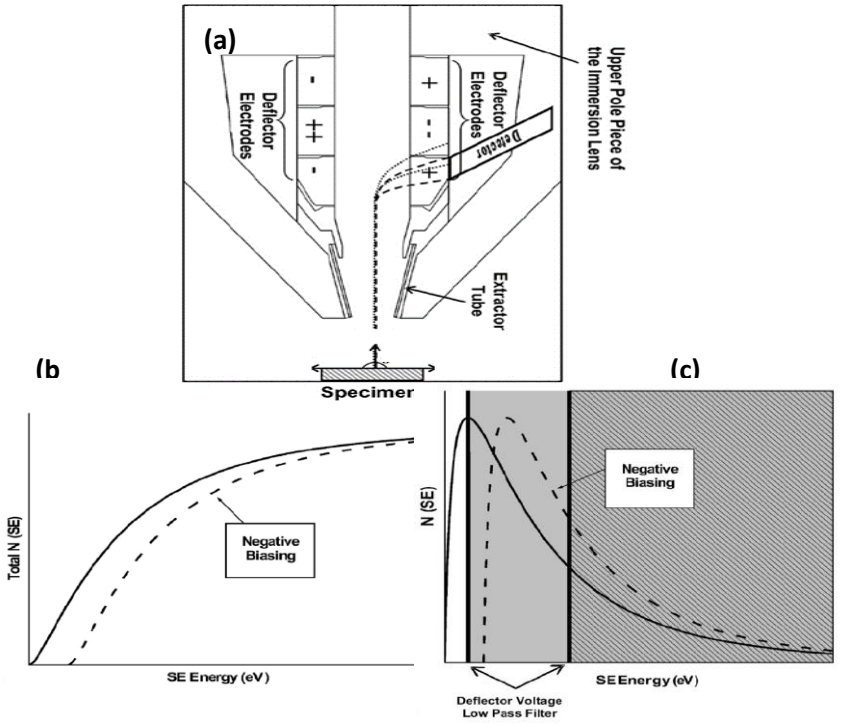

Figure 20 (a) Schematic of set of deflection and extraction electrode for SE energy analysis in TTL detector. The counts in the raw SE spectrum is weighted as EN(E) in (b) and (c) shows the differentiated raw spectrum. Negatively biasing the sample shifts the SE spectra to higher energies. Images a-c are reproduced from **(6)**.

3.6. Summary

A review of the SE detectors in SEM in this chapter show the limited energy analysis capability of the state-of-the-art SE detectors, no energy analysis capability (as in ET detector) or limited energy analysis capability (as in TTL detector). Furthermore, A review of the AES spectroscopy development tells the limited application of the AES detection in SEM. This establishes a need for the design of an improved detector for this application in an SEM environment.

.

Chapter 4: The Bessel Box: Design and Theory

The current chapter elaborates the key design principles and pre-requisites guiding the design of the BB analyzer for energy analysis in an SEM environment. The early interest in BB analyzer was triggered owing to its simple geometry. This trait has been explored in the current design. Critical emphasis has been laid on design of geometrical parameters such as input and output apertures. The findings enabled to deduce scaling parameters for designing customized BB analyzers for different microscopic systems.

The chapter is divided into 6 sections. Section 1 begins by providing a historical perspective to the design and applications of the BB analyser. This section also explains the design considerations used in this study. Section 2 provides a qualitative discussion on the potential distribution with respect to BB's geometrical parameters. This is followed by a brief discussion on analyser design principles in section 3. The simulation methodology for the design of apertures adopted in this work is discussed in section 4. This leads to the discussion on BB optics ion section 5. Finally, the chapter ends with a discussion of a miniature BB, designed as a part of University of York's collaboration with ETH Zurich for their novel SEM design.

4.1. The Bessel Box

The Bessel box is a generic name given to the class of analyser designs that employ electrostatic fields present inside a cylindrical box (Figure 21). A general construction comprises of three electrodes in the form of a central cylindrical electrode and two end-cap electrodes. Controlling the voltages on input electrode (V_{ip}), central electrode (V_{cyl}) and output electrode (V_{op}), enables the BB to analyse charged particles incident at the input aperture which are then energy analysed and transmitted through the output aperture. These apertures are defined at the end-cap electrodes.

.

4.1.1. Historical Perspective

The use of a cylindrical box as an analyser design was first proposed by Allen and his co-workers in 1972 and later described in detail in 1976 (50). It was used for the energy analysis of ions such as Ar^+, H_2^+ and O_2^+. Their design (Figure 21a) consisted of ring apertures defined at the grounded input and output electrodes (V_{ip}=V_{op}= 0 V) and a potential given to the central cylinder (V_{cyl} = U). The electron trajectories are shown in Figure 21a. One drawback of this design was the existence of the spurious peaks and features observed in the experimental spectrum. This was because grounding the output electrode resulted in the existence of alternate ion trajectories within the analyser and eventual transmission of the same. This problem was solved by Fite in 1977 by introducing a mesh with a disc as a stopper in the middle of the BB (51) as shown in Figure 21b. This design is referred to as 'modified BB design'. The stopper blocked the cylindrically asymmetric and on-axis trajectories from transmitting through the analyser and allowed an annular input aperture to be replaced by a hole aperture. The purpose of annular aperture in Allen's design was to stop on-axis electrons from detection.

The BB designs faced competition in spectroscopy experiments with other popular energy analysers such as CMA and CHA which offered superior energy resolution. Nonetheless, the simplicity of cylindrical structure and ease of fabrication resulted in it being an attractive candidate for fabricating compact analyser designs. The first micromachined energy analyser was based on an array of 4 modified BBs developed by researchers at NASA JPL in 1994 (52), although it was never a part of a flight mission. Other compact BB designs were useful to overcome the geometrical constraints in applications such as a pre-filter for quadrupole mass spectrometer (QMS) used in secondary ion mass spectrometry (SIMS); and as an ion analyser in extreme high vacuum (EHV) ion-gauges. These applications were based on the modified BB design shown in Figure 21b. The use of modified-BB as a pre-filter was first proposed by Craig and Hock in 1980 (53) which was also studied by others (54) (55). A pre-filter is used for the selection of low-energy ions as an input for QMS which improves the mass resolution of a SIMS instrument. Presently, Hiden Analytical in the UK, manufacture QMSs integrated with the BB pre-filters (56).

.

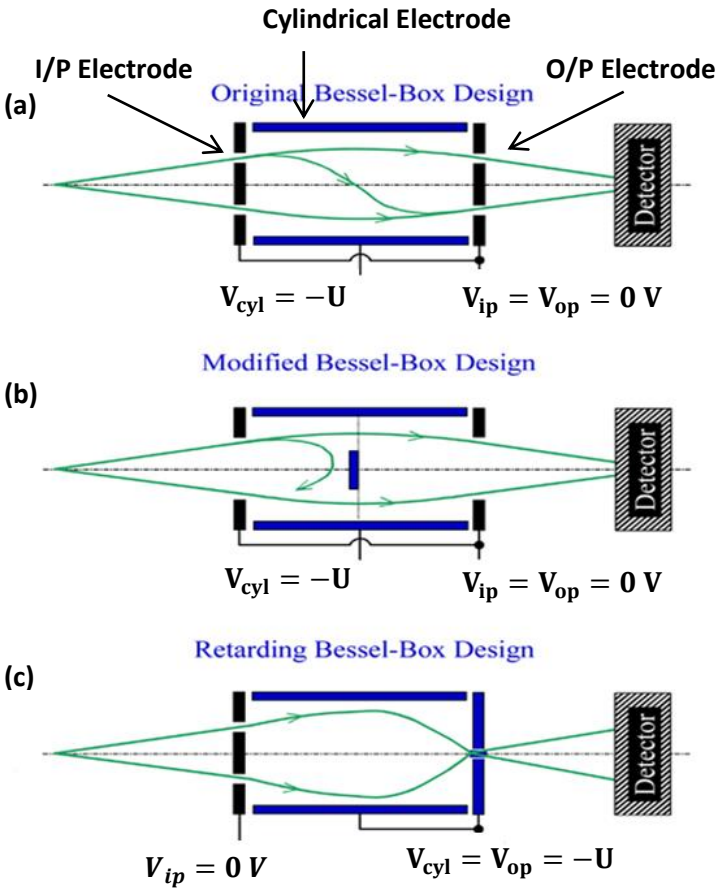

Figure 21 BB designs with electron trajectories shown in green for (a) Original BB design **(50)**. (b) Modified BB design **(51)**. (c) Retarding BB design **(57)**. These simulations were carried for the BB length of 150 mm and is reproduced from **(57)**.

As mentioned before, a modified-BB was also incorporated in the design of a hot-filament ion-gauge developed by Akimichi and co-workers (Figure 22a). This BB based ion gauge measured pressure in UHV ($<10^{-6}$ Pa) and EHV ($<10^{-10}$ Pa) regimes with a lower detection limit reported to be less than $3x10^{-12}$ Pa (58). These ion gauges are presently being sold by ULVAC corporation based in Japan (59). A hot-filament ion gauge measures low pressures by emitting electrons which are accelerated towards a cylindrical wire cage. These electrons strike the gas molecules inside the cage and ionize them. The ion current collected by the central electrode, located at the centre of the cage, is proportional to the pressure in the vacuum chamber. Usual measuring range is in between HV and UHV regimes. The lower limit of the measurement is determined by the unwanted contributions to the ionic current: outgassing of the gauge

.

materials, ions emitted from the grid and collector upon striking with filament electrons (electron stimulated absorption or ESD). The third major contribution comes from the soft X-rays generated at the surface of cage striking the collector. Akimichi and co-workers used the modified BB design before ion collector. The BB stopper helped in shielding X-rays from reaching the collector. The energy analysis of the collected ions using the BB helped in distinguishing between the ions corresponding to the chamber-pressure (ions generated inside the cage) and the unwanted ESD ions (generated at the cage) (58), as shown in Figure 22b.

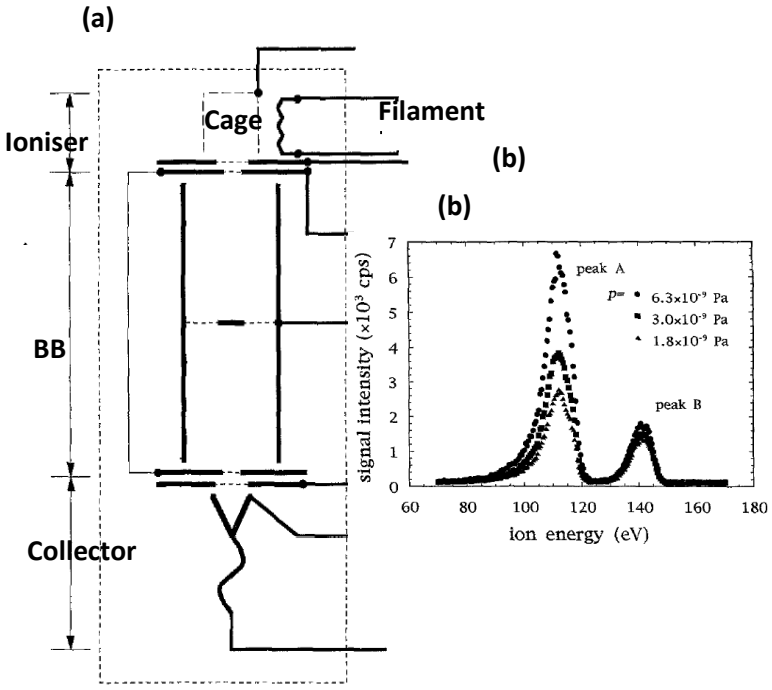

Figure 22 (a) BB based Ion gauge, (b) Shows separation of ion peaks due to potential difference in ion energies generated outside (ESD) and inside the cage. Peak A corresponds to the actual pressure changes while peak B does not. Image is reproduced from **(58)**.

The modified-BB design removed the spurious trajectories but the grid and stopper in the middle of the analyser resulted in increased scattering. In 2015, a new BB design called 'retarding BB' (RBB) was proposed and implemented by Schiwietz and co-workers for pump and probe experiments, working at German synchrotron facility located at Berlin (BESSY) (57). In this design the output and central cylinder electrodes are shorted together (V_{op}=V_{cyl} = U) and the input electrode is grounded

.

(V_{ip}= 0 V). Shorting the output and the BB central electrode together eliminates the existence of alternate trajectories without the need for a stopper in the middle (Figure 21c). This resulted in a gridless BB design with 100% transmission through the analyser. Although annular apertures are still needed to block on-axis trajectories. The total length of the analyser reported was 150 mm.

4.1.2. Design Considerations: Present Study

This study builds upon the RBB design for the development of an SE detector with energy analysis capability for an SEM. Design consideration include:

1. A compact BB design to operate in the geometrically constrained environment of an SEM: The area around the sample is crowded owing to the presence of objective lens' pole-piece, ET, BSE and EDS detectors. Sometimes auxiliary devices such as photodetectors, etc. are also mounted on the SEM.
2. Shorter working distances (10-20 mm): For the detection of high energy Auger electrons, higher voltages on the analyser are needed. This can lead to field penetration from the input aperture at the sample or the region above it, for shorter sample-to-analyser working distances. As will be discussed in the subsequent sections, a tapered input electrode geometry is considered to circumvent this problem.
3. Good energy resolution for AES detection: as a complementary technique to EDS for elemental identification in SEM, approaching to the performance of a CMA (0.3%).
4. Large depth of focus complementing to the SEM's performance: a large depth of focus ensures localized height variations in the sample have a minimal effect on analyser's performance. As an electron-optics rule of thumb, it also relates to a decrease in sensitivity to the sample's position relative to the analyser. Instead would be sensitive towards the position of the beam on the sample. This increased insensitivity to the sample position is an attractive feature, especially for a portable and add-on detector to be used over SEM variants.

.

4.1.3. SIMION 8.1: Simulation Space

This work makes use of SIMION 8.1 ray tracing package (60) which calculates potential distribution of a given electrode geometry and traces electron trajectories through it. The electrode geometry and the potentials on the electrodes and in free space are defined using the potential arrays. The SIMION ray tracing software solves Laplace equation (equation 4. 1) to calculate the potentials in-between and outside the electrodes. Subsequently, the ion-trajectories are calculated from the fields within the potential array. Three different code files were written by the author for simulating an electron-optics problem in SIMION 8.1: (1) A geometry (.GEM) file for defining the electrode geometry; (2) .Fly2 file for defining the ion's parameters and; (3) .Lua file, where the main algorithm is defined.

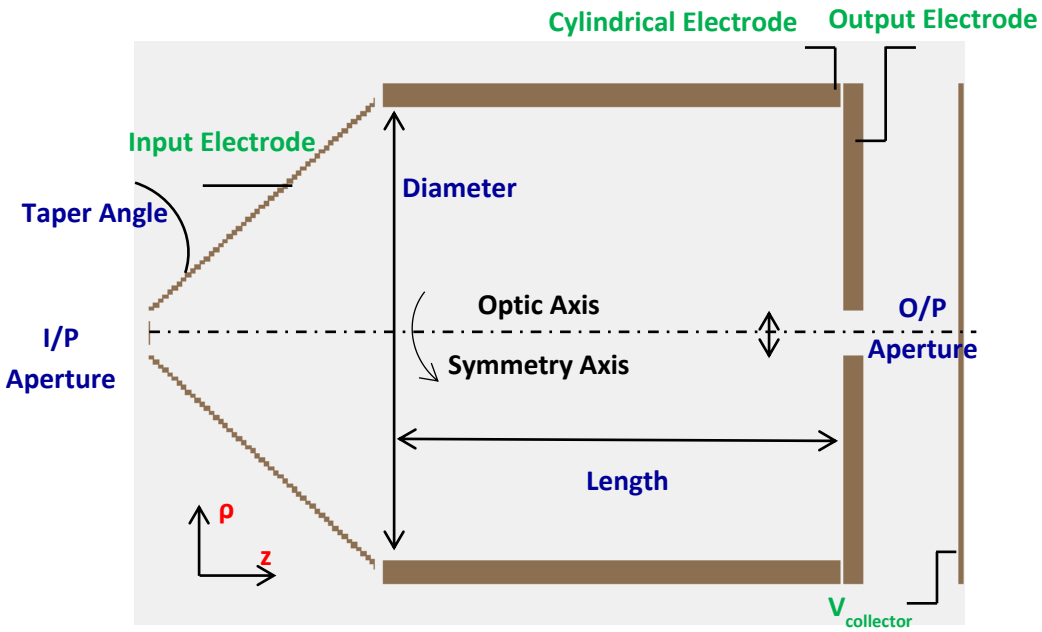

Figure 23 SIMION simulation space: shows a cross-section plane along the length of the BB. The symmetry axis of the device is the optic axis of the analyser.

A geometry file is written to define the electrodes with a mesh size of 0.01 mm for radial (ρ) direction and 0.1 mm in z-direction. Cylindrical symmetry of the device ensures reduced computational times. The geometric parameters: the BB diameter, the BB length, input/output aperture diameters, input-electrode taper-angle and the collector dimensions (in blue in Figure 23) are called in the main program accordingly.

.

This results in the user-control of these parameters in the SIMION workbench. The simulation space consists of 6 electrodes: input, output, BB electrode, output aperture grid (not shown), collector and a shielded cylinder (not shown), written in green colour in Figure 23. All the geometric parameters and voltages can be controlled independently. The actual values of these parameters are specified in the main program. SIMION also allows to simulate an ideal grid which enables 100% transmission of electrons through it, preserving the field distribution of an electrode with the same geometry. This was particularly useful in the cases where the performance of the device is to be studied without many geometrical restrictions (for example: definition of the apertures on the I/O electrodes).

In order to have total control of the shape of the electron-source in the numerical calculations, a point source is defined in particle-definition code file (.fly2). Electrons can then be fired directly at the input aperture. All the parameters pertaining to the initial conditions of the electrons are called in the main code file (.Lua). These parameters include position, direction, energy and the count. For the analyser design of low energy electrons, all the simulations were carried out for the pass energy of 10 eV electron, when otherwise specified.

4.2. Potential Distribution Inside a Cylindrical Box

The so-called Bessel Box derives its name from the fact that the potentials inside the BB depends on the modified Bessel Function. The Bessel functions are solutions to Laplace's equation (4. 1) when solved in a cylindrical coordinate system (ρ: radial, ϕ: azimuthal and z coordinate). It is a second order partial differential equation (PDE). Consider a twice differentiable and real-valued function V, the Laplace equation in Cartesian coordinates is then written as:

$$\frac{\partial^2 V}{\partial x^2} + \frac{\partial^2 V}{\partial y^2} + \frac{\partial^2 V}{\partial z^2} = 0 \qquad 4.\ 1$$

.

4.2.1. Mathematical Formalism

To exploit the cylindrical symmetry in a problem like solving the potential distribution (V) inside a conducting cylinder of finite-length and radius R, which is biased at a voltage of V_{cyl}, it is then more useful to express the Laplace equation in cylindrical coordinates:

$$\frac{\partial^2 V}{\partial \rho^2} + \frac{1}{\rho}\frac{\partial V}{\partial \rho} + \frac{1}{\rho^2}\frac{\partial V}{\partial \phi^2} + \frac{\partial^2 V}{\partial z^2} = 0$$

4. 2

An analytical solution of equation 4. 2 for potentials inside such a cylindrical box as the original BB design (both endcaps grounded) is presented in the work of Allen *et. al.* (50) and elaborated in detail in (61). For this case, the BB is a cylindrical electrode with radius R, length L, biased at V_{BB} and is terminated with grounded endcap electrodes. The boundary conditions (V_{ip}=V_{op} = 0 and $V_{cyl} = V_o$) can thus be defined as:

$$V(R, z) = V_o \; ; \;\; 0 < z < L$$

4. 3

$$V(\rho, 0) = 0 = V(\rho, L) \; ; 0 < \rho < R$$

4. 4

The potential distribution function for a given radial (ρ) and axial (z) coordinate is shown to be (50):

$$V(\rho, z) = \frac{4V_o}{\pi} \sum_{k\ odd} \frac{1}{k} \sin\left(k\pi\left(\frac{z}{L}\right)\right) \frac{I_o\left(\frac{k\pi\rho}{L}\right)}{I_o\left(\frac{k\pi R}{L}\right)}$$

4. 5

While the azimuthal electric fields are zero owing to the cylindrical symmetry of the device, radial ($E_\rho(\rho, z)$) and axial ($E_z(\rho, z)$) fields are given by the partial derivatives of the potential distribution function $V(\rho, z)$:

.

$$E_\rho(\rho,z) = -\frac{\delta V(\rho,z)}{\delta(\rho)} = -\frac{4V_o}{L}\sum_{k\ odd}\sin\left(k\pi(\frac{z}{L})\right)\frac{I_1(\frac{k\pi\rho}{L})}{I_o(\frac{k\pi R}{L})}$$

4. 6

and

$$E_z(\rho,z) = -\frac{\delta V(\rho,z)}{\delta(z)} = -\frac{4V_o}{L}\sum_{k\ odd}\cos\left(k\pi(\frac{z}{L})\right)\frac{I_o(\frac{k\pi\rho}{L})}{I_o(\frac{k\pi R}{L})}$$

4. 7

where

$$I_1\left(\frac{k\pi\rho}{L}\right) = I_o(\frac{k\pi\rho}{L})'$$

4. 8

where I_1 is the modified Bessel function of the first order of the first kind and I_o is modified Bessel function of the zeroth order, is given by:

$$I_0\left(\frac{k\pi\rho}{L}\right) = 1 + \frac{\left(\frac{k\pi\rho}{L}\right)^2}{2^2} + \frac{\left(\frac{k\pi\rho}{L}\right)^4}{2^4(2!)^2} + + \frac{\left(\frac{k\pi\rho}{L}\right)^6}{2^6(3!)^2} + \cdots$$

4. 9

The analytical expression for potential distribution obtained in equation (4. 5) is only valid for the BB design where input (V_{ip}) and output electrodes (V_{op}) are grounded (boundary conditions given by equations (4. 3) and (4. 4)). A new set of solutions for $V(\rho,z)$ is needed if any of the following changes: boundary conditions of the endcap electrode or modifications to the electrode geometry. It is much easier to use software modules such as SIMION 8,1 for the calculations of potential distribution and the electron trajectories through it.

.

4.2.2. Numerical Calculations

Consider a BB with a particular aspect ratio with length L and radius R biased at V_{cyl} = -10 V. The two end caps are grounded ($V_i = V_o = 0$ V). The voltage distribution inside the BB would then be given by the equation (4. 5). Notice, the sinusoidal term is dependent only on the z-coordinate along the length of the BB and the modified Bessel function I_o (monotonically increasing function) is only depended on the radial component. For z = 0 or L, the sinusoidal term is 0 (boundary conditions) and for $z = L/2$ the sinusoidal term reduces to 1 and the $V(\rho, z)$ solely depends on the I_o component. Therefore, the potential distribution $V(\rho, z)$ is symmetric about $L/2$.

Such a potential distribution is also calculated numerically as a function of relative length (z/L) along the BB axis. Figure 24a shows equipotential surfaces at various ρ/R values, ranging from 0 to 1 in steps of 0.2. For a plot say at $\rho/R = 0$, the potentials start at the input electrode of 0 V and increases to a maximum negative value at the centre of the cylindrical box ($L/2$) and decreases back to 0 again at the output electrode. The potentials increase with increasing radial distance from the optic axis with the highest potential at $\rho/R \sim 1$ (BB wall), as expected. The symmetric potential distribution means that the magnitudes of radial and axial fields are also symmetric about $L/2$. As previously discussed, such a potential distribution supports 0^{th} (Figure 24(I)) and 1^{st} order mode (Figure 24(II)), characterised by the number of times electrons cross the optic axis.

When the output electrode is biased at a different voltage than the input electrode, the potentials (Figure 24c) and fields are no longer symmetric about $L/2$. For the special case of the retarding BB design, wherein the central and output electrodes are shorted together ($V_{cyl} = V_o = -10\,V$, henceforth referred to as V_{BB}) the volume near the output electrode are at equipotential and therefore both the radial and axial fields are 0. Figure 24c shows the equipotential surfaces at different BB radii. Such a potential distribution only supports the 0^{th} order trajectories (Figure 24(I)). In general, an electron inside a BB experiences a non-uniform, cylindrically symmetric radial and axial fields. The radial field retards the radial velocity of the electrons and is responsible for the focusing action of the analyser. The axial fields retard the axial

.

velocity and offers a potential barrier that electrons must overcome for transmission through the BB.

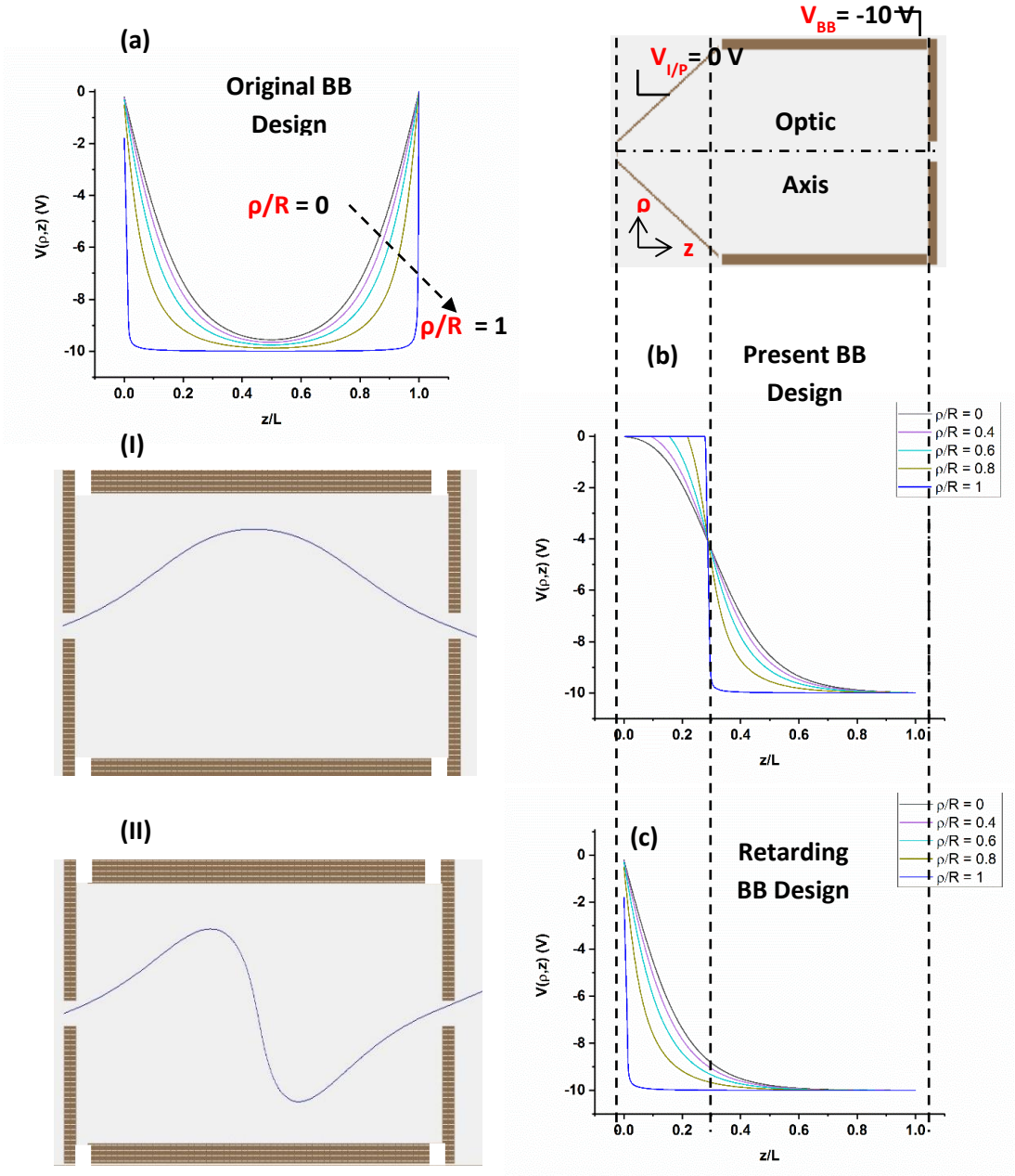

Figure 24 Shows the equipotential surfaces. The colours correspond to different radial positions within the BB for (a) original BB design, (b) compact retarding BB design (this work) and (c) retarding BB design. Electron trajectories for the fundamental (I) and first order mode (II) in the original BB design.

.

The potential distribution and hence the focussing action of the BB depends on its aspect ratio (AR, length to diameter ratio). Figure 25(a-d) shows simulations carried out to study the effect of the BB (V_{BB} = -10 V) aspect ratio on the focussing position of the electron trajectories with respect to a fixed distance from the BB input. A monochromatic electron source with energy 10.1 eV and angular spread of (±15^{o}) is simulated for BB geometry with AR 1,1.75, 4 and 10. Increasing the AR, say from 1 (Figure 25a), results in the increase in equipotential volume near to the output electrode. Incident electrons now experience higher potential gradients, retarding them towards BB optic axis. This reduces the focal distance with respect to the source situated at the object plane, as can be inferred from Figure 25(a -d). When the aspect ratio is increased to a factor of 10 (Figure 25d), a practical case for a Faraday cup design (62), nearly, entire volume of the BB is at equipotential, focussing a 10.1 eV electron just inside of the BB.

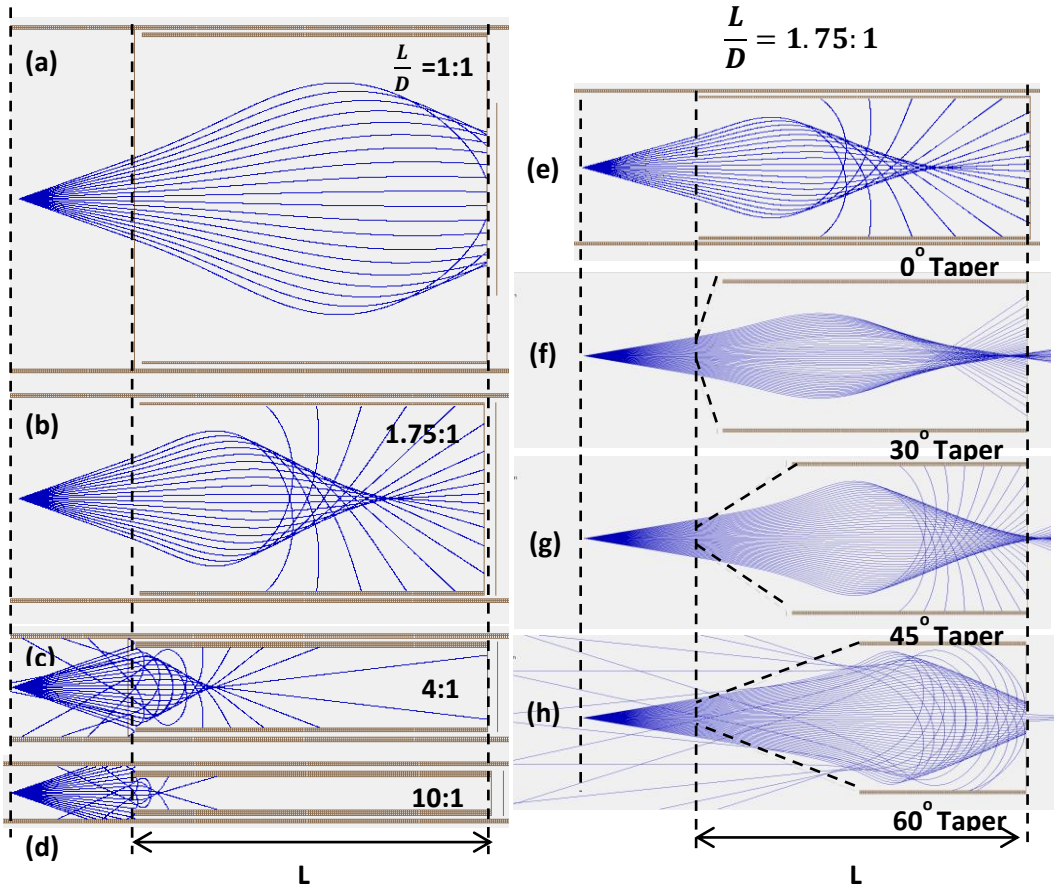

Figure 25 Simulations of electron trajectories carried out by the author for 10.1 eV electron with V_{BB} = -10 V, for AR (a) 1 (b) 1.75 (c) 4 and (d) 10 and with a constant

.

AR = 1.75 for tapered input electrode geometries with angle (e) 0^o (f) 30^o (g) 45^o and (h) 60^o.

Now, keeping the AR and length L constant but modifying the input electrode's geometry to a tapered one, perturbs the potential distribution inside the BB. Figure 24b shows equipotential surfaces at different radii for a BB with tapered input at 45^o with respect to the BB axis-normal. Incident electrons now experience reduced potential gradients at the onset as compared with the flat electrode. Figure 25(e-h) show simulated electron trajectories with different tapered geometries (0^o, 30^o, 45^o and 60^o). Increasing the taper angle with respect to axis-normal increases the focal distance from the object plane, as expected.

This effect has been utilised to modify the BB input electrode's flat geometry to a tapered one. The BB in this study has been designed to operate at shorter working distances (17~24 mm). The voltages applied to the BB can range from few 10 eV for SE detection to 2 keV or more for AES detection. When operated at higher voltages and shorter working distances, results in field penetration from the input aperture to the region above the sample. The field penetration is maximum when a flat input electrode is used.

The reduction in field gradients inside the BB caused by a tapered input electrode also minimises the field penetration in the region above sample. In general, higher the taper angle for a given AR, lower the potential gradients at the input and lower the field penetration at the sample. A 45^o tapered input electrode offers a reasonable trade-off between the field penetration and BB's effective analysing length. Figure 26 shows simulated 3D electrostatic potential energy wells (with respect to 0 eV plane) for various BB energies of 10 eV, 100 eV, 1 keV and 2 keV. The set of figures on the left and right correspond to input electrode's flat and tapered input geometry (45^o), respectively. As can be inferred, field penetration upto 2 mm is evident even for the BB biased at 100 eV. Such field penetration is not observed for the tapered electrode geometry even for 1 keV bias.

.

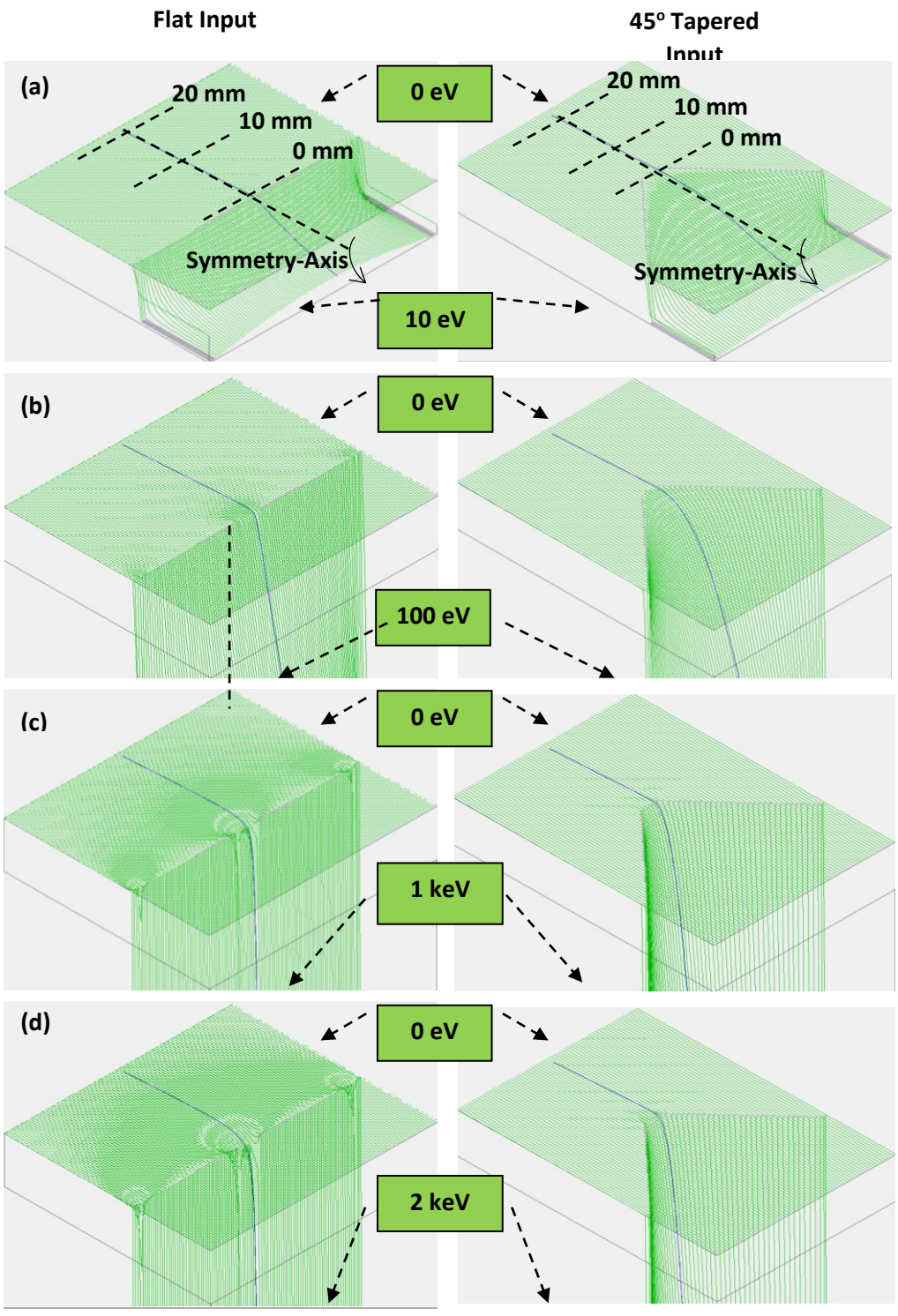

Figure 26 3D representation of the electrostatic potential energy wells with respect to 0 eV plane, as experienced by a 10.1 eV electron The symmetry axis (optic axis) and the length scales from the BB are shown in (a). The set of figures on the left and right correspond to flat and tapered input electrode geometries respectively. The BB is

.

operated at (a) 10 eV, (b) 100 eV, (c) 1 keV and (d) 2 keV. All the figures are to scale, shown in (a) and (b).

4.2.3. BB Analyser Dimensions

In the course of this project, two BB geometries were designed, fabricated and tested. The first geometry, which was designed for the experiments to be carried out at University of York forms the basis of this report. Another, compact version was designed as a part of the collaboration with Eth Zurich, is discussed in the last section. The simulated and experimental results discussed in this work pertains to the BB designed for SEM at University of York, when otherwise specified.

The BB geometry discussed in this work used 1.75 AR as in Schwietz's design (57) with specific modifications included:

1. The BB length of 70 mm and diameter of 50 mm corresponding to a reduction in dimensions by a factor of more than 2. A more compact version with a scaling factor of 10 is discussed in the later section. The scaling offers a comparison between the current compact design and the previous design.
2. Modification to the flat input electrode to a tapered one (45^{o}), as shown in Figure 27a, for avoiding field penetration to the sample, especially when the gridless design is considered.

As mentioned, the BB comprises of three electrodes in the form of a central cylindrical (Figure 27a) electrode and two end-cap electrodes. Controlling the voltages on these electrodes enables the BB to analyse electrons as demonstrated in Figure 27b. Annular input (4 mm inner and 2 mm outer diameter respectively) and output hole (2 mm) apertures are defined on the end-cap electrodes. The separation between the input and cylinder electrode is 0.5 mm, while the output and cylinder electrode are shorted. Electron energies less than the pass energy are repelled back (Figure 27c); electron energies higher than the pass energy are terminated at the BB electrode walls (Figure 27d); and electron energies within a narrow band can be transmitted through the BB for collection (Figure 27b).

.

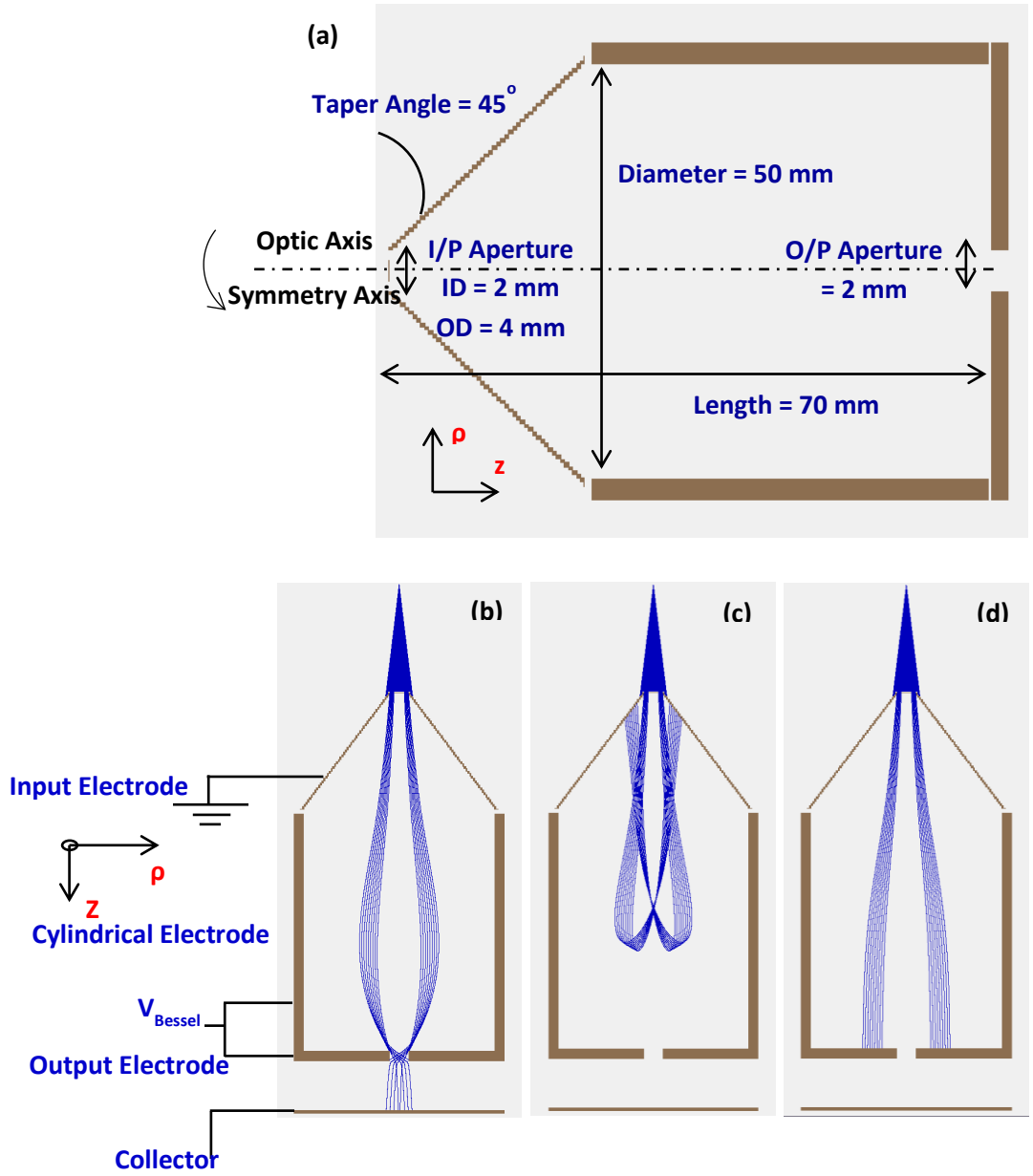

Figure 27 (a) shows BB analyser geometry. A cross-section view of the electron trajectories in the BB. (b) For a given set of voltages the BB focuses electrons at the output aperture before they are collected. (c) Lower energy electrons have insufficient energy to reach the collector. (d) The BB is not able to focus higher energy electrons.

4.3. Analyser Design Principle

An incident beam can be made to deflect under the influence of an electrostatic field resulting in the dispersion of the incident electrons into their respective energy components. A narrow band of energies can then be collected by defining an output

.

aperture. Consider the BB described in the previous section. For simulations, a point electron source is located at the origin. The BB was evaluated at a fixed analyser working distance of $Z_o = 20$ mm, between the source and the apex of the tapered input electrode as shown in Figure 28.

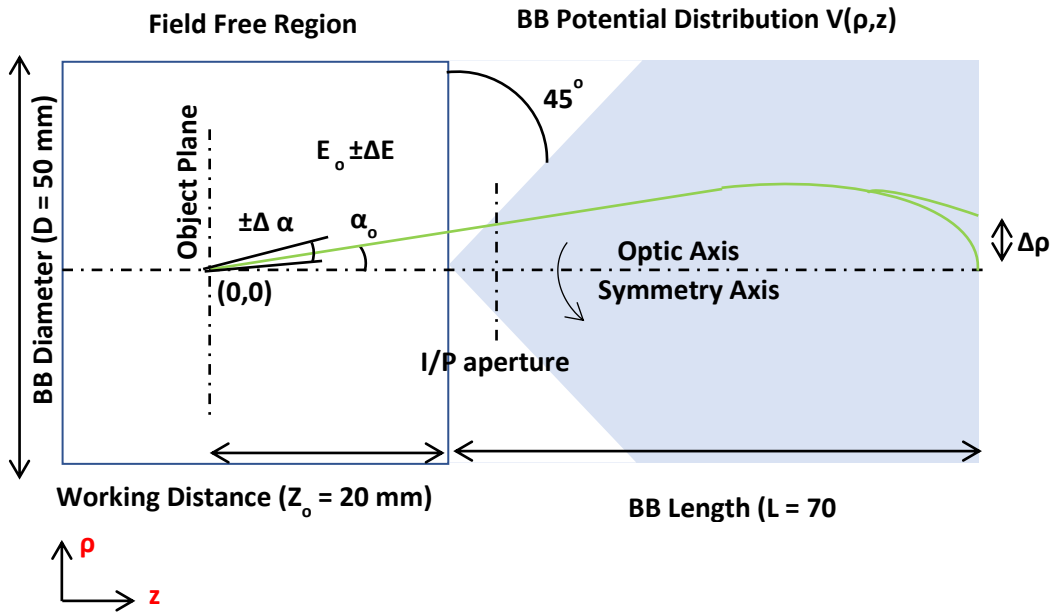

Figure 28 BB design principle.

An electron with a take-off angle α_o leaves the sample surface in a field free region between the grounded sample and the BB input. Depending on its incident energy and angle it makes with the BB field gradient, an electron is retarded back towards the optic axis with a total travel distance of Z from the point of origin. The equations of motion in radial and axial directions for electrons inside the BB can then be given by:

$$m_e \frac{\partial^2 \rho}{\partial t^2} = -eE_\rho(\rho, z) \qquad 4.\ 10$$

$$m_e \frac{\partial^2 z}{\partial t^2} = -eE_z(\rho, z) \qquad 4.\ 11$$

.

where m_e and e are the mass and the charge of the electron, respectively $E_\rho(\rho, z)$ and $E_z(\rho, z)$ are the radial and axial electrostatic fields respectively. For an electron beam with central pass energy of E_o and small spread of $\pm\Delta E$, would terminate at the output electrode at different ρ-coordinates, as shown in the Figure 28. The width traced ($\Delta\rho$) by these electron trajectories on the output electrode is given by relative dispersion:

$$\frac{D}{E_o} = \frac{\Delta\rho}{\Delta E}$$

4. 12

The BB's acceptance cone, defined by the input aperture, intercepts only a tiny fraction of the total cosine distribution of the emanated electrons resulting from the beam-matter interaction. This allowed angular spread ($\pm\Delta\alpha$) or the acceptance-angle results in an increase of the trace-width ($\Delta\rho$). A condition is imposed on the take-off angle (with respect to optic axis) (α_o) to minimise this effect:

$$\frac{\partial\rho}{\partial\alpha} = 0$$

4. 13

When this condition is satisfied, the BB is operated in a first order focussing regime, wherein, the trace width now depends on higher order variations in the angular spread ($(\Delta\alpha)^2, (\Delta\alpha)^3$ and so on).

A linear relationship between the radial coordinate and relative energy spread is shown in Figure 29a. Figure 29b shows first order conditions for the different energies above BB energy. For 10.12 eV, 10.13 eV, 10.14 eV, 10.15 eV, 10.16 eV and 10.17 eV, the first order condition is numerically found to be 1.6^o, 2.1 ^{o}, 2.5 ^{o}, 2.8 ^{o}, 3.2 ^{o} and 3.4 ^{o} respectively.

.

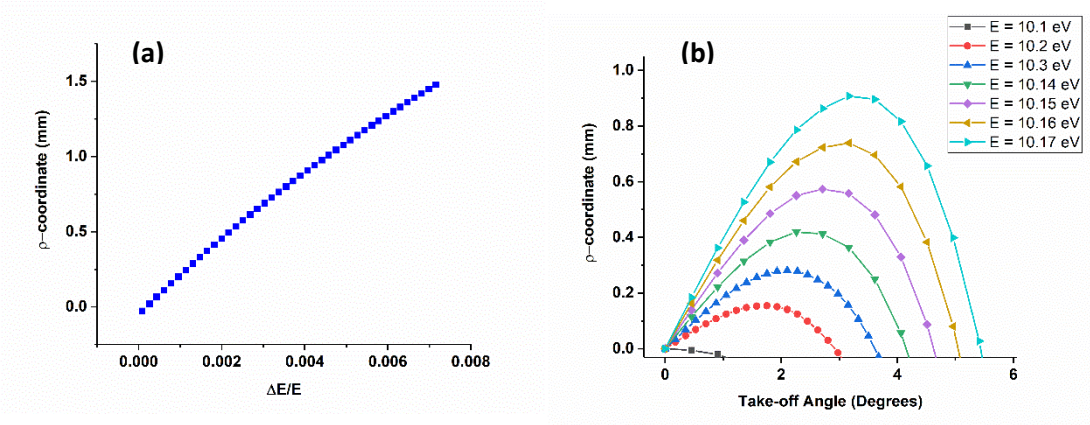

Figure 29 (a) The electron energies terminated at the output aperture as a function of BB radial coordinate for a BB bias of -10 V. (b) demonstrates first order condition for electron trajectories with varying electron energies.

4.4. Aperture Design

One of the most important performance parameters is the relative energy resolution ($\Delta E/E$) of the analyser. It depends on the dimensions of input and output aperture. As previously described, on-axis electrons need to be prevented from detection. This calls for an annular input aperture design (Figure 30a). The resolution, therefore, would depend on the input aperture's inner dimension (ID) and outer dimension (OD) coupled with output aperture diameter. Other performance parameters are discussed in chapter 5 which include: depth of focus ($\pm\Delta z$) and field of view ($\pm\Delta\rho$). An algorithm for the code written in SIMION, by the author takes a general approach for assessing BB's performance parameters. As will be demonstrated in the subsequent sections, this approach provides an ease to study and design customised apertures for energy resolution and collection efficiency.

In the simulation setup, multiple electrons with a set of initial take-off angle and energy are directly fired at the BB input, in an iterative fashion. A single electron trajectory corresponding to intial energy and angle is counted if it terminates at the specified radial coordinates on the output electrode. Subsequently the process is iterated over entire energy-spread and over all take-off angles. Mathematically, the incident matrix $I_{\alpha,E}$ is represented as a 'matrix of ones':

.

$$I(\alpha_i, E_i)_{\alpha_n, E_n} = \begin{bmatrix} b_{1,1} & \cdots & b_{1,E} \\ \vdots & \cdots & \vdots \\ b_{\alpha,1} & \cdots & b_{\alpha,E} \end{bmatrix} = 1$$

4. 14

where α_n and E_n correspond to the size of the matrix depending on the angular and energy spread and the number of steps. All simulations were carried out at a fixed energy step of 0.001 eV and angular step of 0.01°. A MATLAB code was written for the analysis of the transmitted matrix T_{α_n, E_n}:

$$T(\alpha_i, E_i)_{\alpha_n, E_n} = \begin{bmatrix} N_{1,1} & \cdots & N_{1,E} \\ \vdots & \cdots & \vdots \\ N_{\alpha,1} & \cdots & N_{\alpha,E} \end{bmatrix}$$

4. 15

where $N_{\alpha,E}$ = 0 or 1.

4.4.1 Input Aperture

For input aperture design, the BB input electrode is simulated as an ideal grid, preserving the potential distribution but allowing higher angled trajectories into the BB. Once again, only the dispersed electron trajectories that terminate at the radial coordinate of the output electrode are counted in the simulations. The detected count $N(E_i, \alpha_i)$ is a function of the electrons' initial energies and angles and is summarised in Figure 30b. This is the analyser's transmitted matrix for an output aperture of radius = 1mm. Henceforth, referred to as 'acceptance plot', relates the transmitted response of the BB (V_{BB}: -10 V) to the initial conditions of the angles and energies of the electrons. The violet background corresponds to 0 electron detection and the yellow corresponds to detected electron count of 1. The broad curvature in the shape of the area of detected electrons with angle reflects the greater dispersion from the higher radial field gradients experienced by high-angled trajectories than for the low-angled electron trajectories.

.

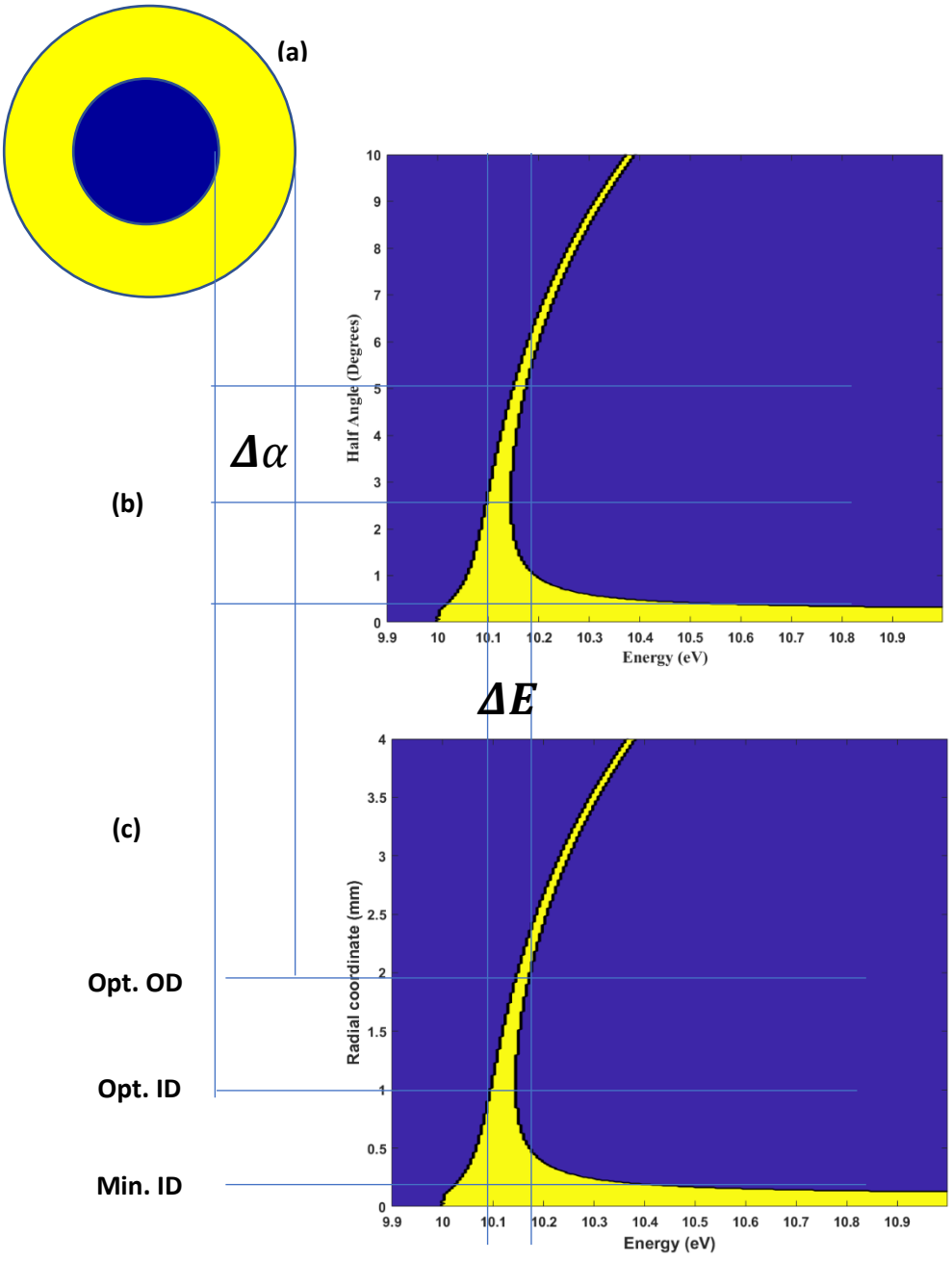

Figure 30 Region of detected electrons as a 2D function of the initial angle and energy of the electron for a BB voltage of: -10 V. Yellow represents detected count = 1 and violet background no detection.

The detection of energies for angles shallower than 0.5^{o} correspond to on-axis trajectories. These electrons have line-of-sight to the detector and are minimally deviated by the low-field gradients near the optic axis. With this as starting point

.

subsets of the acceptance plot were extracted for the definition of various combinations of ID and OD radii.

These subsets were integrated over all angles between α_{ID} and α_{OD} for each incident electron energy, resulting in an energy spectrum:

$$N(E) = \sum_{\alpha_{ID}}^{\alpha_{OD}} N(E, \alpha)$$

4. 16

The total count detected in the spectrum equals to the area under the simulated spectrum. Peak-pass count at the pass energy is simply defined as the maximum count in the simulated spectrum:

$$N(E_o) = max\left(\sum_{\alpha_{ID}}^{\alpha_{OD}} N(E, \alpha)\right)$$

4. 17

The transmission efficiency is given as the ratio of the maximum count in the spectrum corresponding to the pass energy or E_o, to the total incident counts (I matrix) within the solid angle at that energy:

$$T = \frac{N(E_o)}{\sum_{\alpha_{ID}}^{\alpha_{OD}} I(E_o, \alpha)} \text{x}100$$

A Gaussian curve is fitted onto the simulated data to estimate the full width at half maximum (FWHM):

$$N(E) = \frac{1}{\sqrt{2\mu\sigma^2}} e^{-\left(\frac{E-\mu}{\sqrt{2\sigma}}\right)^2}$$

4. 18

where μ is the mean value of the counts and σ is the standard deviation and is related to FWHM by:

.

$$FWHM = \sqrt{2\sigma}$$

4. 19

Relative energy resolution, is given by:

$$Relative\ Energy\ Resolution = \frac{FWHM}{E_{peak-pass}} \text{x}100$$

4. 20

Finally, in order to determine the ID and OD of the input aperture, the Y-axis (angle) is reinterpreted to the BB radial coordinate on the axis-normal plane located at the apex of tapered input electrode, as shown in Figure 30c. The minimum ID radius needed to stop the on-axis trajectories is 0.25 mm.

Figure 31a-b shows resolution and transmission efficiency as a function of OD radius for a fixed output diameter of 2 mm. Multiple plots correspond to ID radius of 0.25 mm, 0.5 mm, 0.75 mm, 1 mm, 1.5 mm, 2 mm and 2.5 mm. Figure 31c shows transmission function weighted with the respective solid angle. A 100% transmission through the analyser can be seen for OD radius of 2 mm for various ID radii up to 1.5 mm.

There is always a trade-off between the energy resolution desired and the number of electrons collected, as can also be inferred from Figure 31a and c. The input aperture dimensions were chosen to achieve acceptable energy resolution and collection efficiency. The dimension chosen for the experimental characterisation are; OD radius = 2 mm, ID radius = 1 mm (green curve in Figure 31). This offers a resolution of 0.4% and collection efficiency of 0.28%. One can choose, an OD radius of 3 mm and an ID radius of 0.5 mm (red curve) for a higher collection of 0.8 % at 1% energy resolution. The working distance from the input aperture now equals $Z_o = 20+2 = 22$ mm.

.

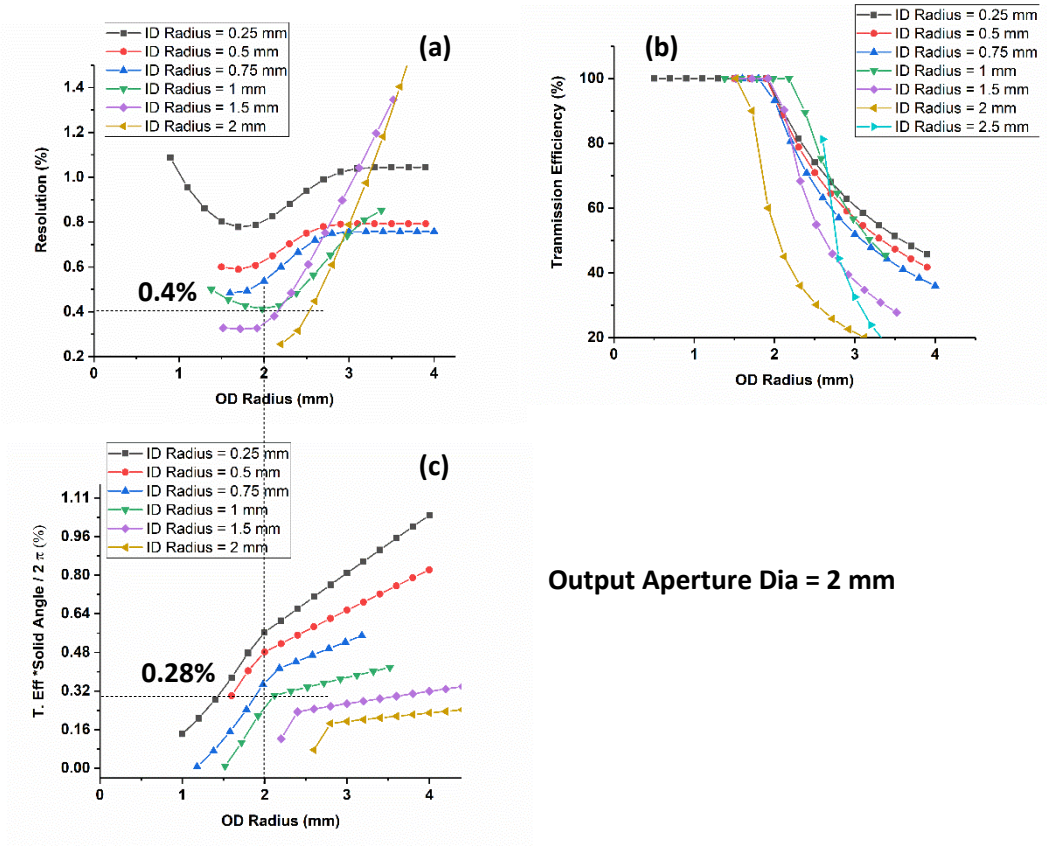

Figure 31 (a) Resolution and (b) transmission efficiency as function of OD radius of input aperture for an output. Multiple plot corresponds different ID radius. (c) Transmission efficiency weighted with the solid angle.

A new acceptance plot corresponding to aperture dimensions is shown in Figure 32(I) and the simulated spectrum is shown in Figure 32(II). The colours introduced in the detected peak correspond to larger contributions (yellow) to the total count from radii near OD as compared to lower counts near to ID (blue-green). The pass energy (for the BB biased at -10 V) is shown to be:

$$E_{peak-pass} = 10.14\ eV$$

4. 21

A ratio of the BB energy to the peak-pass energy gives a constant of the analyser, defined as:

.

$$K_{BB}(Simulated) = \frac{E_{peak-pass}}{E_{BB}} = 1.014$$

4. 22

The analyser's constant depends on the input and output aperture dimensions for a fixed working distance.

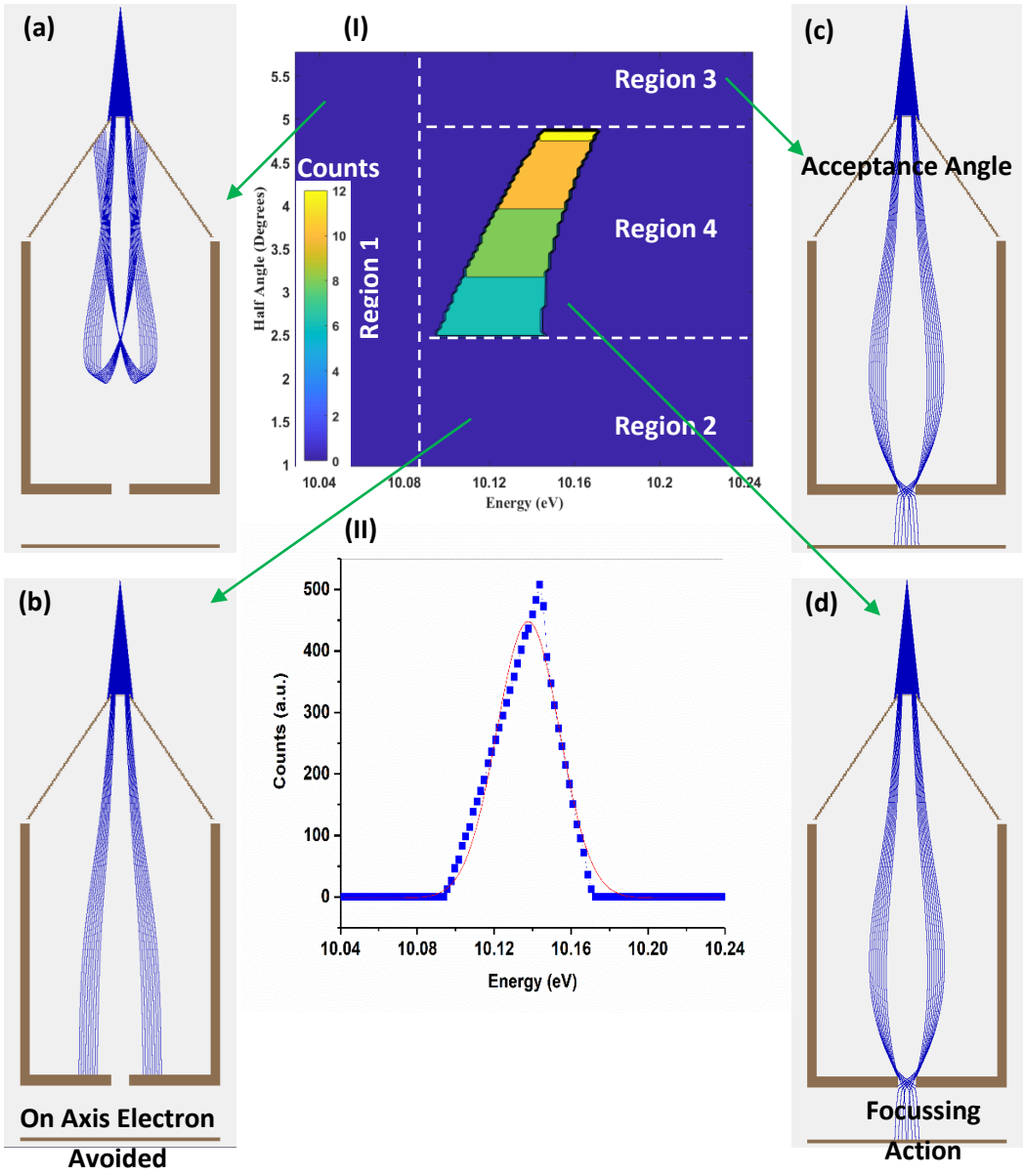

Figure 32 (I) shows acceptance plot for the BB biased at -10 V and operated at 23 mm working distance (centre) with simulated electron trajectories: (a) Regime 1

.

corresponds to electrons lower than the BB energy and are repelled back. (b) Region 2: On axis electrons are not deflected by the BB fields and are avoided by the central stopper. (c) Region 3: electrons physically stopped by the input aperture, and (d) Region 4 showing the focussing action of the BB. (II) Spectrum of incident electron energies obtained by integrating the surface plot over all incident angles at each incident electron energy with an analyser voltage at -10 V.

Notice the simulated spectrum is a skewed one. This is because of the asymmetric contribution from the angles within the acceptance cone. The BB acceptance plot can be divided into 4 regions for relating it with working of the BB:

Region 1: All the incident electron energies are less than the BB energy and therefore repelled back (Figure 32a).

Region 2: Correspond to the on-axis trajectories that are stopped by annular input aperture's ID (Figure 32b).

Region 3: This region falls outside the analyser's acceptance cone and therefore the electron trajectories are physically stopped from entering the BB (Figure 32c).

Region 4**:** This region demonstrates the focusing action of the analyser (Figure 32d).

4.4.2 Output Aperture

Figure 33(a-b) shows the resolution and total detected counts as function of output aperture diameter for input aperture of ID radius = 1mm and OD radius = 2 mm. A 100% transmission was calculated for all the output apertures. An increase in total counts is expected with an increase in the output aperture diameter. An increase in resolution increased can be seen for aperture diameters greater than 2 mm. An examination of the simulated spectra (Figure 33c), shows a shift in the central energy for the output aperture diameter of 0.5 mm. This is a result of the asymmetric trace-width by the angles in the acceptance cone. A summary of simulated resolution and transmission function for various combinations of the input ID and OD radius with output aperture diameter is shown in appendix A.

.

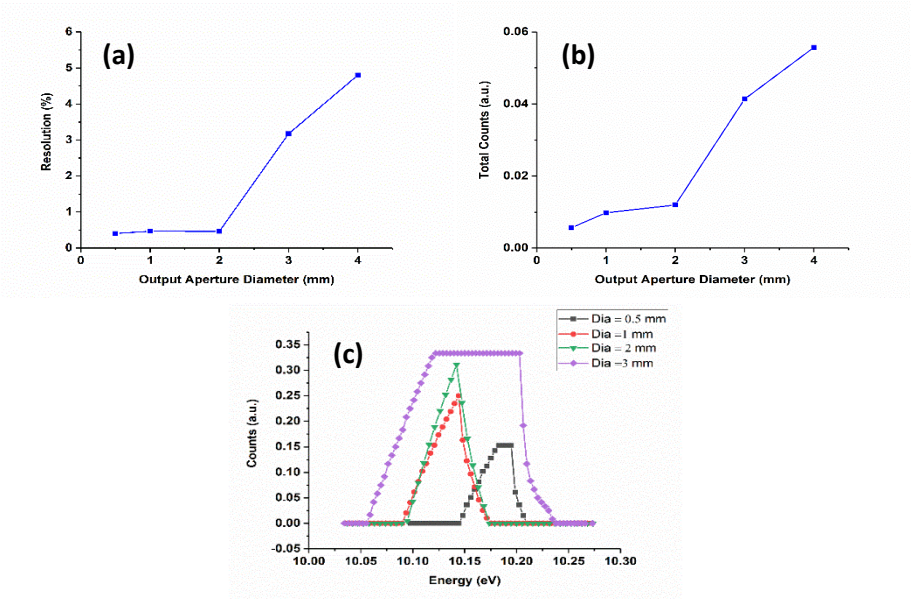

Figure 33 shows the (a) resolution and total counts (b) as a function of output aperture diameter, with input aperture of ID radius = 1mm and OD radius of 2 mm. (c) shows simulated spectrum for output aperture diameters of 0.5 mm, 1 mm, 2 mm, and 3 mm.

4.5. BB Optics

All the numerical solutions until now have been calculated for a fixed working distance. To further understand the focusing properties of the BB, the solid angle subtended by the input aperture at the source is swept and the acceptance-plot is generated for each working distance (Z). A similar procedure as described earlier is carried out to extract the BB performance parameters. This helps in numerically computing and optimizing the working distance for the best focusing action of the analyser. More specifically, at optimized working distance ($Z_{WD} = 22\,mm$), the angular contribution causes minimum energy-spread around the peak-pass energy with 100% transmission through the analyser. Furthermore, it leads to a shift in the central detected energy and the highest detected peak-pass count rate. These observations are summarized in Figure 34a-d. As for the shorter working distance, (i.e. $Z < Z_{WD}$) the electrons can enter the BB only at higher angles (shallower-angled trajectories are blocked by the input ID). The stronger radial-field near the BB electrode under-focusses the electron trajectories leading to a broader energy spread.

.

Only a fraction of incident trajectories within the analyser's solid angle are detected, resulting in lower transmission through the analyser and lower peak-pass count rate.

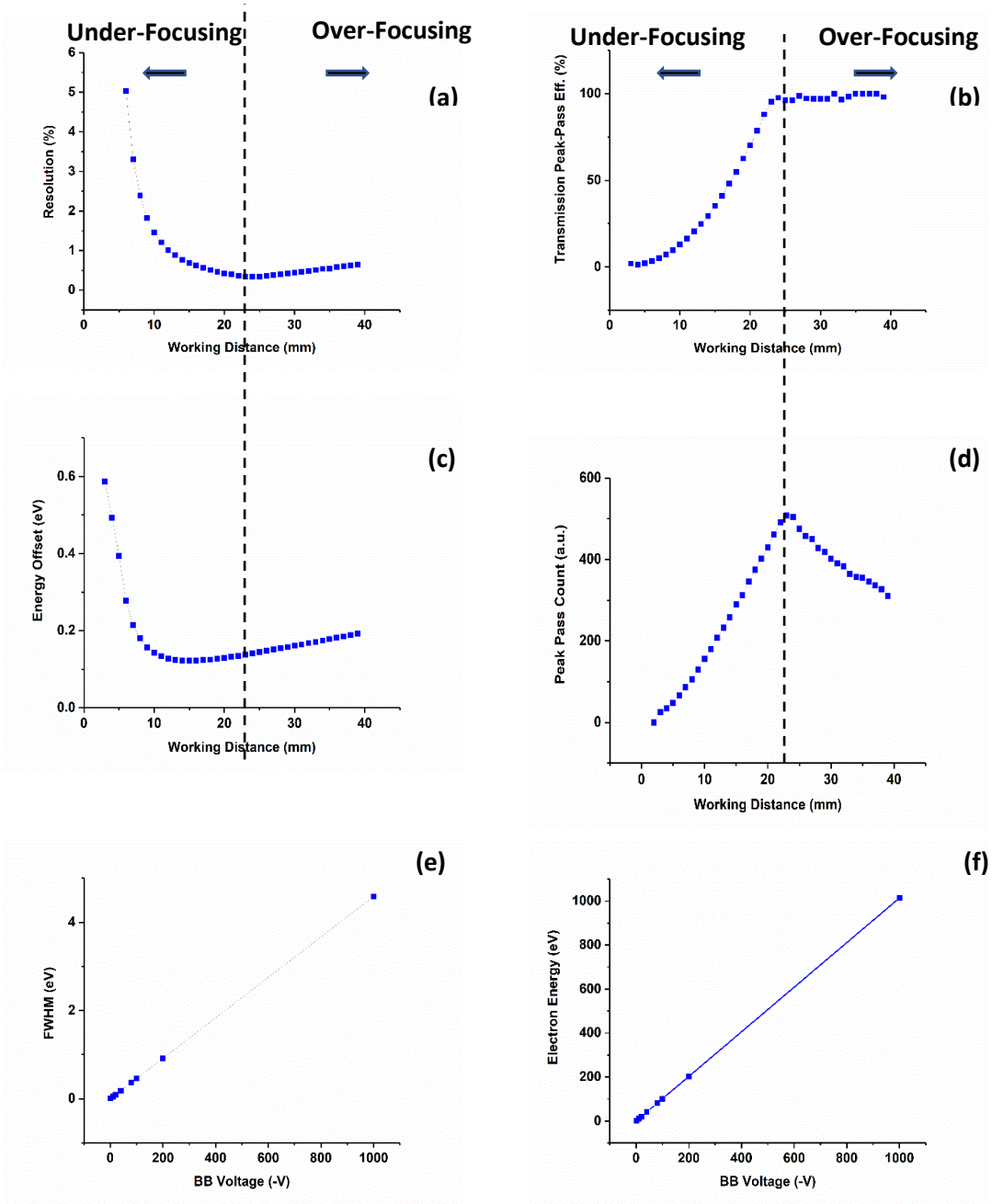

Figure 34 The focussing action and the performance parameters of the analyser: (a) resolution, (b) peak-pass transmission efficiency, (c) energy offset and (d) peak-pass count as a function of working distance. A linear relationship of FWHM (e) and central electron energy (f) is numerically established as a function BB energy.

.

On the other hand, longer working distance (i.e. $Z > Z_{WD}$), the electron trajectories enter at shallower angles and experience weaker radial fields close to the axis. The BB now operates in over-focusing regime. Given the finite size of the output aperture, the over-focusing allows more electron trajectories around peak-pass energy with 100% transmission leading to increase in the energy spread and energy offset in the detected spectrum. The overall peak-pass count rate decreases because of the decrease in the solid acceptance-angle with increasing working distance.

Simulations were also carried out at higher electron energies. A linear relationship between the FWHM and pass energy is established numerically (Figure 34e). A similar linear-relationship is also calculated for the pass energy with respect to the BB energy as shown in Figure 34f, the slope of which equals = K_{BB} (from equation 4. 22)

For a practical detector design, the BB mounted on a linear drive can be operated in two modes simply by changing the output aperture and working distance as shown in Figure 35. For AES detection which requires higher resolution, an output diameter of 2 mm can be used which offers an energy resolution of 0.4% and a collection efficiency of 0.28% at operating working distance of 22 mm, as previously described. For SE imaging mode which requires higher collection, an output aperture of diameter 4 mm can be used, which offers 0.8% collection efficiency (Figure 35b) with an inferior resolution (Figure 35a) of 0.7% at a working distance of 17 mm. For the time being, the experimental work (spectroscopy and imaging) described in this thesis is carried out using an output aperture of diameter 2 mm.

.

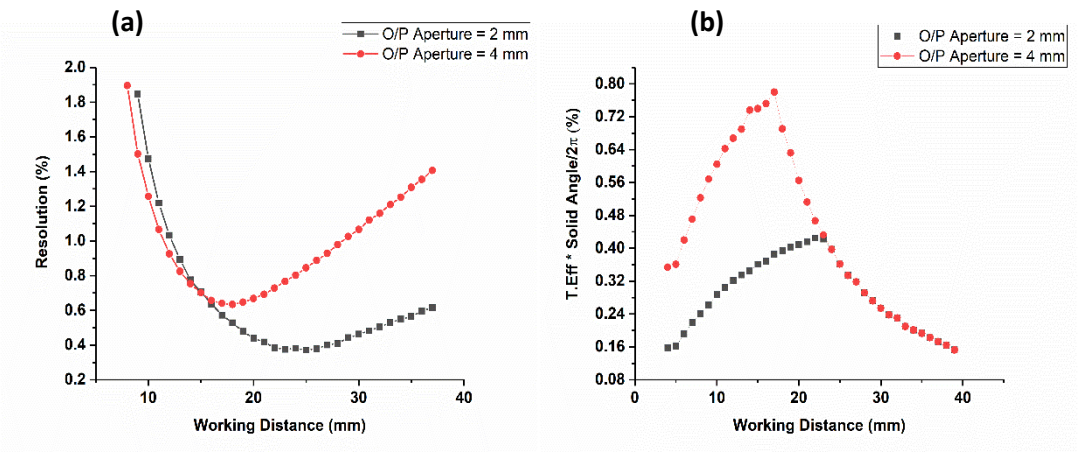

Figure 35 Comparison of resolution (a) and collection efficiency (b) for output aperture diameter of 2 mm and 4 mm respectively.

4.6. BB Scaling

A new BB was designed as a part of collaboration of University of York with ETH Zurich for the energy analysis of low energy electrons in their novel instrument: scanning field emission microscope (SFEM) (63). The SFEM is based on a scanning tunneling microscope (STM) with a retracted tip such that electrons no longer tunnel between tip and surface but are instead field emitted from the tip to the surface. In this mode, secondary electrons are generated from the surface that can be used for characterization. Although the SFEM is a compact instrument as it is a lens-less SEM design (typical tip-sample distance is 50 nm), the analysis of the emitted electron energy distribution has to-date been carried out using a bulky hemispherical energy analyser. A scaled down version of BB analyser was proposed for this application.

In general, if all the BB geometric parameters are scaled down by the same factor ‘S’: length, AR then the resolution and transmission functions discussed so far shall be described with respect to scaled down dimensions of input ID radius/S and OD radius/S, output aperture radius/S at a given working distance/S. The present design requirements in SFEM included an upgrade in energy resolution from the current-in-use energy analyser (relative energy resolution of 1%). Considering geometrical constraints around the STM tip, piezoelectric motor assembly and the sample stage

.

(computer aided design or CAD drawing of Figure 36a), a restriction was imposed on the BB diameter to 10 mm and on the minimum working distance of 5 mm.

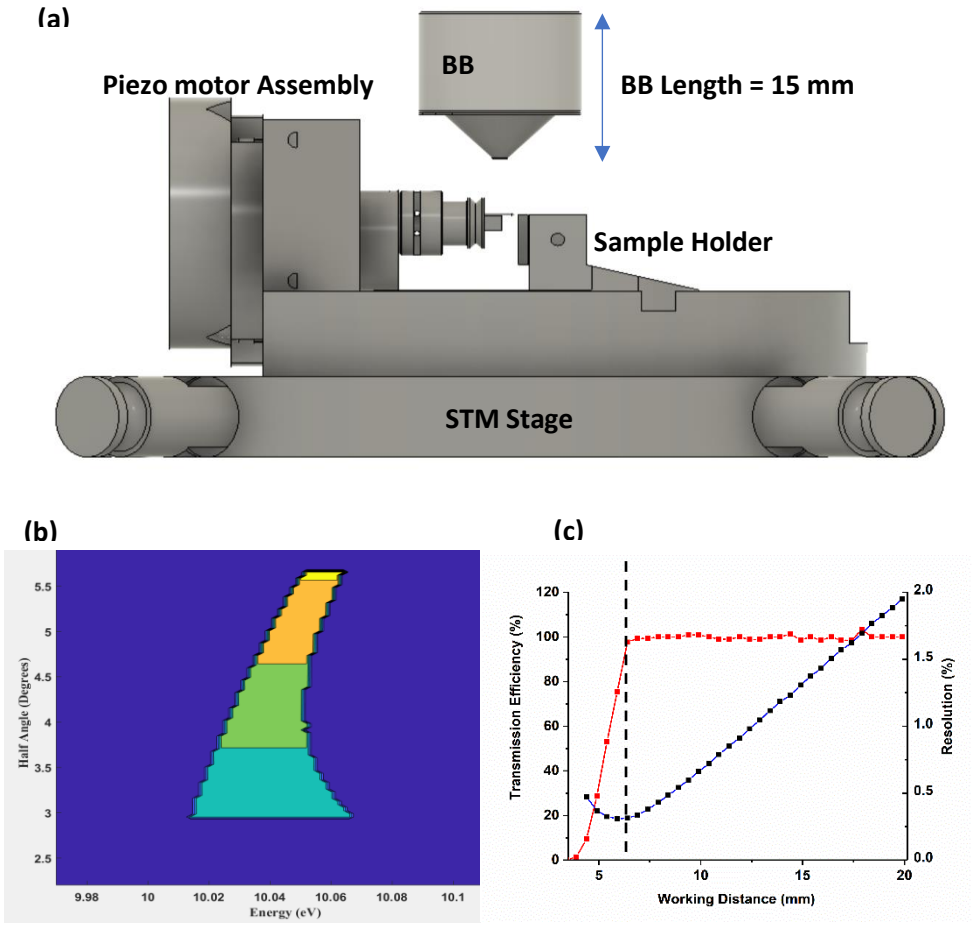

Figure 36 (a) shows CAD drawing of a dummy STM stage provided by ETH Zurich (side view). It is integrated with the BB analyser CAD drawing, dimensions to scale. (b) shows acceptance plot of the smaller BB design (c) resolution (black) and transmission efficiency (red) as a function of working distance.

With this as the starting point the BB was designed for the total length of 15 mm with tapered input electrode and working distance of 6 mm from the sample. Input ID and OD radii and output aperture diameter were chosen for a resolution of 0.3%. Table 3 summarises geometric parameters, energy resolution for both the designs. Figure 36b shows the acceptance plot of the new design. A transmission efficiency (red curve) and resolution (black curve) as a function of the working distance (Figure 36c) is numerically calculated with the procedure described in previous sections.

.

Geometric Parameters	BB Design for SEM (UoY)	BB Design for SFEM (ETH Zurich)
Total BB Length	70 mm	15 mm
BB Diameter	40 mm	10 mm
Input ID radius	1 mm	0.25 mm
Input OD radius	2 mm	0.5 mm
Output diameter	2 mm	0.5 mm
Working Distance (from I/P aperture)	22 mm	6.5 mm
Energy Resolution	0.4%	0.3%
Transmission Efficiency	100%	100%
Collection Efficiency (over 2π sr)	0.28%	0.28%

Table 3 shows the comparison between a larger and smaller BB parameter designed in this work.

4.7. Summary

This chapter discussed the theory and operation of a compact BB analyser designed for SEM and a scaled down version for SFEM. A code written in SIMION ray tracing software enabled the systematic study and design of the apertures needed to achieve desired trade-off between energy resolution and collection efficiency. An energy resolution of 0.4% was numerically calculated which approaches the performance of the CMA for AES detection. The energy resolution and transmission functions with respect to working distance were generated which will be helpful in the experimental characterisation of the BB detector, discussed in the next chapter.

.

Chapter 5: The Bessel Box: Experimental Characterisation

The BB analyser for SEM described in the previous chapter was fabricated in-house, in the Department of Physics' mechanical workshop. The complete detector setup consists of a designed component: the BB analyser and an electron collector: channeltron electron multiplier (CEM). This chapter discusses experimental characterisation of the BB analyser in a UHV test-chamber using a LEED gun.

The chapter begins with explanation of different components constituting the BB detector assembly and experimental setup for the BB characterisation. Subsequently, the experimental findings are discussed which helps in the assessment of the analyser's performance via parameters such as relative energy resolution, depth of focus and field of view. The experimental results are also compared with the numerical results presented in the previous chapter. Experimental spectrum was acquired from silicon (111) sample with this BB detector. The chapter concludes with the discussions on the preliminary experimental results from the BB analyser designed for SFEM, carried out at ETH Zurich in a UHV test-setup in section 4.

5.1. Experimental Setup

Figure 37a shows an exploded, isotropic view of the BB analyser assembly in a CAD (computer aided design) drawing. The BB electrodes are shown in green, poly ether ketone (PEEK) spacers are shown in golden and grounded shielding electrodes and mounts are shown in black, respectively. From left to right, conical input electrode; was connected to the BB cylindrical electrode using M3 PEEK screws (not shown) and isolated using a PEEK spacer. The output electrode was connected to the cylindrical electrode using M3 steel screws (shorted together in-situ). This was followed by a channeltron electron multiplier (CEM). The CEM and the shielding-cylinder (lower half of the Figure 37a.), are secured to the circular assembly-mount with a mounting rod. Finally, the cylindrical electrode was fastened on the inside of

.

the shielding cylinder using a PEEK M4 screw and is separated by a semi-circular PEEK spacer. This forms a complete BB detector assembly.

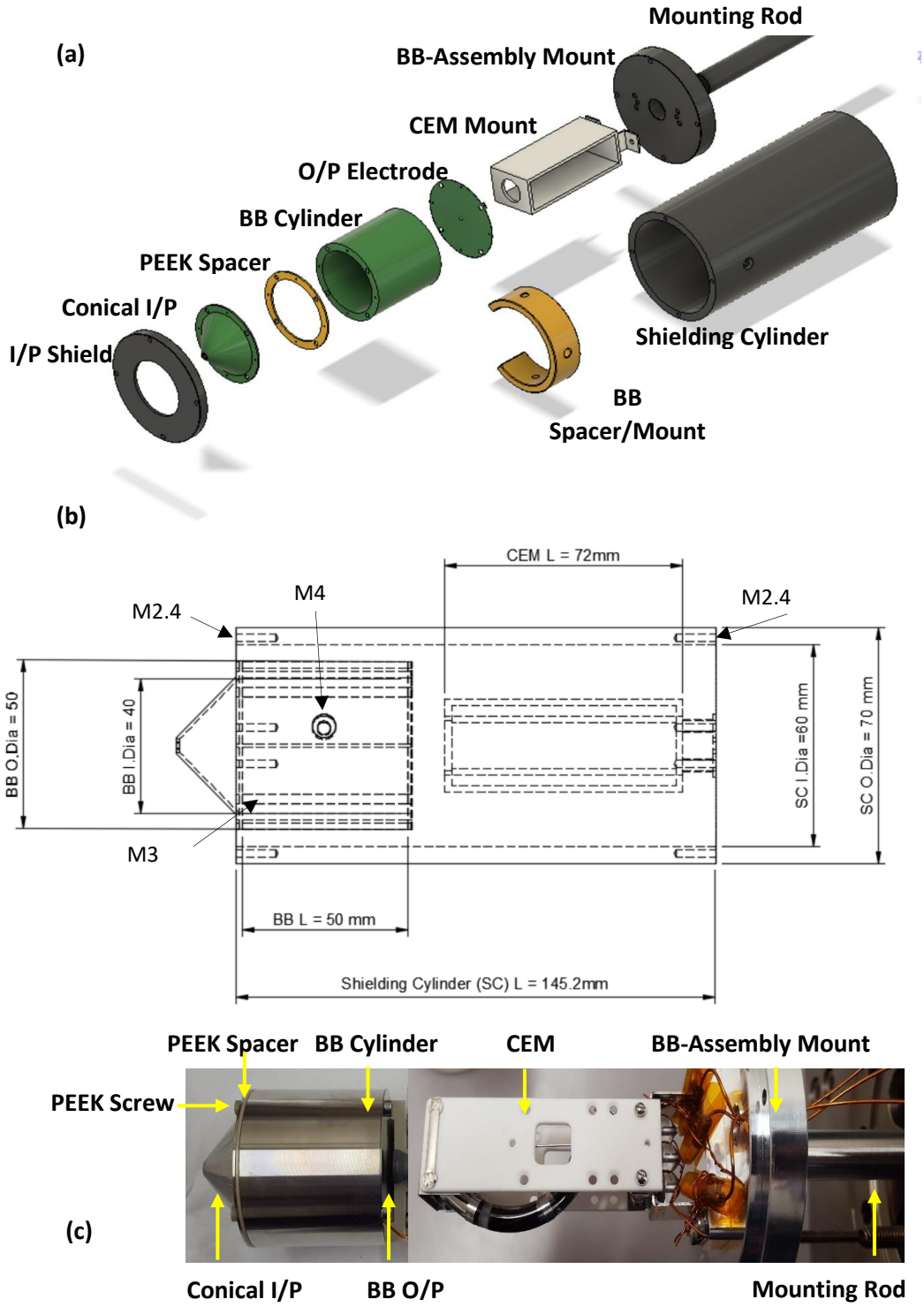

Figure 37 Components of BB analyser assembly (a) in a CAD drawing with 3D isotropic view and (b) 2D side view and (c) photograph of the BB assembly.

.

As it will be discussed, the BB was mounted on a 8″ port of a large UHV chamber, therefore the outer dimensions of the BB and shielding cylinder were not of critical importance. However, care was taken to restrict the outer diameter of the BB shielding cylinder from interfering with the LEED gun's scintillator screen. The BB cylindrical electrode was fabricated with inner and outer diameter of 40 and 50 mm, respectively. The inner and outer diameter of the shielding cylinder was 60 mm and 70 mm respectively (Figure 37b). Annular input (4 mm inner and 2 mm outer diameter respectively) and output hole (2 mm) apertures are defined on the end-cap electrodes. The separation between the input and cylinder electrode is 0.5 mm, while the output and cylinder electrode are shorted in-situ. The separation between the output electrode and CEM is 2 mm. The upper limit of the total assembly length was determined by the length of the CEM, which in this case was more than 70 mm long. Figure 37c shows a photograph of the fabricated parts of the BB detector assembly (shielding cylinder not shown). It also shows the PEEK screws which were used to connect the conical input and the cylindrical electrode. In order to prevent line of site of the electrons the assembly components, an input shielding ring was screwed into the shielded cylinder using M2.4 screws (Figure 37a). The author acknowledges the contribution of Mr. Jason Flatt from mechanical workshop for providing with individual CAD drawings of the BB/CEM mounts along with shielding electrodes which are used in the CAD drawings of the BB assembly in Figure 37a-b.

A complete circuit block-diagram of the BB-sample system is shown in Figure 38. The electrons from a grounded or a biased sample surface are focussed by the BB onto a CEM. The connections from input and the BB electrode, along with CEM wires are connected to their respective power supplies using feedthroughs mounted on the BB manipulator. The description of each component of the experimental setup is discussed in the following sections.

5.1.1. Electron Multiplier

Electron multipliers are used in vacuum systems to amplify low-level (usually in fA to nA range) or a single free-electron signal through the multiplication of electrons by the phenomenon of secondary electron emission. CEMs (64) and multi-channel plates

.

(MCP (65)) are the most common commercially available electron multipliers. The incident electrons hit the inside-walls of a high resistance, semi-conductive, high electron-emissive material (such as glass or ceramic) and lead to secondary electron generation.

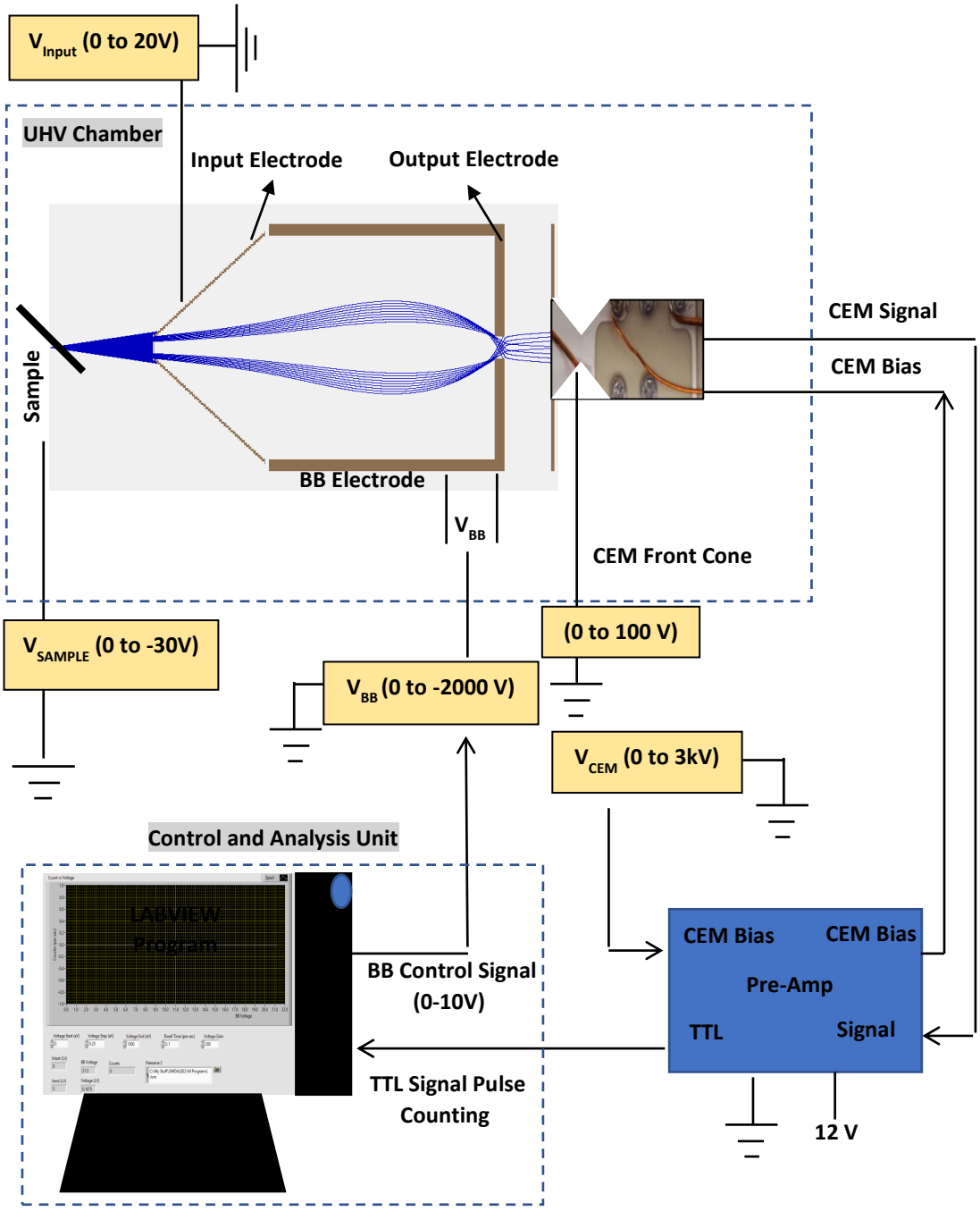

Figure 38 Circuit block-diagram for the BB experimental setup.

.

Upon applying a high bias of 2-3 kV across the CEM, electrons are accelerated through its length causing a cascade of such collisions. This results in amplification of the signal. Depending on the multiplier length, multiple such collisions take place and are responsible for the net gain. The choice of the electron multiplier usually depends on the desired gain. CEMs have higher gains of about 10^8 and MCPs can have gain of 10^3 to 10^6 (when used in parallel). Experimental work presented in this chapter makes use of a CEM from Photonis USA Inc. (Part no. - CEM 7010 C WLNM).

A resistance of 400 MΩ was measured between the front horn and the back of the CEM. Unlike a simple analog amplification, counting mode is employed which is a more sensitive way of electron detection, when there are low number of electrons per second. A single electron impact on the electron multiplier is amplified and converted to a transistor-transistor-logic (TTL) pulse using a pre-amplifier unit interfaced with the CEM. Noise in CEM is termed as 'dark noise' and is defined as the detected count rate when no input signal is given. A distinction is made between dark count rate and the actual count rate using a discriminator interfaced with pre-amp. It discriminates between high-level pulse heights of the true signal from the low-level pulse heights of the dark noise.

This study makes use of MTS-100 pre-amplifier by Advance Research Instruments Corporation. The discriminator value was adjusted by bringing the dark counts down to 0 while the electron gun was switched off. The gun was switched on to check for the detection of true counts. The process was repeated several times until the discriminator threshold was set just above the dark noise pulse-height. These CEM pulses are then converted to TTL pulses by the pre-amp. Counting these pulses in a given time frame called the dwell-time, corresponds to the number of electrons and contributes to the net signal intensity at a given BB energy.

5.1.2. Experimental Chamber

A rounded-cylindrical chamber with an average diameter of 26 cm and height of 30 cm was used in this study. As shown in Figure 39a, this UHV test chamber had three 8'' ports (outer diameter) which were used to mount diffusion pump, electron gun and BB manipulator with an adaptor flange (8'' to 6''), respectively. The relative location

.

of the ports can be seen in the top view in the CAD drawing (Figure 39b). The BB and the electron gun were mounted on the ports which were orthogonal to each other. The sample manipulator was introduced from the top and was mounted on an 4'' port. For the BB experiments, the sample was tilted at 45° with respect to the BB and the electron beam axis (Figure 39c-d). The BB and the sample were mounted on separate manipulators with 4 degrees of freedom: x, y, z and Φ. The chamber had four $2\frac{3}{4}''$ ports (not shown). One at the bottom used for mounting a rotary pump, the other with ion gauge mounted on it and the other two with glass windows mounted on them.

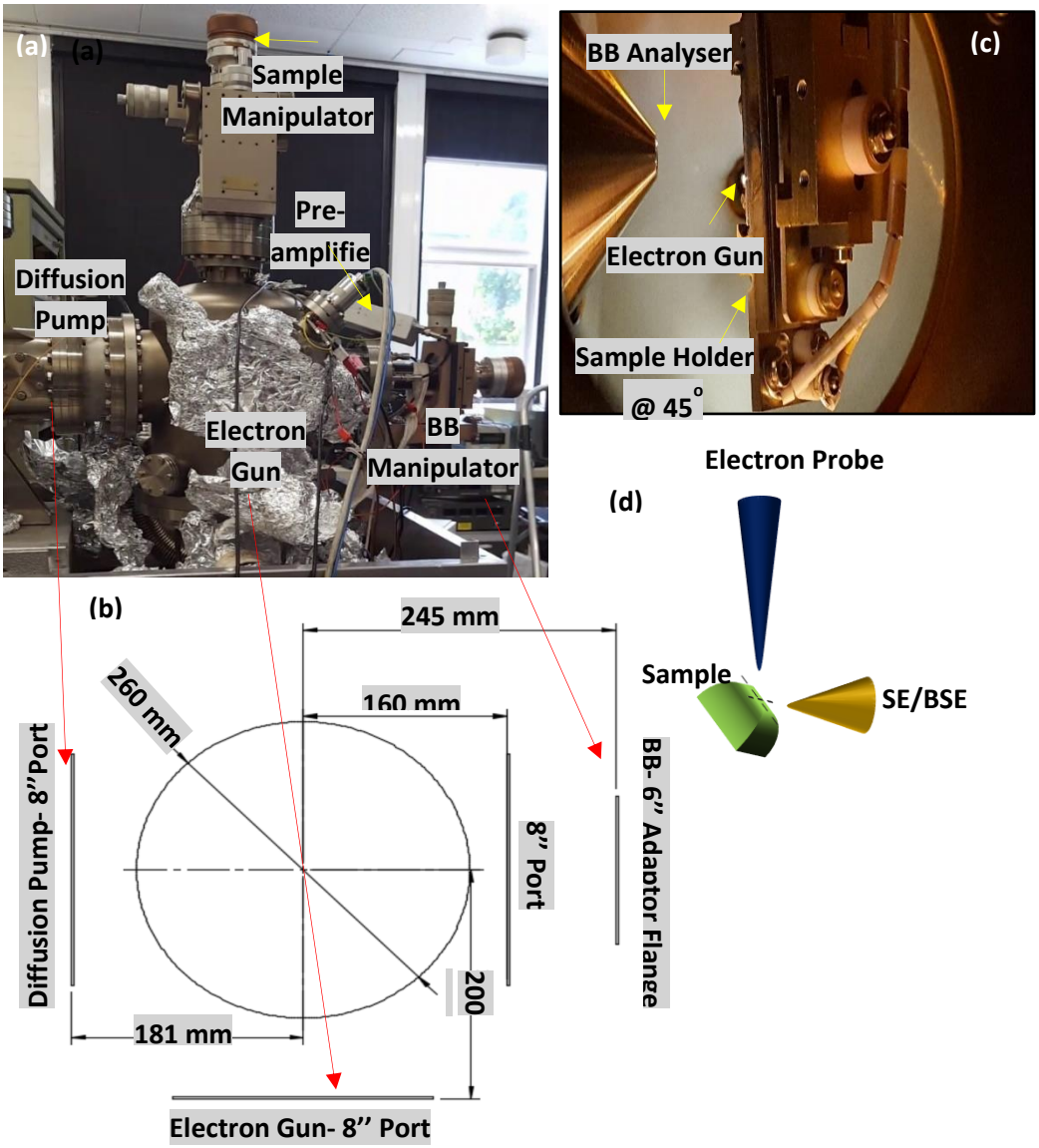

Figure 39 (a) UHV test-chamber used for the analyser characterisation experiments (b) CAD drawing of the top view of the chamber and the ports. The sample was

.

mounted on the top flange at 45^{o} with respect to the BB and the electron gun shown in the image (c) and sketch (d).

The chamber was maintained at a base pressure of 1 x 10^{-8} Pa using a diffusion pump (Figure 39). Diffusion pumps use heaters to vaporize oil, such as mineral or silicone. These exhibit high resistance towards thermal decomposition and oxidation. The vapours rise through the centre column and exit the nozzle in a downward fashion forming a curtain of vapours that extend from the centre column to the water-cooled chamber walls. Air molecules inside the chamber hitting the inlet of the diffusion pump are captured by the vapour and are pumped out of the chamber using a rotary pump. Subsequently, the oil-vapours are cooled down by the walls and reach the reservoir for the next cycle.

5.1.3. Electron Source

The chamber is furnished with an OMICRON LEED gun. A tungsten filament generates the electrons through the process of thermionic emission. These electrons are then collimated using electrostatic lenses and are incident normally to the sample. LEED as a technique is often employed in surface science for the determination of the sample crystal structure (66). Electrons are bombarded on a clean sample and a diffraction pattern is observed on a scintillator screen. Elastically backscattered electrons are diffracted by the sample crystal structure and form a diffraction pattern, which is the direct representation of the crystal in the reciprocal space.

5.1.4. Spectrum Acquisition

Spectrum acquisition was carried out using a National Instruments (NI) data acquisition (DAQ) card (PCI-MIO-16XE-10). A data acquisition code was written by the author in LABVIEW to drive the BB voltage and acquire the TTL signal from the output of the CEM pre-amp. The code sent out a low-voltage (0-10 V) signal in a step waveform to the digital-to-analog (D/A) port of the NI card. The analog voltage was then used to control high voltage, negative polarity, power supply (0 to -2 keV). The TTL pulse signal from pre-amp was connected to a 24-bit counter at the input port of the NI card and each pulse was counted in the code (rising edge) for a given dwell

.

time. Subsequently, both the signals were synchronised in the software to generate an electron spectrum.

The remote control of the BB power supply allowed the operator to set the start and stop voltages on the BB, for a wider or a narrower energy scan. The voltage gain of the high-voltage power supply was also incorporated into the code. Figure 40 shows the graphic user-interface (GUI) developed for the spectrum acquisition. The code was tested by sending an input TTL signal from a signal generator. The frequency of signal corresponded to the counts registered in the software. The test was conducted for a range of frequencies from 1 Hz to 10 MHz. This is more than the maximum range needed for the CEM in the counting mode which can range from 1 Hz to 1 MHz.

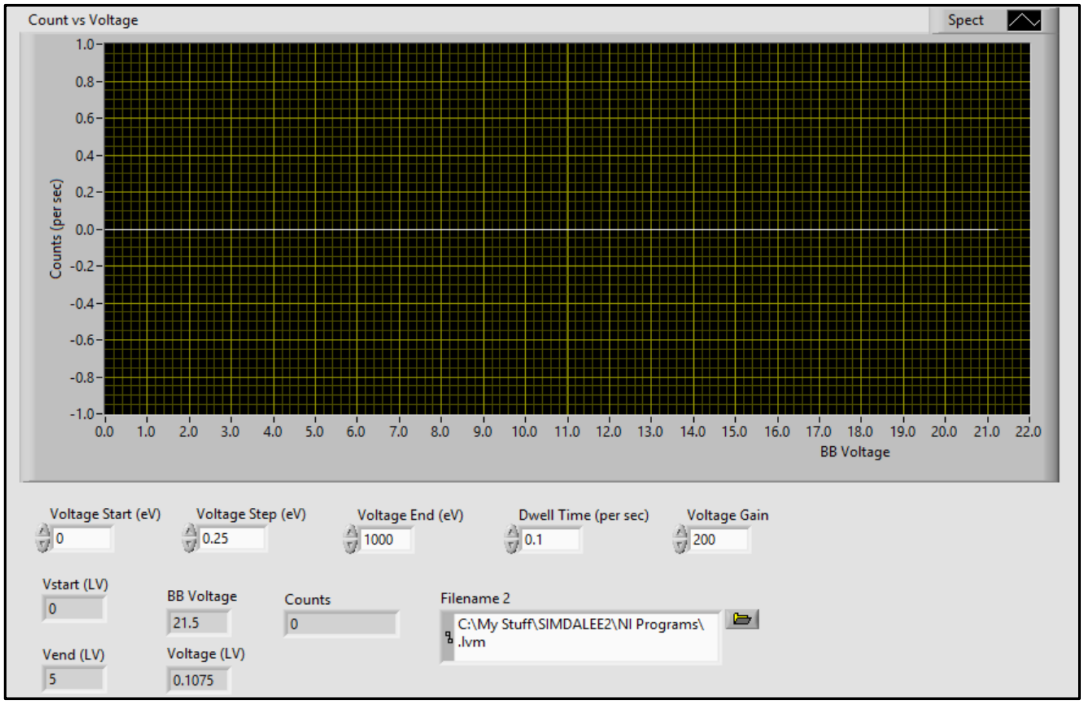

Figure 40 GUI for the code written in LABVIEW for spectrum acquisition in counting mode.

5.2. BB characterisation

The BB is characterised by analysing the experimental spectrum, wherein the BB is tuned to operate near the primary beam energies. Characterisation of the analyser using the elastic peak (EP) not only helps in assessing the performance parameters as

.

predicted by the simulations but also helps in the calibration. For an analyser, the maximum possible detected energy must peak around primary beam energy. Figure 41 shows the comparison between experimentally acquired EP (black curve) and simulated EP (red curve) for the primary beam energy of 1 keV at the working distance of 22 mm. The BB voltages were ramped from -950 eV to -1 keV in equal steps of 0.25 eV. The experimental spectra are smoothed using Savitzky-Golay filter in the OriginLab graphing software (67). The spectrums are normalized with the maximum peak intensity. The FWHM is 4 eV corresponding to a resolution of 0.4% predicted from simulations are in good agreement with the experimental findings. The ratio of the BB energy to the peak-pass energy is defined as the constant of the analyser, as in equation 4. 22 in chapter 4, is also found to be in good agreement with the simulations:

$$K_{BB}(Experimental) = \frac{E_{peak-pass}}{E_{BB}} = 1.0145 \qquad 5.\ 1$$

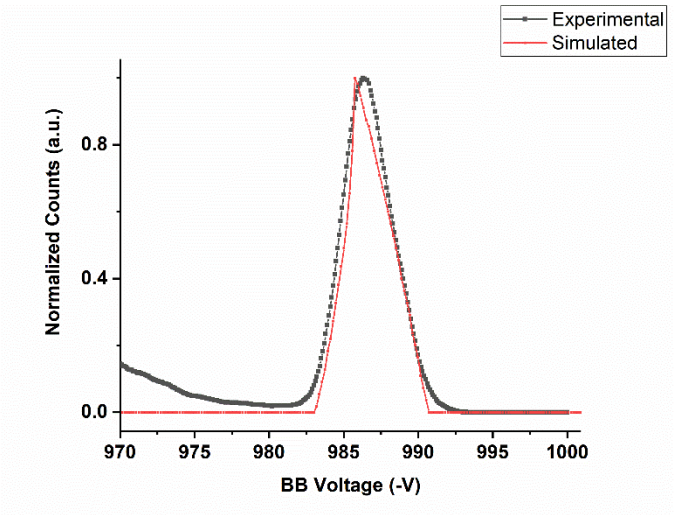

Figure 41 shows the comparison of the experimentally acquired and the simulated spectrum for 1 keV primary beam energy.

The analyser is calibrated using the experimentally acquired elastic peak and the x-axis can now correspond to the electron energies instead to the BB voltage, given by the equation:

.

$$Electron\ energies = V_{BB}K_{BB}(eV) \quad (5.2)$$

The energy analysers are often characterised by the energy resolution. A complete description of the BB's performance is assessed by defining depth of focus (DOF) and field of view (FOV).

5.2.1. Depth of Focus

DOF is defined as the maximum possible displacement in point-source (ΔZ) around the optimized working distance ($Z_{WD} = 22\ mm$), such that the FWHM only increases by 10% ($\Delta E_{total} + \frac{\Delta E_{total}}{10}$). In other words, the resolution of the analyser degrades by 10% (Figure 42a). This can be easily estimated from the discussions on the BB optics in Figure 34a of chapter 4. A 10% degradation in resolution (0.4% to 0.44%) occurs for a displacement of ΔZ = ± 3.5 mm around the optimized working distance and thus DOF is numerically estimated to be 7 mm. This has also been verified experimentally.

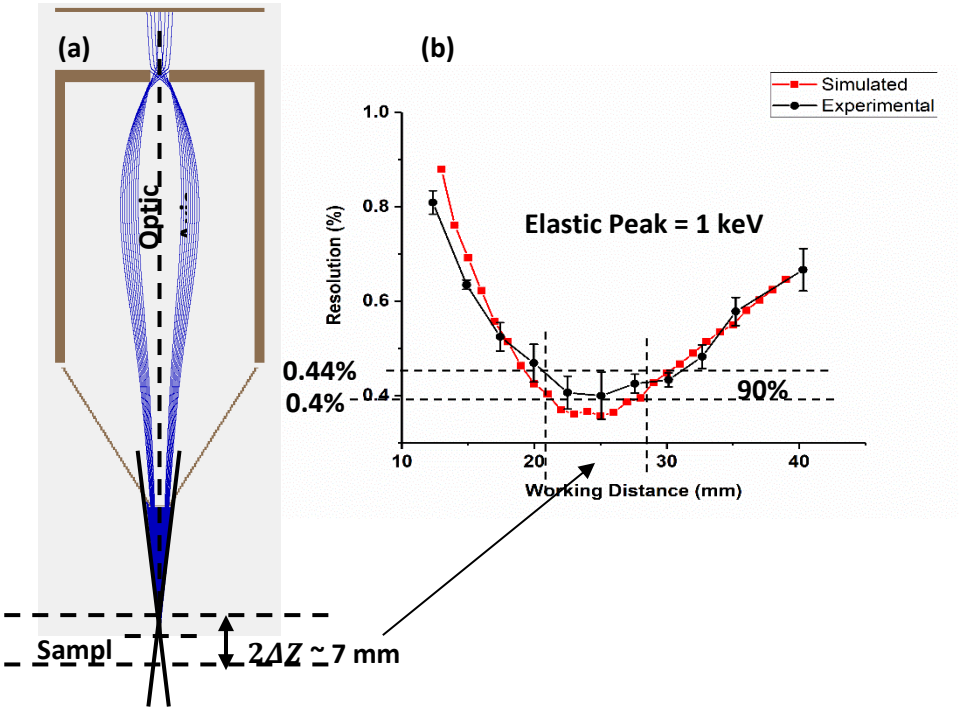

Figure 42 Depth of Focus estimation from simulations (red) and experiments (black).

.

A good agreement between the simulations (red) and experiment (black) can be seen in Figure 42b. This is achieved, by physically moving the BB away from the sample and analyzing the EP obtained at each step. The error bars are calculated from 4 different scans at each working distance with primary beam of 1 keV. A larger DOF ensures the local altitude variations in the sample would remain in focus and decreases the sensitivity of the analyzer's performance to the sample position.

5.2.2. Field of View

A well aligned analyser would imply that the BB optic-axis and the electron gun-axis intersect exactly at the sample-surface. This results in the transmission of cylindrically symmetric trajectories through the BB shown in the acceptance plot of Figure 43(Ic). The experimentally acquired and simulated EP spectrums for such a case are shown in Figure 43(Ia) and (Ib), respectively. As the point source is moved off-axis to a maximum of 400 μm, a shoulder starts to appear at the falling edge of the EP, seen both in experimental and simulated curves (Figure 43(IIa) and (IIb) respectively). The simulated spectra are numerically computed by moving the point-source off-axis and analyzing the acceptance plot at every radial step. Figure 43(IIc) shows an acceptance plot generated for electrons with a constant pass energy of 1 keV. The x-axis now corresponds to the BB energy. The shoulder on the EP is a result of the transmission of cylindrically asymmetrical trajectories of a 1 keV electron through the BB. The point-source in the simulations is moved below the optic axis, the lower negative-angled trajectories (Figure 43(IIc)) now experience lower field gradients and therefore can be transmitted at lower BB biases.

Moving the point source further away from the optic axis introduces artefacts in the experimental spectrum of Figure 43(IIIa). The physical interpretation of the artefact is understood using the acceptance plot in Figure 43(IIIc). The electron trajectories at about 1000 μm off-axis have near line of sight through the BB. This results in 'split-peak' effect that can also be seen in the simulated spectrum in Figure 43(IIIb). This is the physical case, where the analyser is highly misaligned and needs to be corrected for.

.

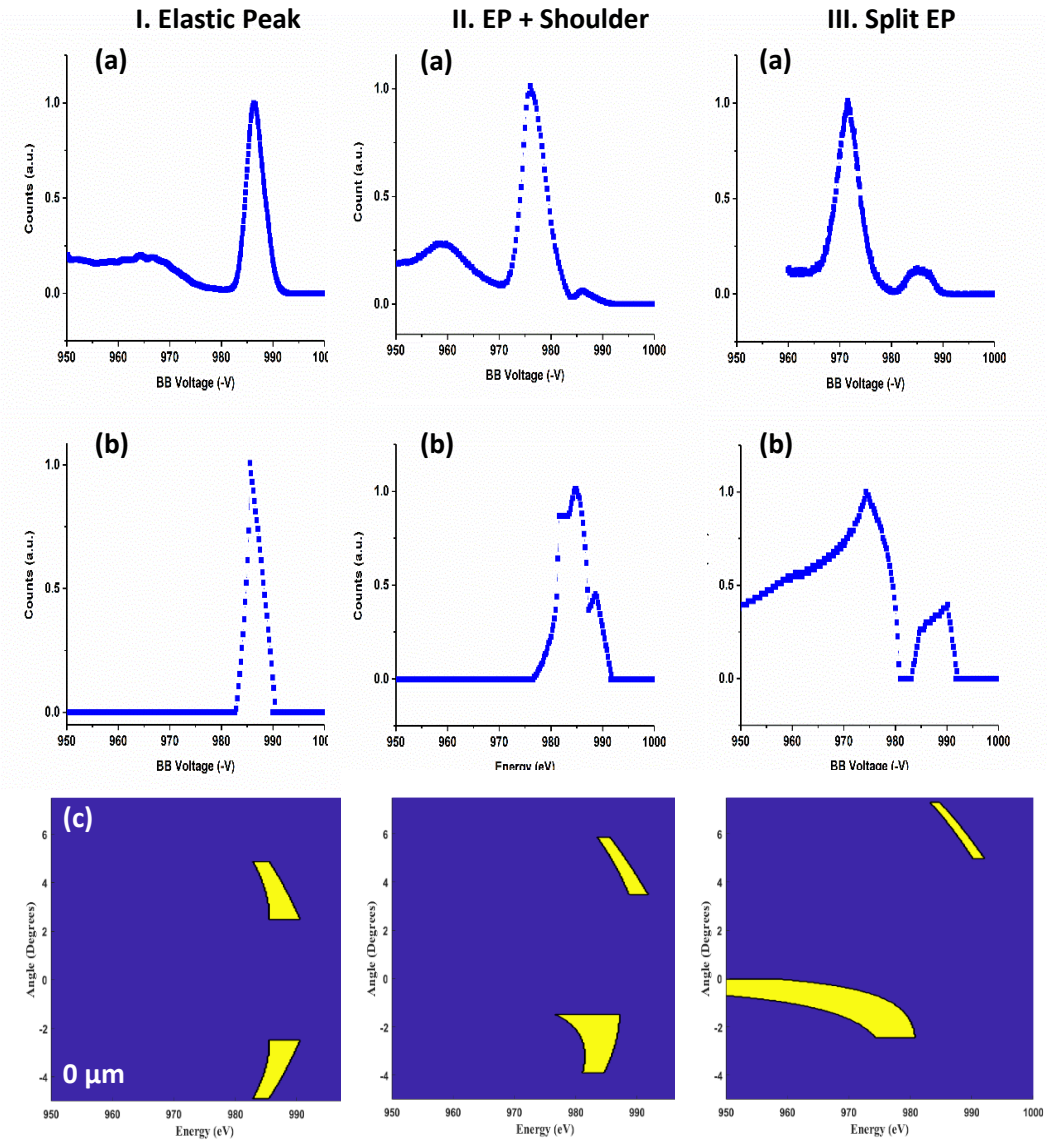

Figure 43 Comparisons of experimental (a) and simulated (b) spectra for different radial positions of the point-source at (I) 0 µm (II) (I) 400 µm and (III) 1000 µm with corresponding trajectories summarised in the acceptance-plots (c)

Similar to the definition of DOF, field of view (FOV) of the BB analyser can defined as the maximum possible displacement in point-source ($\Delta\rho$) around the BB optic axis. ($\rho_o = 0\,mm$), such that the FWHM only increases by a factor of F% ($\Delta E_{total} + \frac{\Delta E_{total}}{\mathrm{F}}$). This definition of the FOV is particularly important for imaging, wherein, the area to be scanned should be restricted within the definition of FOV. From the discussions on the BB alignment in Figure 43, it is now known that the peak-shape

.

starts to distort when the point source is moved to 400 μm or more off-axis. This corresponds to an upper limit for the definition of FOV. For AES detection, a condition of F = 10 can be imposed on the definition FOV. On the other hand, a flexible condition of F = 20 can be imposed for SE imaging. Figure 44 shows % change in resolution (left y-axis) and % change in total count (right y-axis) as the source moves away from the optic axis. A 20% change in FWHM/resolution corresponds to a field of view of 380 μm x 380 μm of area. While a 10% change corresponds to a FOV of 200 μm x 200 μm. Note that the net count or area under the simulated spectrum increases by 3% and 1.5% for F = 20 and 10 respectively. The broadening of the peak also results in peak shift by ± 0.5 eV and ±0.25 eV for F= 20 and 10 respectively.

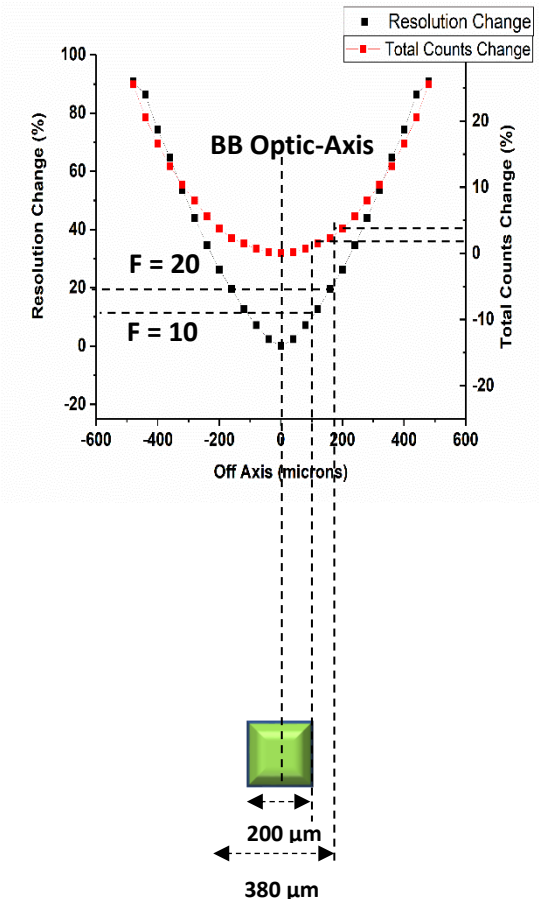

Figure 44 Definition of FOV with F= 10 for AES detection and F = 20 for SE detection. The graphs shows % resolution change with respect to the radial position of the point-source (black curve). This leads to a reduction of total count change of 3% (red curve).

.

5.3. Electron Spectrum

A freshly inserted n-doped silicon (111) sample was initially degassed overnight by heating at 400^{o} C. Following which, the Si sample was annealed at 900^{o} C for 10 min to remove contamination. Figure 45 shows 1x1 LEED diffraction pattern acquired at 104 eV primary beam energy.

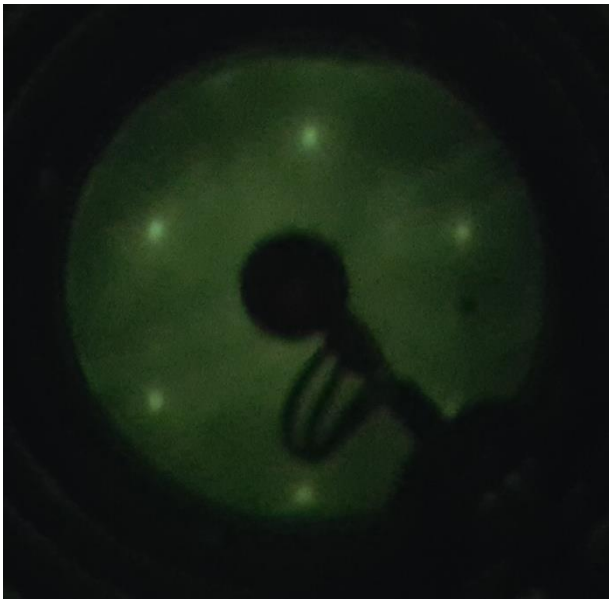

Figure 45 A 1x1 LEED diffraction pattern acquired at 104 eV from a clean Si (111) surface.

A spectrum is acquired from silicon sample at 800 eV primary beam energy with a beam current of 50 nA. The y-axis of the raw spectrum (Figure 46a) represents count rates in the $EN(E)$ form as the BB's energy window for collection increases linearly with energy ($\frac{\Delta E}{\mathrm{E}}$ = constant). The spectra in Figure 46 and Figure 47 presented are averaged from three scans and are smoothed using Savitzky-Golay filter in OriginLab graphing software .

The spectrum shows an SE peak, observed at 12.5 eV from a grounded sample with elastically scattered electrons peaking at 800 eV. A shoulder can be seen on the falling edge of the SE peak in Figure 46a. This feature is the Si LVV Auger peak, which is also observed in the differentiated spectrum (Figure 46b). The features observed near

.

EP correspond to the plasmon losses. A bulk plasmon peak is observed at 17.3 eV in the energy loss spectrum of Figure 46c which is in good agreement with the reported literature data (68) (69). A bulk plasmon peak has been previously reported at 16.8 eV. Higher order plasmon peaks can also be seen in the energy loss spectrum at 34.5 eV and 52.5 eV (Figure 46c).

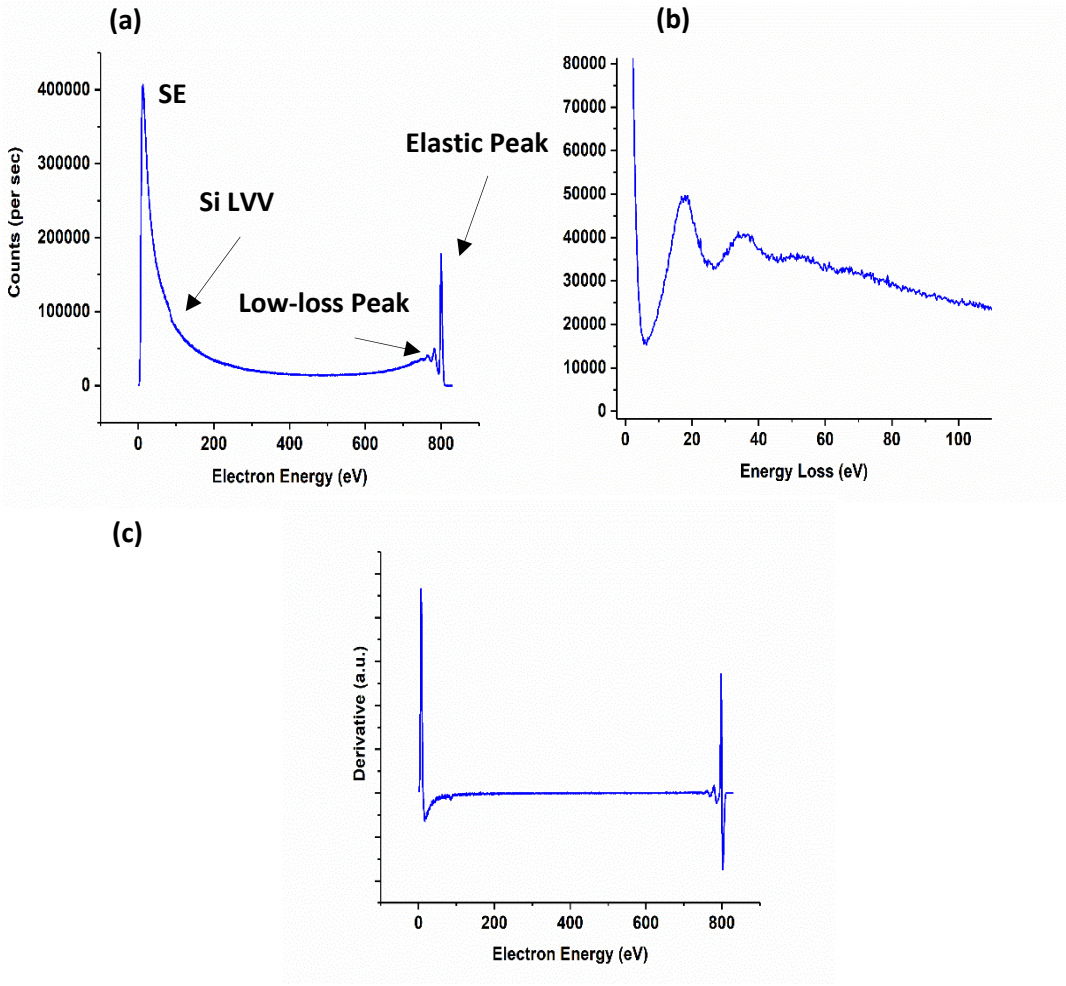

Figure 46 (a) Electron spectrum acquired from the bombardment of 800 eV electron beam on silicon (111) sample. (b) Electron loss spectrum showing Si bulk plasmon resonance peaks with the first peak observed at 17.3 eV. (c) Differentiated spectrum.

Figure 47a shows the silicon Auger feature observed as a shoulder in the raw spectrum. Si LVV peak is observed at 85 eV in the differentiated spectrum. Silicon peak is found to be positioned at lower energies in comparison with the reported peak position of 92 eV in the differentiated spectrum (70). This shift to the lower energies is due to the

.

presence of oxygen on the sample. A weak oxygen peak is seen in the raw spectrum and corresponding Auger peak can be seen at 505 eV in the differentiated spectrum. The presence of carbon was also checked. A clear and obvious feature was not observed in the expected energy region. However, a discernible carbon Auger peak is observed in the differentiated spectrum observed at 272 eV, which is good agreement with reported values (70).

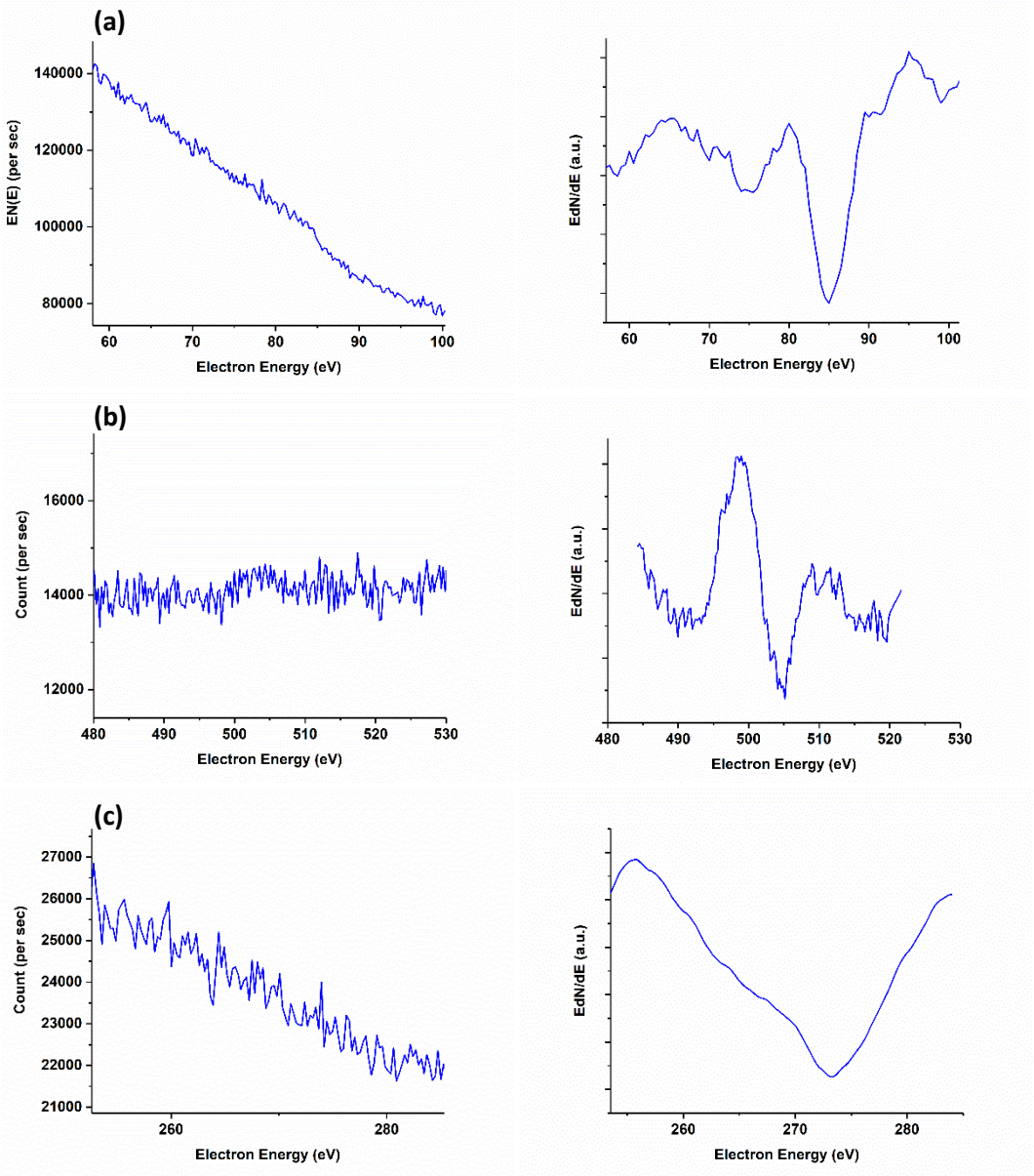

Figure 47 Graphs on the left show Auger features as observed in the raw spectrum and in the differentiated spectra shown on the right for (a) silicon (b) oxygen and (c) carbon acquired from Si (111) sample at 800 eV primary beam energy.

.

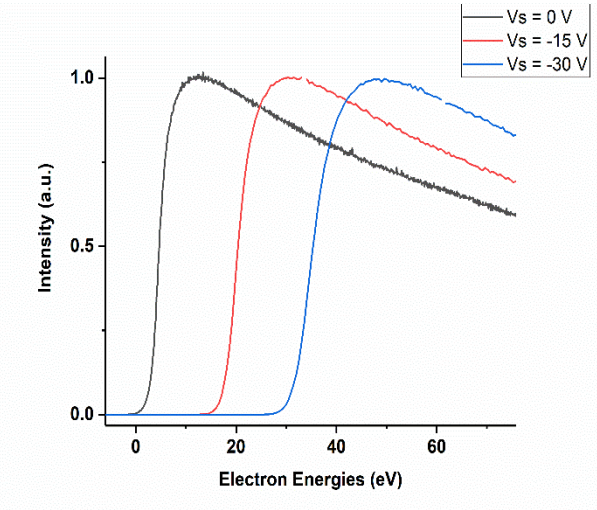

Figure 48 Shift in the SE peak with the sample bias of 0 V, -15 V and -30 V.

Biasing the sample negatively, shifts the spectrum to higher energies because the electrons emanated from the sample are accelerated towards the analyser with an additional energy. Figure 46c shows shift in the low energy peak in similar steps corresponding to the negative bias applied to the sample: 0 V, -15 V and -30 V, as expected. The presence of oxygen in the spectrum also confirms the observation of higher SE emission from the silicon sample (71). The SE peak intensity is small for pure element like silicon (69) but has been reported to be larger in the from the oxides (71). The SE intensity is sensitive to the composition of the surface.

5.4. Preliminary Results: SFEM BB

Proof of principle experiments for the BB designed for SFEM was carried out by the author at ETH Zurich in a UHV chamber equipped with a thermionic electron gun (Figure 49a). Similar to the experimental setup at York, the BB was mounted on a linear drive which was orthogonal to the electron gun. The sample was mounted at 45^{o} to the BB axis and the electron gun axis (Figure 49b). The BB analyser is coupled with a CEM purchased from Sjuts optotechnik. An 760 eV primary-beam was bombarded on a graphene film on a copper sample with a probe current of the order of 100 nA.

A copper-on-graphene sample was provided by Dr. Oghuzan Gurlu. Figure 49c shows first result from the smaller BB design. SE peak is observed at 8 eV. Carbon Auger KLL peak can be also be seen in the raw spectrum which is observed at 265 eV in the

.

differentiated spectrum (inset of Figure 49c). These experimental results along with the simulation results for this BB design are published and can be found in the reference (72).

It is noted that electrons are detected even with a 0 V bias on the BB. Furthermore, the SE peak is superimposed on a background, as opposed to the experiments carried out with the bigger BB design at York. This is due to internal scattering and is discussed in chapter 6.

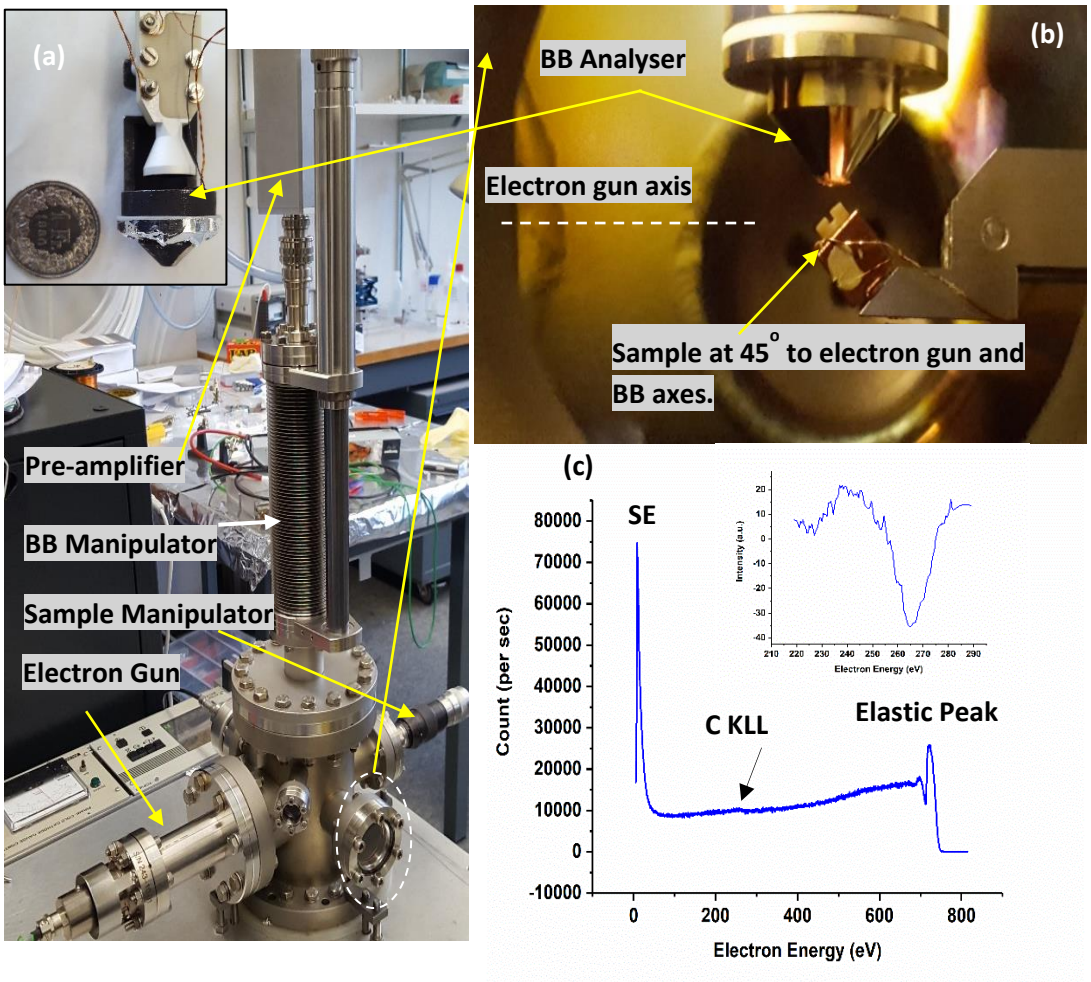

Figure 49 (a) Experimental test chamber used at ETH Zurich. (b) Sample was mounted at 45° with respect to the sample and the BB. (c) First result acquired from the smaller BB design from a graphene on copper sample. The inset shows the carbon KLL peak in the differentiated spectrum.

.

5.5. Summary

This chapter discussed the experimental setup and characterisation of the BB design. The experimental findings are in good agreement with the simulated results. The figure of merits for the BB analyser are as follows: resolution 0.4%, DOF =7 mm, FOV = 380 μm x 380 μm for imaging and 200 μm x 200 μm for spectroscopy The BB approaches the resolution of the cylindrical mirror analyser (CMA). The high depth of focus along with a compact design also demonstrates the transferability of the device, which can be used as an add-on component in a variety of scanning electron microscopes.

.

Chapter 6: Detection and energy analysis of SE using BB in JEOL SEM

In the final phase of the thesis, characterization of BB analyser was extended to the SEM environment. BB mounts were modified, and a bespoke flange was constructed in house (with assistance from the mechanical workshop) at UoY to enable integration of BB analyser in the JEOL 7000F field emission SEM. To perform experiments with the above-mentioned modifications, scanning control of the SEM was achieved This was followed by the demonstration of Auger and SE spectroscopic analysis. Furthermore, a copper on silicon test-sample was examined for image acquisition in the SEM coupled with BB analyser.

6.1. Experimental Setup

The specimen chamber of JEOL 7000F had three available ports, as shown in Figure 50a. Port 2 was found to be the most suitable one for mounting the BB assembly to circumvent the geometrical constraints imposed by the SEM chamber and proximity of the BB to the objective lens, ET detector and sample stage as shown Figure 50b. Similar to the UHV setup, the BB mounting port was orthogonal to the electron beam and the sample was tilted at 45^{o} with respect to the electron gun and the BB for the experiments (Figure 50b-c).

Although mounting the BB assembly on port 2 provided sufficient distance from the ET detector, modifications to the BB assembly design, described in chapter 5 (Figure 37), were still required. A reduction in outer diameter was needed to avoid point of contact with the sample stage and objective lens. Reduction in the total length of the assembly was also needed to accommodate the BB assembly inside the specimen chamber (average radius of 190 mm). The x, y, z and ϕ manipulator with an adaptor flange used previously was heavy and bulky which would have needed extra support from the SEM's base. Any modifications to the SEM other than the mounting flange were avoided. Furthermore, these extra degrees (x, y, and ϕ) of freedom were not

.

required and therefore the BB assembly was attached to a single linear drive. Specific modifications to the assembly are discussed in the next section.

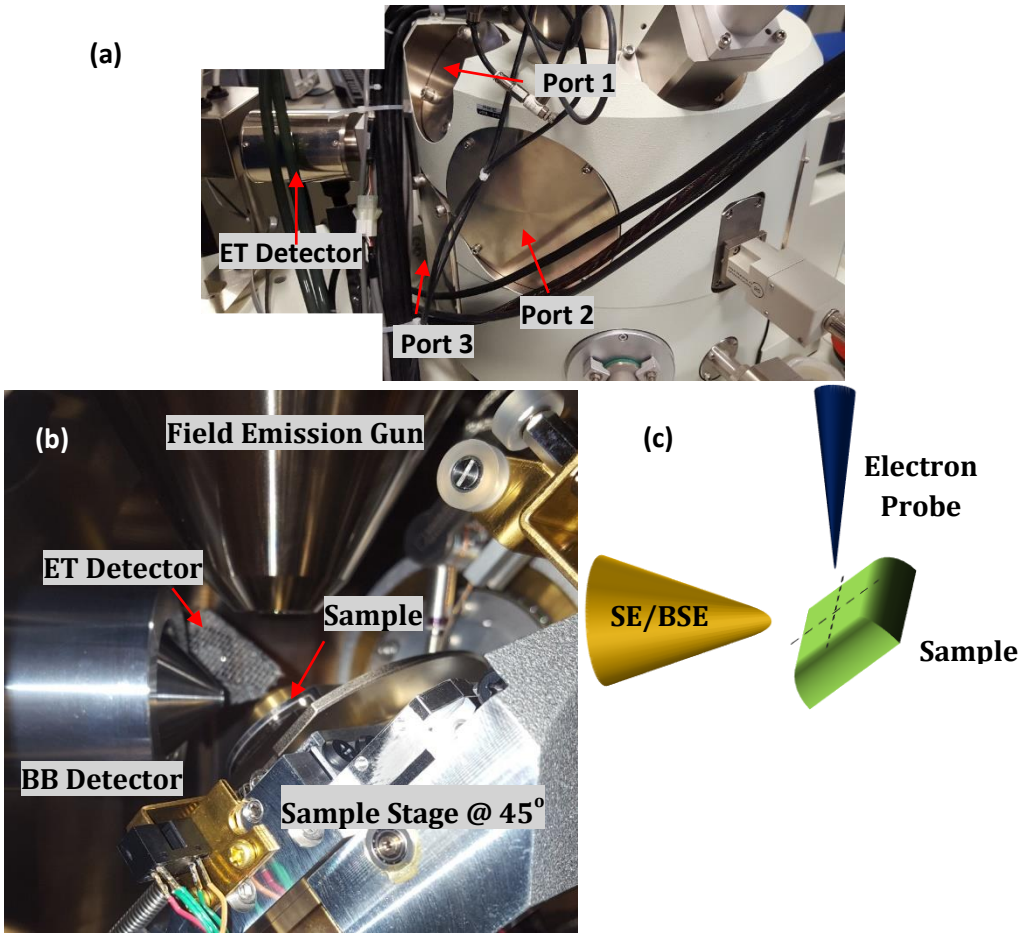

Figure 50 Experimental setup in SEM(a) Available ports for mounting the Bessel Box(b) Experimental assembly showing the sample mounted at 45º to the electron gun and the BB detector. (c) Schematic of the experimental geometry shown in b.

6.1.1. BB Detector Assembly

The modifications were needed to make the BB assembly much more compact. Care was taken to shorten the length and the diameter by using a compact CEM and modified mounts. These were then mounted on a bespoke flange for JEOL SEM on a linear drive. The description of the modifications to BB assembly is as follows:

.

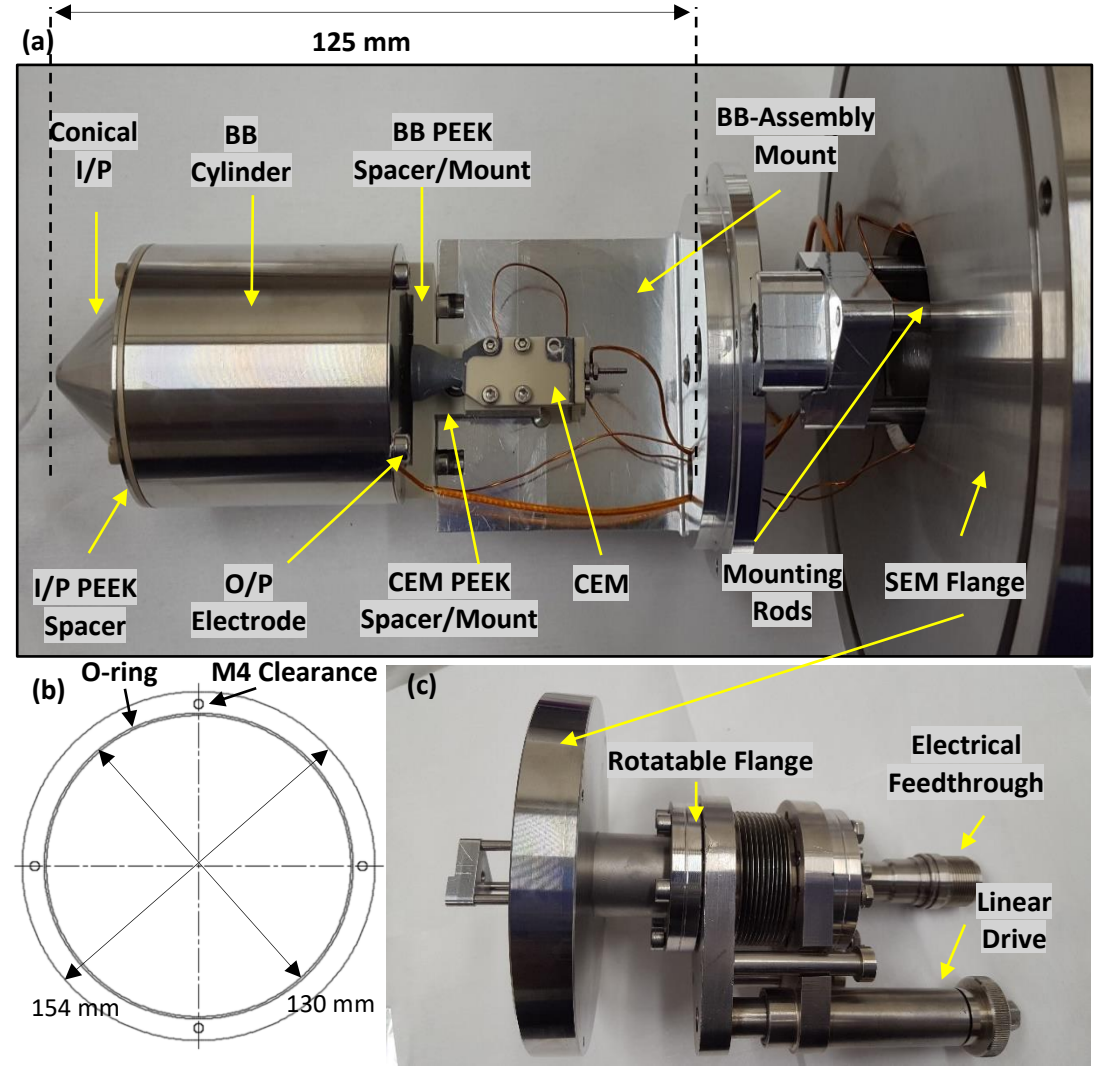

Figure 51 (a) BB assembly with modified mounts, a compact channeltron from Sjuts and a bespoke mounting flange for JEOL 7000F SEM (b) CAD drawing of the SEM mounting flange (c) SEM flange interfaced with linear drive and electrical feedthroughs.

1. Compact CEM: As discussed in chapter 5, the overall BB-assembly length was limited by the CEM length, therefore, a compact CEM was purchased from Sjuts optotechnik Gmbh (part no.- KBL 10RS) which had a total length of 34 mm. This allowed for the reduction in the combined length of the BB-CEM (including input cone) from 165 mm for UHV test setup to 125 mm for SEM (Figure 51a). Similar CEM was used in the compact BB design for SFEM, at eth Zurich.

.

2. Modified Assembly Mounts: In order to reduce the outer diameter of the assembly, a new assembly-mount was fabricated as shown in Figure 51a. The BB cylinder was now tapped onto this mount through a PEEK spacer instead of mounting on the inside of the shielding-cylinder (as in the UHV setup). This allowed, for the reduction of the inner diameter of the shielding-cylinder. A reduction to 55 mm was achieved from 70 mm for the outer diameter of BB-assembly. The CEM was also tapped through a PEEK block onto the same mount.
3. SEM Flange: A bespoke flange was fabricated for JEOL SEM of outer diameter 154 mm as shown in the CAD drawing of Figure 51b. This was interfaced with a linear drive (Figure 51c) using a $2\frac{3}{4}''$ rotatable conflat flange. Finally, electric feedthroughs purchased from Allectra (part no.- DN16CF) were interfaced with the linear drive.

6.2. JEOL 7000F: External Scan

The external scan can be accessed from the SEM's magnification-control printed-board (mag-PB). The mag-PB is a part of the electron optical system (EOS) control-unit located on the SEM's front panel as shown in Figure 52. A test cable with a 14 contact, D-sub ribbon-type plug (from Amphenol) was made. This was interfaced to the corresponding socket provided for external scan located on the mag-PB. The test cable comprised of 4 wires corresponding to the 4 pins needed for the external scan as shown in Figure 52.

.

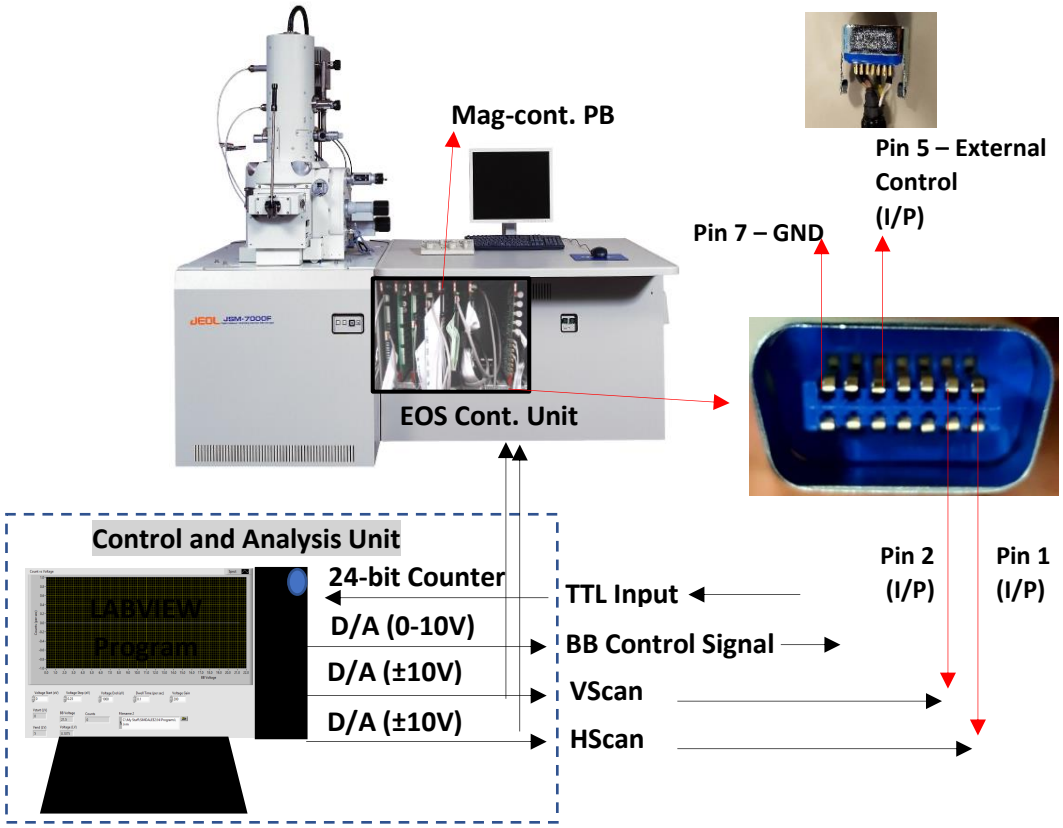

Figure 52 Block diagram for external scan: showing the location of the magnification control PB mounted on the EOS control unit on JEOL 7000F SEM's front panel. Also shown is the plug needed to interface with the mag-PB.

1. Pin 1 referred to a line or horizontal scan (Hscan) signal and Pin 2 corresponded to a frame or vertical scan (Vscan) signal. These needed ±10 V analog signals and were connected to the digital-to-analog (D/A) ports of the NI-DAQ.
2. Pin 5 referred to the SEM's scan control signal. SEM's scan system is active when pin 5 remains at 5 V level and external scan is activated when the pin 5 is pulled-down to a 0 V level. This can be controlled using a computer program, but for the time being was manually grounded whenever external scan was needed for imaging using the BB detector.
3. The wire connected to pin 7 was grounded.

In addition to the NI data acquisition card (PCI-MIO-16XE-10) previously used, another NI acquisition unit (NI myDaq) was interfaced with the computer to control BB voltages. The 2 D/A ports available on PCI-MIO-16XE-10 were now used for

.

Hscan and Vscan signals for scanning. Pulse counting was carried out by the 24-bit counter of the PCI-MIO-16XE-10, as before.

6.2.1. Image Acquisition

Spectrum acquisition in the SEM was carried out with the hardware (Figure 38) and software (Figure 40) setup as described for the UHV experiments in chapter 5. A new code for image acquisition using the BB detector was written by the author in LABVIEW. This involved a three-step procedure, discussed below.

6.2.1.1 Raster Scan

For a single raster scan, the code generated a single Vscan and multiple Hscan step-waveforms at the D/A ports of the NI-DAQ. These analog sawtooth waveforms were used to drive SEM's external scan. Figure 53a shows a schematic of the timing diagram of Hscan and Vscan analog signals (in green) for a single raster scan. A single Vscan step, corresponding to a single line scan, was synchronized with a complete set of Hscan steps (Figure 53a in black).

The number of Vscan steps and hence the number of lines of the raster were determined by the number of vertical pixels (V_n) desired. Similarly, number of Hscan steps were determined by number of horizontal pixels (H_n). The code allowed to set start (V_{start} and H_{start}) and end (V_{end} and V_{end}) voltages of the Hscan and Vscan signals allowing, in a nutshell, selection of a region of interest at the magnification set by the SEM. When Hscan and Vscan = 0 V, it corresponds to the centre of the physically scanned area and the central pixel in the image. Figure 53b shows image quadrant with respect to the scanning voltages polarity. For imaging with the BB detector, V_{start}/H_{start} = 7.5 V, and V_{end}/H_{end} = -7.5 V and the number of pixels (V_N/H_N) were set equal.

.

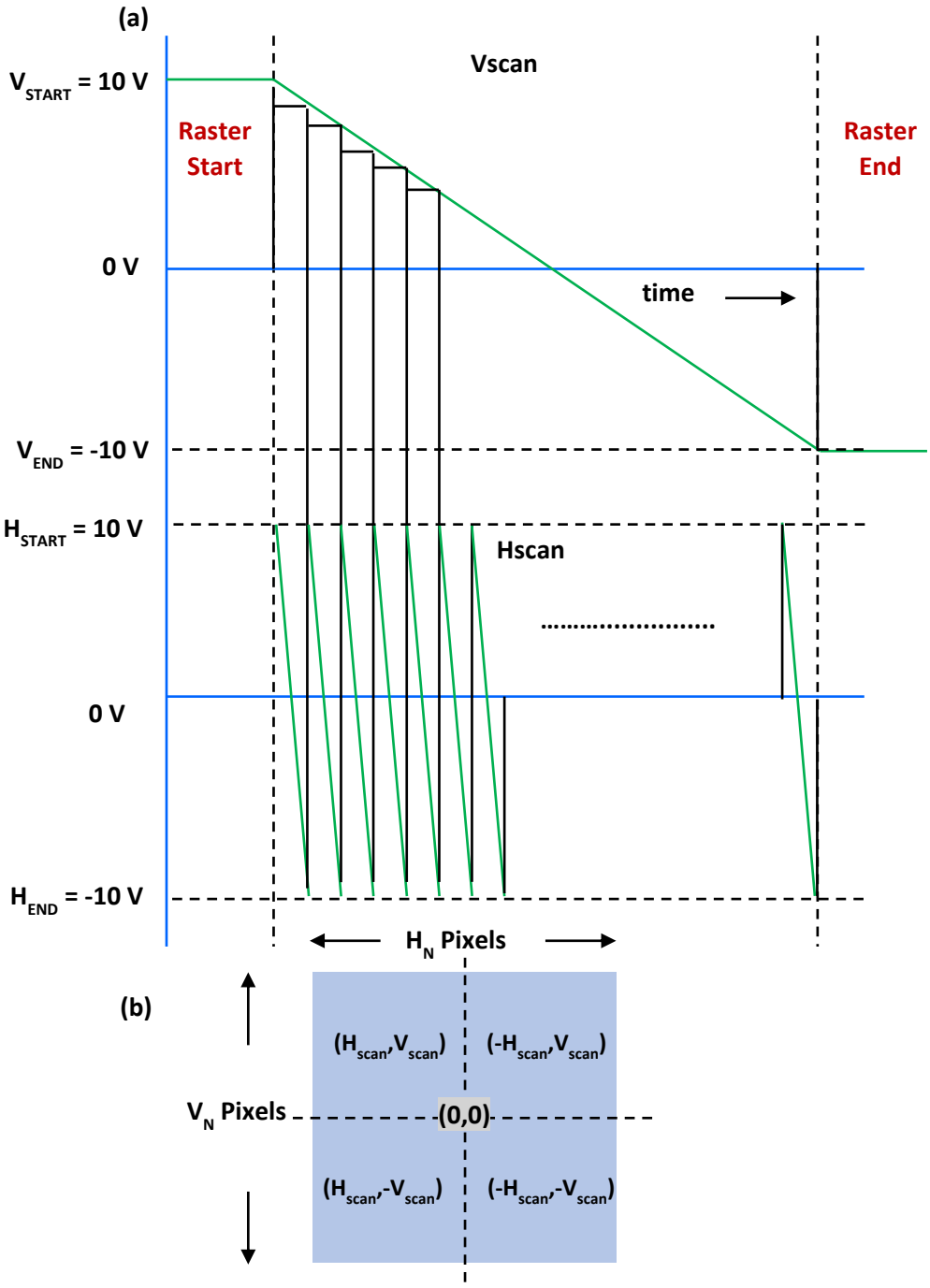

Figure 53 (a) Timing diagram of Hscan and Vscan sawtooth waveforms (in green) and Vscan step waveform (in black). (b) Image quadrants with respect to the polarity of the scanning voltages.

6.2.1.2 TTL Pulse Counting and Image Matrix

.

As previously stated, a single Hscan step correspond to a single pixel in an image. The time width of a single Hscan step was determined by the software-controllable dwell-time. The TTL pulse signal from the pre-amp was counted within this dwell-time. Finally, the counts were registered as the raw pixel-intensity corresponding to the index values of the Hscan and Vscan signals. Thus, an image matrix was generated with each matrix element corresponding to the raw count values (per sec) as shown in the timing diagram of Figure 54.

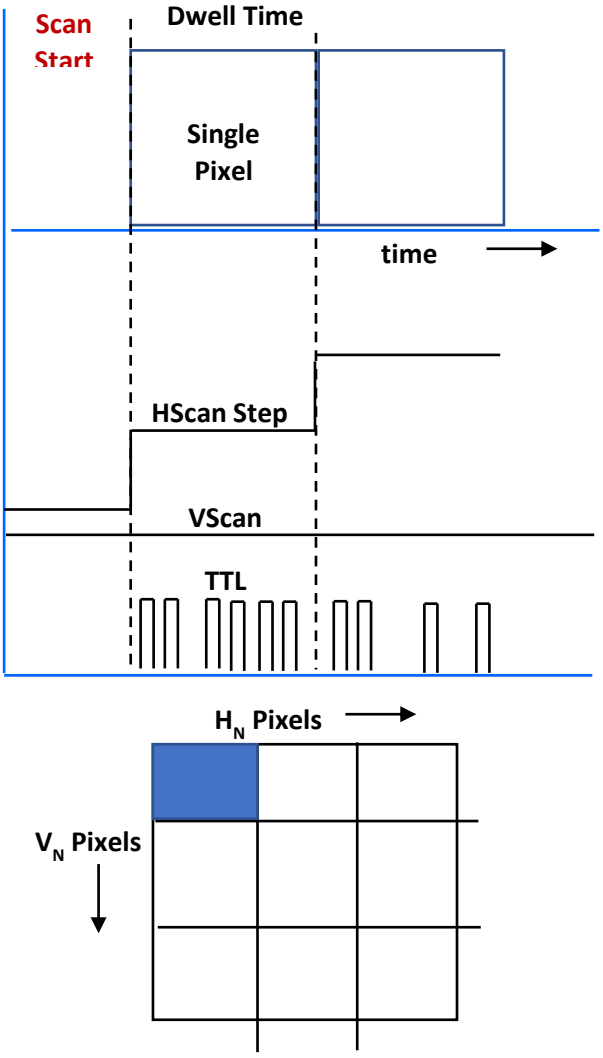

Figure 54 Timing diagram for the registration of the count value for a single pixel.

6.2.1.3 Imaging

.

Finally, the raw image-matrix was converted to a 16-bit grey- scale image. This step was also incorporated in the LABVIEW code. However, a code written in MATLAB by the author, was found to be easier to use for performing basic image processing algorithms on raw matrix, such as brightness, contrast etc. Figure 55a shows GUI for scanning and imaging written in LABVIEW. Figure 55b shows a low magnification ET image of an aluminium stub taken at 10 keV primary beam energy. The scanned region corresponds to an area of 6 mm x 6 mm. Figure 55c shows the first image taken with the BB detector.

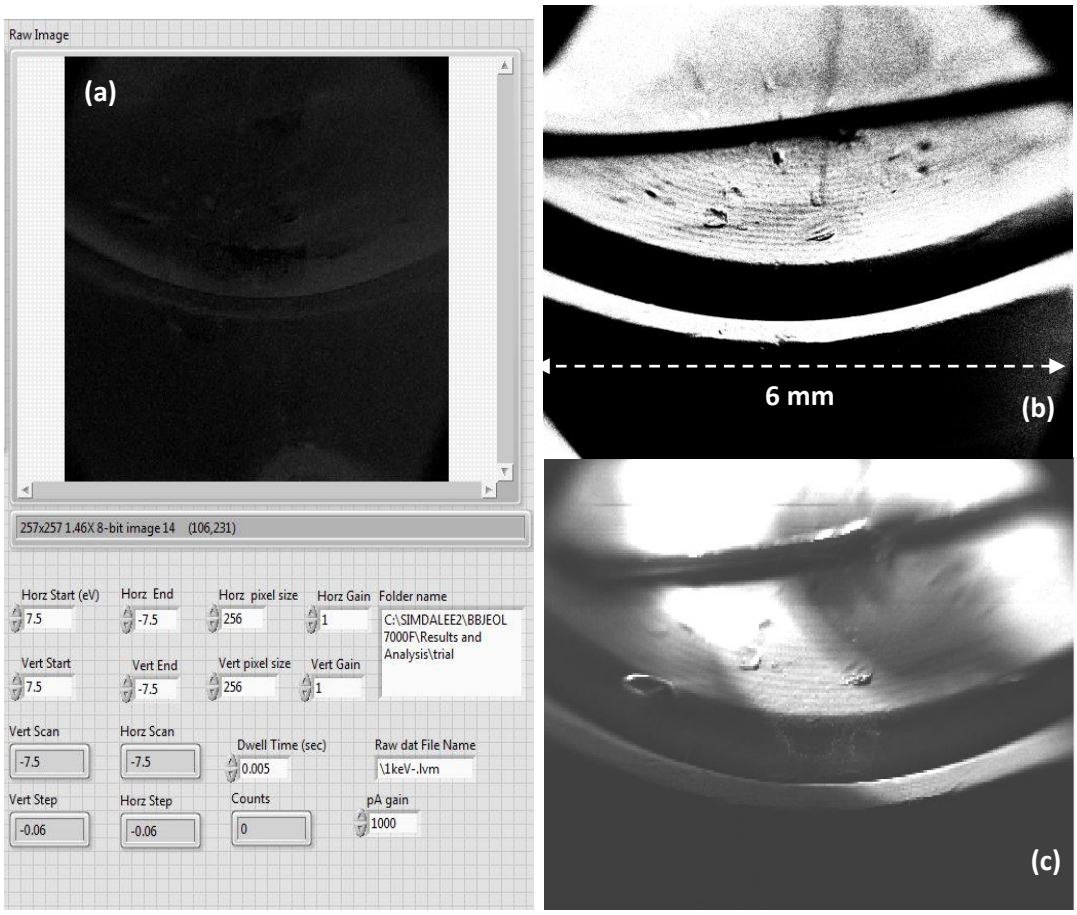

Figure 55 (a) GUI for the code written in LABVIEW used for SEM's external scan control and for generating image matrix. (b) Low magnification image of aluminium taken with a 10 keV probe with (a) ET detector (b) BB detector.

.

The BB image corresponds to a pixel resolution of 512 x 512. In comparison with the ET image, the features of the stub are reasonably reproduced by the BB detector. An elliptical bright feature is seen in the BB image, which is not seen in the ET image. This is an artefact which is observed at the lower SEM magnification and is related to the BB detector's FOV. This is elaborated below.

6.3. BB Detector Alignment

As defined in chapter 5, the FOV of the BB detector corresponds to a maximum scanned area of 380 μm x 380 μm. When a larger area is scanned, the off-axis electrons have near-line of site to the output aperture and large number of electrons with energies higher than BB energy are detected. The shape of the artefact observed in the BB image corresponds to the projection of the input aperture on the sample. The BB detector was mounted at -35^{o} with respect to the sample-exchange chamber as shown in the SEM's top view (Figure 56a). Initially, the sample was mounted on a flat stub and tilted at 45^{o} with respect to the electron gun and the BB optic axis. This results in the elliptical projection of the BB's annular input aperture in the BB image (Figure 56c). For the alignment, the centre of the projection in the BB image must coincide with the central pixel in the image. A sample-stub with top face sliced at 45^{o} was fabricated (Figure 56b). The as-inserted sample stub resulted in the elliptical projection in the BB image, as expected. Rotating the sample-stage by -35 ^{o}, resulted in the decrease in ellipticity of the aperture projection. Figure 56d shows a percentage change in the total detected counts with respect to the position of the beam on the sample and the BB optic axis. A qualitative one-to-one correlation is established between the numerically computed counts to the grey-level intensities in the BB image (at constant BB bias). Figure 56e shows the projection of the annular aperture after the alignment was achieved. The scanned area in the BB images in Figure 56 is 6 mm x 6 mm. This corresponds to a physical length of ~10 microns with pixel resolution of 512 x 512. This falls well within the definition of FOV.

.

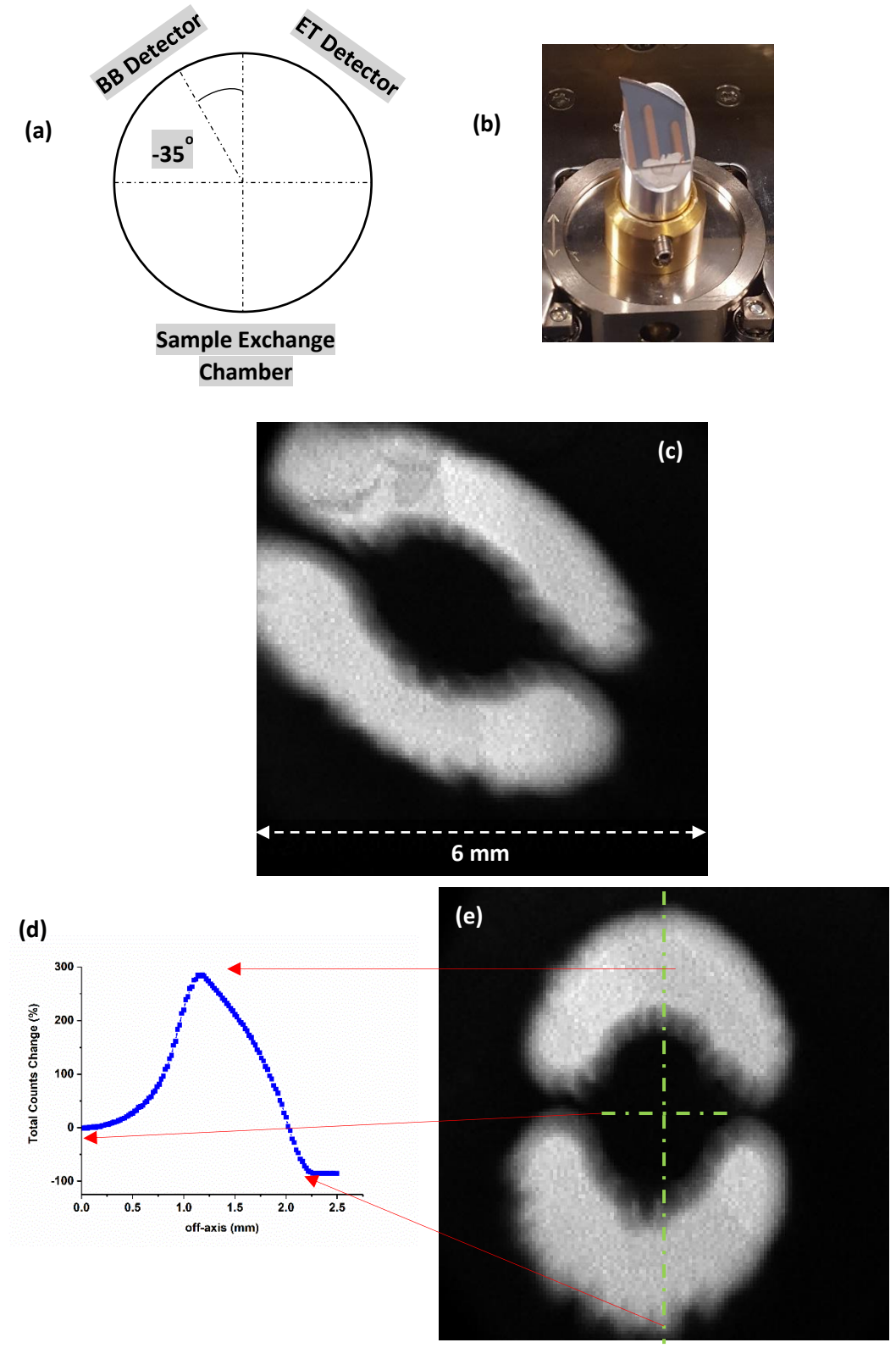

Figure 56 (a) Top view of the JEOL SEM , showing relative position of the BB detector, ET detector and sample exchange chamber. (b) A modified sample-stub with the top face tilt at 45°. (c) BB image acquired at 10 keV beam energy showing elliptical

.

projection of the input aperture. (d) percentage change in the count rate with respect to the beam position on the sample and the BB optic axis. (e)

6.4. Experimental Results

6.4.1. Microscopy

The sample used in the experiments consisted of a 100 nm thick layer of copper deposited on a silicon substrate. The sample was plasma cleaned ex-situ before inserting into the SEM. Plasma cleaner from Diener Electronic GmbH was used. The sample was cleaned at 25% instrument power for 3 min. Figure 57b shows an SE image, obtained using the microscope's ET detector, of the copper-on-silicon sample. Firstly, narrow energy spectra (0-100 eV) were acquired using the BB detector from the Si and Cu regions (regions marked in red in the ET image). A 10 keV primary beam energy with a beam current of the order of 17 nA was used. The raw SE spectra (Figure 57a) from both the regions are superimposed on a background. A straight line is subtracted from the spectra with the y intercept at the onset of SE emission and a slope of 20^{o} for both the regions. Si LVV and Cu MVV low energy Auger peaks can be seen in the direct spectrum at 78 eV and 53 eV, respectively. The SE peak in the copper and silicon regions are seen at 8.9 eV and 10.1 eV, respectively. For imaging, the BB detector is tuned to a pass energy of 12 eV. Figure 57c shows a raw image with a pixel resolution of 512×512 of the same area (250 μm x 250 μm) as acquired for the ETD image of Figure 57b. As for the ETD image, in the BB image the Cu region is brighter in contrast than the Si region. Generally, this is related to the relative differences in the secondary electron yields (SEY) of copper and silicon (71). The features observed in the BB and ET detector image are in reasonable agreement with each other. Multiple scans at various pixel resolutions were also taken (128x128, 256 x 256).

Bright features can be seen on the copper region in the ET image. This is possibly to due to oxidation. Changing the plasma cleaning conditions, alters the shape and location of these features. A contrast reversal can be seen from this region in the BB image. This was probably due to an increase in carbon presence because of carbon-cracking at the sample, which is pronounced due to prolonged beam exposure during

.

BB imaging experiments. At this stage it has to be pointed out that the current scanning setup is incapable of achieving TV scan rates. The best possible timing resolution from the software and hardware setup was 5 ms per pixel. All the BB images in this study were taken at 10 ms dwell time. Normally, additional hardware is interfaced which can store a frame before the software can process it. Dedicated software packages from the manufacturers can then drive the external scan at higher scanning rates.

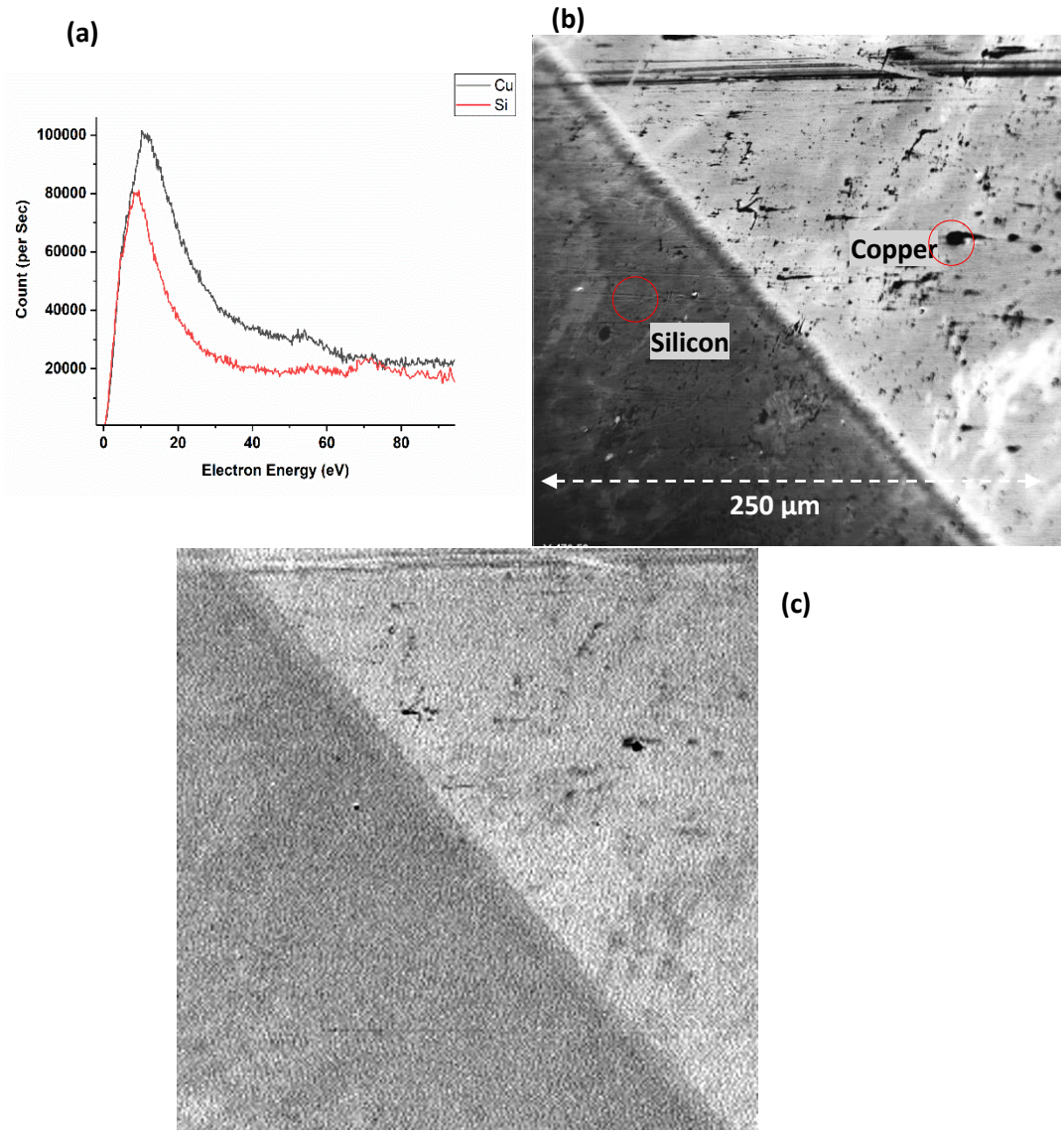

Figure 57 (a) shows the SE spectra from a copper-on-silicon sample, as shown in the ETD image in (b). The features observed on the low energy spectra are Si and Cu Auger peaks. (c) shows the energy-filtered image obtained with the BB detector tuned to a 12 eV pass energy.

.

6.4.2. Spectroscopy

A wider energy scan was acquired from the Si and Cu regions. Figure 58a shows a raw spectrum (average of 3 scans) acquired from the copper region. Figure 58b shows the spectrum after background subtraction. As would be expected from an SEM environment, oxygen and carbon peaks are seen in the differentiated spectra at 510 eV (Figure 58c) and 271 eV (Figure 58d) respectively. These values are in reasonable agreement with the reported values from a differentiated spectrum (70). Oxygen can also be seen in the direct spectra at 502 eV. This is an expected difference, as the differentiated peaks are located at higher energies compared to the position in the direct spectra (73).

Low energy copper MVV peak can be seen at 57 eV in the differenced spectra (Figure 58e) and copper LMM peaks are observed at 762 eV, 832 eV and 908 eV in the direct spectra and at 772 eV, 842 eV and 918 eV in the differentiated spectra (Figure 58f). The peaks are observed at slightly lower energies due to the presence of oxide layer (reported values in literature are 920 eV, 840 eV and 776 eV respectively for the differentiated spectra (70)).

Similarly, Figure 59a shows the raw spectrum from the silicon region in the sample. Si LVV peak is observed at 78 eV in the differentiated spectrum (Figure 59c). This peak is seen at lower energy as opposed to the one observed in the UHV system which was at 84 eV. This is most likely due to higher carbon contaminants on the silicon surface in the SEM system. The Si LVV has to emerge from larger depth in SEM system as opposed lesser carbon contamination in the UHV system. The position of the oxygen from silicon and copper region are seen at 502 eV in the direct spectra but in the differentiated spectra, the oxygen peak is observed at 505 eV from the silicon region but at 510 eV from the copper region. The shapes of the oxygen peaks from the two regions are different which is expected from the oxides from different elements. Presence of copper was also checked in the silicon spectrum because the copper MVV peak is also expected in this energy range. No discernible features were observed in the direct or differentiated spectra at the expected higher energy range for copper.

.

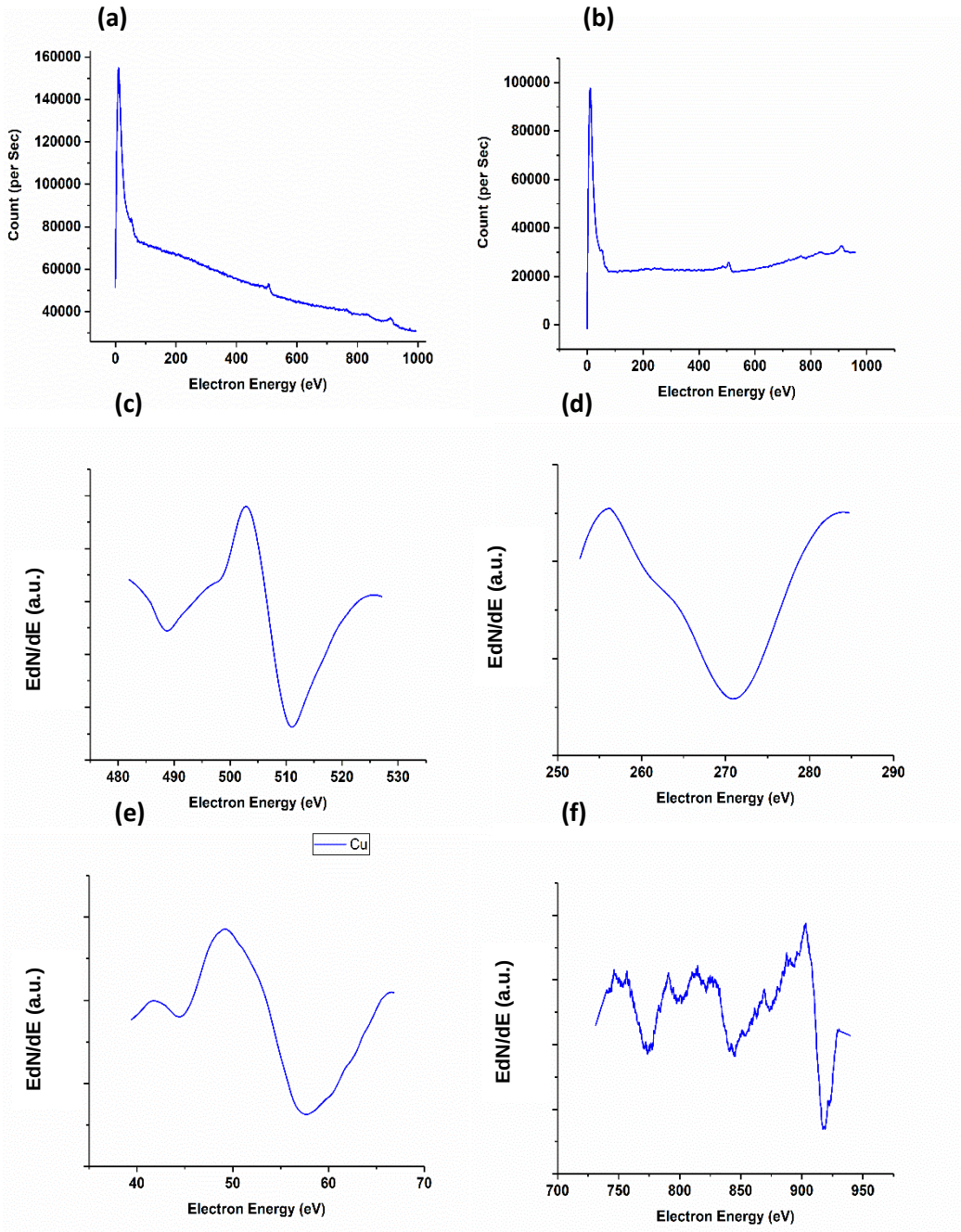

Figure 58 (a) Raw spectrum acquired from the Copper region. (b) Spectrum after background subtraction. Auger peaks in the differentiated spectrum: (c) oxygen KLL (d) carbon KLL (e) copper MVV and (f) copper LMM peaks.

.

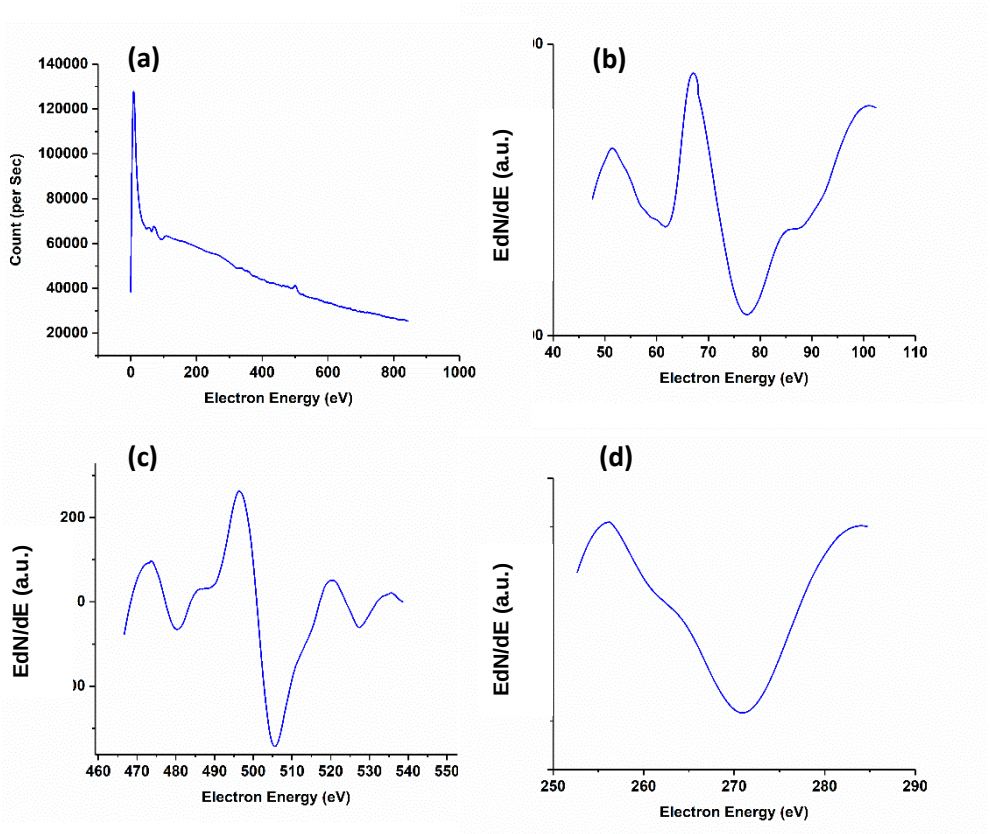

Figure 59 (a) Raw spectrum acquired from the Si region. Auger peaks in the differentiated spectrum: (b) Si LVV, (c) O KLL and (d) C KLL.

6.5. Internal Scattering

As has been pointed out, the spectra acquired in the SEM is superimposed on an unknown background. This is due to internal scattering. Internal scattering occurs when some of the high energy electrons from the sample under study, strike the inner walls of the analyser. This action generates secondary electrons. Some of these electrons may have lines of site to the output aperture and therefore may be detected. This contributes to the background signal, observed in the experimental spectrum. A significant effort goes into eliminating this effect. Internal scattering was studied extensively by Martin Seah (74), Greenwood and co-workers (75) in CHA. While El-Gomati and Bakush studied internal scattering in CMA (76).

Internal scattering is a geometric phenomenon, where in the location of the first impact on the walls of the analyser determine the line of sight to the collector for internally generated SEs. It would be easier to eliminate if it is just a first scattering problem.

.

Consider the BB shown in Figure 60a. The input apertures designed are such that the electron trajectories can only strike the walls of the output electrode. The SEs generated would be accelerated towards the input electrode inside the BB because the output electrode is biased negatively. However, SEs generated at the periphery of the input aperture (Figure 60b), both at inner and outer dimensions, can have line of site to the collector. This scenario is simulated as can be seen in the acceptance plot of Figure 60c, where angle axis is at arbitrary units and energy axis corresponds to energies higher than the BB energy. Electrons with direct line of sight to the collector and with energies greater than the BB energy can be detected and will contribute to the background signal. Figure 60d shows an ideal spectrum at the constant BB bias for such a scenario. This corresponds to a response of a high-pass filter.

Assessing internal scattering may be a good approximation for CMA which usually has open ends and a potential route to avoid higher order scattering. The BB being an enclosed box, multiple such scattering events are probable, which is pictorially represented in the Figure 60e. Intuitively, a smaller design may have a higher probability for multiple scattering events because of its smaller size. This may be able to explain the existence of background in the Zurich experiments. However, this doesn't explain the background in the spectra acquired in the SEM as opposed to one in the UHV chamber. One explanation, although not a very convincing one at this stage, is the likelihood of higher SE emission in the presence of oxides on the BB electrode surfaces. The BB was mounted on a linear drive in both the systems. Had it been a simple case of first scattering dependence, the effect should have had a major impact (minimum or maximum) in the SEM experiments, but only a marginal change was observed. Similarly, the background signal observed closer to 0 eV bias was negligible in the spectra acquired in the UHV chamber. The background intensity at 0 eV BB bias increased with increasing primary beam energies, which further confirms the presence of internal scattering. Negligible internal scattering in the UHV spectra can be regarded as a positive result but calls for a systematic study of the internal scattering in the BB analyser.

As a first step, coating the inside walls with low SEY and BSC materials such as carbon will help in minimising the effect of internal scattering. Low BSC in carbon

.

(17) ensures lower number of internal scattering events and low SEY in carbon (71) ensures lower number of SE generation at each event. Other possible solution could be the design of microstructures on the walls of the electrodes, such that the electrons are always scattered away from the output aperture, may be implemented.

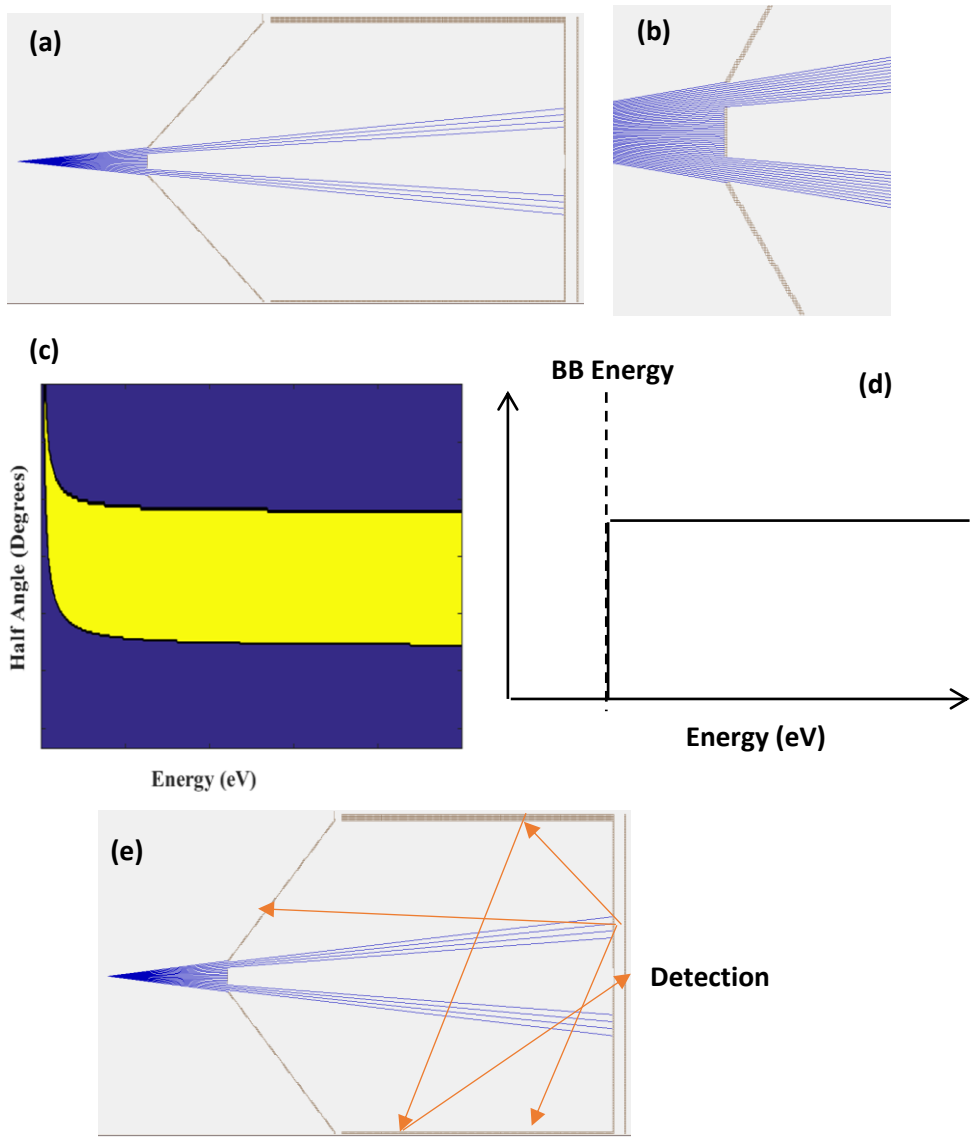

Figure 60 (a) Input aperture dimensions ensure that the high energy electrons always hit the output electrode. (b) Possible scattering centres include the periphery of the inner and outer dimensions of the input aperture. (c) Acceptance plot showing electron with energy greater than the BB energy and with line of site to the collector will be detected. (d) An ideal background due to internal scattering. (e) Multiple scattering events are highly probable in an enclosed structure like the BB.

.

6.5. Summary

A successful integration of the BB with a conventional FEG-SEM is demonstrated. Experiments have been performed for AES and SE spectroscopy. The observed Auger peaks were found in reasonable agreement with the published data. Microscopy has also been demonstrated by tuning the BB to a 12 eV pas energy. A discussion on the internal scattering is also offered.

.

Chapter 7: Conclusion

Since its discovery in the early 1930s, scanning electron microscopy has emerged as a versatile characterisation technology. Auger and SE microscopy analysis on the other hand have been the key analytical methodologies to facilitate surface analysis of materials with resolutions close to nm length scales. However, so far this energy analysis has been only pursued in UHV systems owing to surface cleanliness enabling higher contribution of the SE electrons to the net output signal.

With this motivation, obtaining energy information of the SEs in an SEM is attractive and promises to extend its existent capabilities. In addition to a HV environment, the inherent design of a typical SEM setup, poses challenges in terms of a compact analyser/ detector that can be scaled as per the system requirements. Overall, Bessel Box detector meets these prerequisites, owing to its facile design geometry. This thesis discussed the design, fabrication and implementation of a novel SE detector with energy analysis capability.

The thesis was carried out in 3 different phases. The primary phase focussed on extracting the desired geometrical parameters that meet the expected performance parameters of the detector. Simulations were designed using Simion 8.1 with self-written codes to study significant performance parameters. Numerical results were instrumental in narrowing the design considerations of the detector. The second phase involved in-house fabrication of the BB analyser with support from the mechanical workshop, Dept. of Physics, UoY.

The final phase entailed integration of the said analyser in UHV and SEM environment. A scaled in version of the device in the form of a more compact detector was also designed and integrated as part of the collaboration with ETH Zurich for the SFEM system.

The detector successfully meets the prerequisites as mentioned before with deeper understanding of effect aperture dimensions on the trade-off between resolution and collection.

.

Appendix A

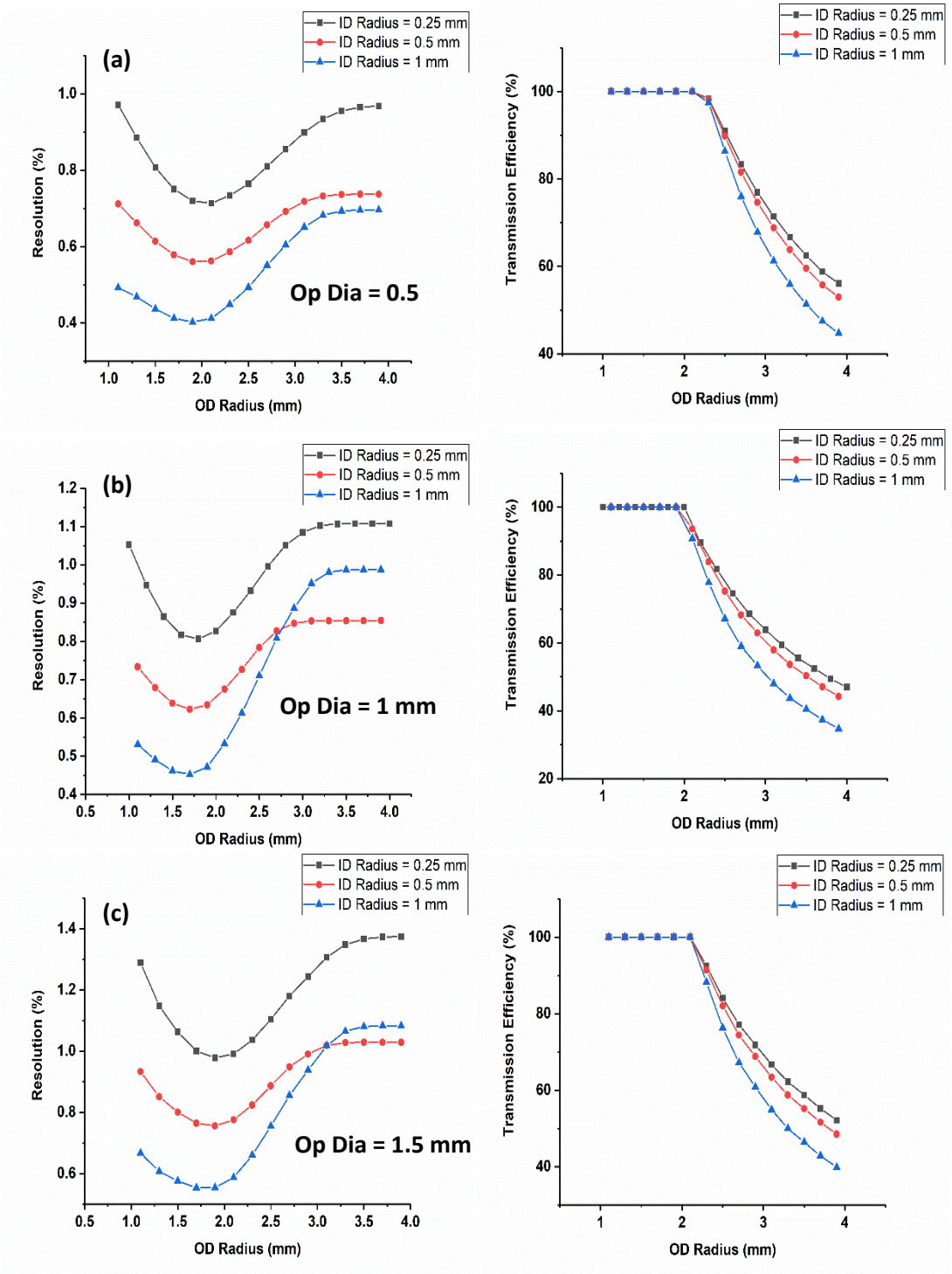

Figure 61 Resolution and transmission efficiencies as a function of input OD and ID radius for output aperture with diameters (a) 0.5 mm (b) 1 mm and (c) 1.5 mm.

.

References

1. Scanning Electron Microscopy and X-ray Microanalysis. J. I. Goldstein, D. E. Newbury, P. Echlin, D. C. Joy, C. E. Lyman, E. Lifshin, L. Sawyer, J. R. Michael. New York: Springer Third Edition, ISBN 978-1-4613-4969-3 (1992).

2. Scanning Auger Electron Microscopy. M. El-Gomati and M Prutton. New Jersey: John Wiley & Sons, ISBN:9780470866771 (2006).

3. Towards quantitative scanning electron microscopy: Applications to nano-scale analysis. M. El-Gomati, C. Walker and X. Zha. Nuclear Instruments and Methods in Physics Research A 645, 68 (2011).

4. Sub-nanometre resolution imaging of polymer–fullerene photovoltaic blends using energy-filtered scanning electron microscopy. R. Masters, A. Pearson, T. Glen, F. Sasam, L. Li, M. Dapor, A. Donald, D. Lidzey and C. Rodenburg. Nature Communications 6, 6928 (2015).

5. Wide-band detector for micro-microampere low-energy electron currents. T. Thornley and R. Everhart. Journal of Scientific Instruments 37, 7 (1960).

6. Quantitative secondary electron energy filtering in a scanning electron microscope and its applications. P. Kazemian, S. Mentink, C. Rodenburg and C. Humphreys. Ultramicroscopy107, 140 (2007).

7. J. J. Thomson and The Electron: 1897–1899 An Introduction. G. Smith. Springer:The Chemical Educator 2, 6 (1997).

8. Ueber die Reflexion der Kathodenstrahlen und eine damit verbundene neue Erscheinung secundärer Emission. L. Starke and H. Austin. Annalen der Physik 314, 10 (1902).

9. Principles of Analytical Electron Microscopy. D. C. Joy, A, D. Romig and J. I. Goldstein. Boston: Springer, ISBN: 9781489920379 (1986).

10. Monte Carlo modelling of electron-solid interactions. Z. Ding and R. Shimizu. IOP Science 34, 487 (1992).

11. Quantitative Electron Spectroscopy of Surfaces: A Standard Data Base for Electron Inelastic Mean Free Paths in solids. W. A. Dench and M. P. Seah. Surface and Interface Analysis 1, 2 (1979).

.

12. World Scientific Series in 20th Century Physics: Selected Works of Hans A. Bethe. Singapore: World Scientific, (1997).
13. Role of Plasmon Decay in Secondary Electron Emission in the Nearly-Free-Electron Metals. Application to Aluminium. T. Everhart and M. Chung. Physics Review B 15, 4699 (1977).
14. Theory of secondary electron cascade in metals. P. A. Wolff. Physics Review 95, 56 (1954).
15. From the physics of secondary electron emission to image contrast in scanning electron microscopy. J. Cazaux. Journal of Electron Microscopy 61, 5 (2012).
16. Secondary electron emission from solids. J. Cazaux. Journal of electron microscopy 61, 5 (2002).
17. Theory Experiment Comparison of the Electron Backscattering Factor from Solids at Low Electron Energy (250-5000 eV). C. Walker, M. El-Gomati, A. Assa'd and M. Zadrazil. Scanning 30, 2 (2008).
18. A new examination of secondary electron yield data. D. C. Joy and Y. Lin. Surface and Interface Analysis 37, 895 (2005).
19. Backscattering coefficients for low energy electrons. M. El-Gomati and A. Assad. Scanning 12, 185 (1998).
20. Scanning Electron Microscopy and X-ray Microanalysis. J. Goldstein. New York : Springer Third Edition, (2000).
21. New type of Auger effect and its influence on the x-ray spectrum. D. L. Kroning and D. R. Coster. Physica 2, 1 (1935).
22. Atomic radiative and radiation less yields for K and L shells. Krause, M. 307, Journal of Physical and Chemical Reference Data 8, 45 (1979).
23. Das Elektronenmikroskop. E. Ruska and M. Knoll. Zeitschrift für Physik. 78, 318 (1932).
24. The scanning electron microscope and its fields of application. C. W. Oatley and K. C. Smith. British Journal of Applied Physics 6, 391 (1955).
25. The development of the electron microscope and of electron microscopy. E. Ruska. Bioscience Reports 7, 318 (1987).

.

26. The fiftieth anniversary of the first applications of the scanning electron microscope in materials research. K. C. Smith, O. C. Wells and D McMullan. Physics Proceedings 1, 3 (2008).

27. [Online] Britannica Encyclopaedia: Scanning Electron Microscope. [Cited: June 24, 2017.] https://www.britannica.com/technology/scanning-electron-microscope.

28. The Secondary Emission Multiplier- A New Electronic Device. V. K. Zworykin, G. A. Morton and L. Malter. Proceedings of the Institute of Radio Engineers 24, 3 (1936).

29. Scanning Electron Microscopy 1928–1965. D. McMullan. Scanning 17, 318 (1995).

30. Why is it possible to detect doped regions of semiconductors in low voltage SEM: a review and update. M. El-Gomati, F. Zaggout, H. Jayacody, S. Tear and K. Wilson. Surface and Interface Analysis 37, 11 (2005).

31. Quantitative secondary electron imaging for work function extraction at atomic level and layer identification of graphene. Y. Zhou, D. Fox, P. Maguire, R. O ' Connell, R. Masters, C. Rodenburg, H. Wu, M. Dapor, Y. Chen and H. Zhang. Scientific Reports 6, 21045 (2016).

32. High contrast imaging and thickness determination of graphene with in-column secondary electron microscopy. V. Kochat, A. N. Pal, E. Sneha, A. S. Kumar, A. Gairola, S. A. Shivashankar, S. Raghavan, A. Gosh. Journal of Applied Physics 110, 1 (2011).

33. Basic Vacuum Technology. A. Chambers, R. Fitch and B. Halliday. Bristol: IOP Publishing ltd, ISBN 9780750304955 (1989).

34. Characteristic energy losses of electrons scattered from incandescent solids. Rydberg, Eric. Proceedings of the Royal Society A 127, 804 (1930).

35. Inelastic Scattering of Electrons from Solids. Rydberg, E. Physical Review 50, 138 (1936).

36. Analysis of Materials by Electron-Excited Auger Electrons. L. A. Harris. Journal of Applied Physics 39, 3 (1968).

37. Use of LEED Apparatus for the Detection and Identification of Surface Contaminants. W. T. Peria and R. E. Weber. Journal of Applied Physics 38, 11 (1967).

.

38. High Sensitivity Auger Electron Spectrometer. P. W. Palmberg, G. K. Bohn, and J. C. Tracy. Applied Physics Letters 15, 254 (1969).

39. Towards quantitative scanning electron microscopy: Applications to nano-scale analysis. M. El-Gomati, C. Walker and X. Zha. Nuclear Instruments and Methods in Physics Research A 645, 68 (2011).

40. A high energy resolution Auger electron spectrometer using concentric hemispheres. P. J. Bassett, T. E. Gallon and M. Prutton. Journal of Physics E: Scientific Instruments 5, 2 (1972).

41. A Third-generation Auger Microscope using Parallel Multispectral Data Acquisition and Analysis. M. Prutton, C. Walker, J. Greenwood, P. G. Kenny, J. C. Dee, I. R. Barkshire, R. H. Roberts and M. El Gomati. Surface and Interface Analysis 17, 71 (1991).

42. Electron Beam Testing Technology: Electron Spectrometers and Voltage Measurements. J. T. Thong. Boston: Springer, 211 (1993).

43. The Examination of p-n Junctions with the Scanning Electron Microscope. T. E. Everhart and C. W. Oatley, International Journal of Electronics 2, 42 (1957).

44. Voltage measurement in the scanning electron microscope. O. C. Wells and C. G. Bremer. Journal of Physics E: Scientific Instruments 1, 12 (1968).

45. Electric Field Mapping in Conducting Langmuir-Blodgett Films. A. Barraud, J. Richard, A. R. Teixier and M. Vandevyver. Thin Solid Films 159, 1 (1988).

46. Cylindrical Capacitor as an Analyzer I. Nonrelativistic Part. H. Z Sar-el. Review of Scientific Instruments 38, 1210 (1967)

47. New improvements in energy and spatial (x, y, z) resolution in AES and XPS applications. C. Tewell and F. Reniers. Journal of Electron Spectroscopy and Related Phenomena 142, 1 (2005).

48. A fast, parallel acquisition, electron energy analyzer: The hyperbolic field analyzer. M. Jacka, M. Kirk, M. El-Gomati, and M. Prutton. Review of Scientific Instruments 70, 2282 (1999).

49. Hyperbolic field electron energy analyzer with second order focussing. M. Jacka, A. Kale, and N. Traitler. Review of Scientific Instruments 74, 4298 (2003).

.

50. A new electron spectrometer design:II. J.D. Allen, J. D. Durham, G. K. Schweitzer, and W.E. Deeds. Journal of Electron Spectroscopy and Related Phenomena 8, 395 (1976)

51. Methods and apparatus for energy analysis and energy filtering of secondary ions and electrons. W. L. Fite US Patent 4146787, March 27, (1979).

52. Micromachined array of electrostatic energy analysers for charged particles. R. E. Stalder, S. Boumsellek, T. R. Van Zandt, T. W. Kenny, M. H. Hecht and F. E. Grunthaner. Journal of Vacuum Science & Technology A 12, 2554 (1994).

53. Construction and performance characteristics of a low-cost energy prefilter. J. L. Hock and J. H. Craig Jr. Journal of Vacuum Science & Technology 17, 1360 (1980).

54. Transmission characteristics of a cylindrical energy analyzer. W. G. Durrer and J. H. Craig. Journal of Vacuum Science & Technology A 7, 337 (1989).

55. A new Bessel-Box energy analyser for sputtered neutral mass Spectrometry. R. Shimizu and H. Yoshikawa. Japenese Journal of Applied Physics 29, 2 (1990).

56. [Online] Hiden Analytical [Cited: November 1, 2019.] https://www.hidenanalytical.com/products/.

57. The retarding Bessel–Box—An electron-spectrometer designed for pump/probe experiments. G. Schiwietz, M. Beyea, D. Kühna and G. Xiao. Journal of Electron Spectroscopy and Related Phenomena 203, 51 (2015).

58. Development of a new ionization gauge with Bessel Box type energy analyser. H. Akimichi, T. Tanaka, K. Takeuchi and Y. Tuzi. Vacuum 46, 8 (1995).

59. [Online] AxTRAN [Cited: November 1, 2019.] https://www.ulvac.com/components/Gauges/Extremely-High-Vacuum-Gauges/AxTRAN.

60. SIMION for the personal computer in reflection. D. Dahl. International Journal of Mass Spectrometry 200, 337 (2000).

61. Static and Dynamic Electricity. W. R. Smythe. New York: McGraw-Hill Book Company Inc., ISBN: B001B0PXTQ (1950).

62. Microfabrication of fine-pitch high aspect ratio Faraday cup arrays in silicon. C. A. Bower, K. H. Gilchrist, M. R. Lueck and B. R. Stoner. Sensors and Actuators A: Physical 137, 2 (2007).

.

63. Chapter Two - A Review of Scanning Electron Microscopy in Near Field Emission Mode. T. L. Kirk. Advances in Imaging and Electron Physics 204, (2017).

64. An Improved Electron Multiplier Particle Counter. J. Allen. Review of Scientific Instruments 18, 10 (2004).

65. Microchannel plate detectors. W. J. Ladsilas. Nuclear Instruments and Methods 162, 1 (1979).

66. Modern Techniques of Surface Science. T. David and W Phillip and Delchar. Cambridge: Cambridge University Press, ISBN: 0521357195 (1988).

67. [Online] Origin Labs [Cited: 11 01, 2019.] https://www.originlab.com/.

68. Dielectric Loss Function of Si and SiO2 from Quantitative Analysis of REELS Spectra. F. Yubero, S. Tougaard, E. Elizalde and J. M. Sanz. Surface and Interface Analysis 20, 719 (1993).

69. Energy spectra of electron yields from silicon: Theory and experiment. Z. Chaoui, Z.J. Ding and K. Goto. Physics Letters A 373, 1679 (2009).

70. Handbook of Auger Electron Spectroscopy. L. E. Davis, N. C. MacDonald, P. W. Palmberg, G. E. Riach and R. E. Weber. Eden Praire : Physics Electronics Division (1976).

71. The Secondary Electron Emission Yield for 24 Solid Elements Excited by Primary Energy in the range 250–5,000 eV: Theory and Experiment Comparison. C. Walker, M. El-Gomati, A. Assa'd and M. Zadrazil. Scanning 30, 365 (2008).

72. Simulation of a Bessel box electron energy analyser for analysis of secondary electrons. A. Suri, A. Pratt, S. Tear, C. Walker and M. El-Gomati. Journal of Physics: Conference Series 902, 6596 (2017).

73. Practical Surface Analysis. M. P. Seah and D. Briggs. Chichester: Wiley, ISBN 0-471-92081-9 (1992).

74. Scattering in Electron Spectrometers, Diagnosis and Avoidance. I. Concentric Hemispherical Analysers. M. P. Seah. Surface and Interface Analysis 20, 865 (1993).

75. Internal Scattering of Electrons in a Hemispherical Spectrometer. J. C. Greenwood, M. Prutton, R. H. Roberts and Z. Liu. Surface and Interface Analysis 20, 891 (1993).

76. Internal scattering in a single pass cylindrical mirror analyser. T.A. Bakush, M.M. El Gomati. Journal of Electron Spectroscopy and Related Phenomena 74, 104 (1995).

.